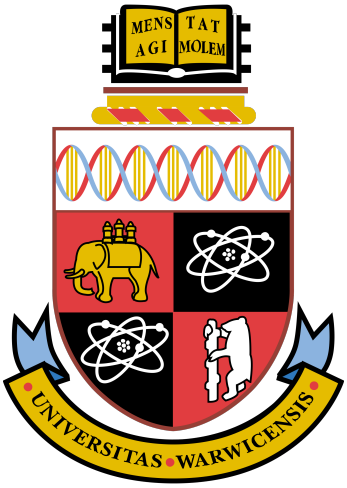

Topological Insulators: A Study of Bulk Crystalline and Nanomaterials

by

Mohammed Saghir

Thesis

Submitted to the University of Warwick in partial fulfillment of the requirements for admission to the degree of

Doctor of Philosophy

Department of Physics

July 2016

THE UNIVERSITY OF WARWICK

Contents

Acknowledgements

Words that amplify the appreciation and recognition that Prof Geetha Balakrishnan deserves are difficult to find and so I will begin by saying that I am humbly thankful for the all the good advice and assistance you have provided over the last few years both academically and personally. I also wish to thank Dr. Neil Wilson for his assistance and meaningful discussions. I could not have wished for better supervisors. I also thank the numerous collaborators who have one way or another contributed to the work presented: Dr M. Lees, Dr A. Hillier, Dr A. Sanchez, Dr M. Walker, Prof C. McConville, Mr S. York, Mr S. Hindmarsh and Mr T. Orton.

Then comes the infamous 'bants' which have been a prominent feature during this PhD. I think we have collectively covered all parts of life both real and fictitious so at least we are well prepared for such occasions. Again, ink on paper will not convey the thanks I offer to those involved, but to all the academics, those in the physics posse, the collective that is the S&M group and Mr and Mrs Jones for getting me to 'work' safely, for all the humour and laughter along this journey, I thank you all.

To my wonderful Mum, thank you for your love and support and Dad I hope you can now relax and enjoy what life brings to you - for you have both been such successful parents. Special thanks for the support from my brothers and sisters and to my beautiful nephews and nieces.

By the will of God to whom I give thanks.

رَبِّ زِدْنِي عِلْمًا

Declaration

All data presented in this thesis was obtained by myself with the exception of some data, the details of which are presented here. XPS data in Chapter 3 was obtained with the assistance of Dr M Walker. TEM data presented in Chapter 4 was obtained with the assistance of Dr A. Sanchez and AFM data in Chapter 5 with the assistance of Dr N Wilson. Graphene substrates used in Chapter 5 were provided by Dr A Marsden. In all cases, I was either the sole experimentalist or a leading member of the experimental team. No part of this work has been submitted for examination for the award of Doctor of Philosophy at any other institution.

Publications and Conference Presentations

The work in this thesis has led to a number of publications and conference presentations shown below.

Publications

- *Nanomaterials and Crystals of Topological Insulators and Topological Crystalline Insulators*. **M. Saghir**, M.R. Lees, S.J. York, S.A. Hindmarsh, A.M. Sanchez, M. Walker. C.F. McConville and G. Balakrishnan - *JIISc. Rev. 96, 2, (2016)*

- *Surface preparation of microcrystals of the topological crystalline insulator, SnTe*. **M. Saghir**, M. Walker, C. F. McConville and G. Balakrishnan - Appl. Phys. Lett. 108, 061602 (2016)

- *Observation of surface states on heavily indium doped SnTe(111), a superconducting topological crystalline insulator*. C. M. Polley, V. Jovic, T-Y. Su, **M. Saghir**, D. Newby Jr., B. Kowalski, R. Jakiela, A. Barcz, M. Guziewicz, T. Balasubramanian, G. Balakrishnan, J. Laverock and K. E. Smith - Phys. Rev. B 93, 075132 (2016)

- *Nanomaterials of the topological crystalline insulators, $Pb_{1-x}Sn_xTe$ and $Pb_{1-x}Sn_xSe$*. **M. Saghir**, A. M. Sanchez, S. A. Hindmarsh, S.

J. York and G. Balakrishnan - *Cryst. Growth Des. (2015)*

- *Studies of the superconducting properties of $Sn_{1-x}In_xTe$ ($x = 0.38$ to 0.45) using muon-spin spectroscopy*. **M. Saghir**, J. A. T. Barker, G. Balakrishnan, A. D. Hillier and M. R. Lees - Phys. Rev. B (2014)

- *Synthesis and Characterization of Nanomaterials of the Topological Crystalline Insulator SnTe*. **M. Saghir**, M. R. Lees. S. J. York and G. Balakrishnan - Cryst. Growth Des. (2014)

Conference Presentations

- APS March Meeting 2014, Denver, Colorado, USA - *Talk*

- Frontiers in Unconventional Superconductivity and Magnetism 2014, Bristol, UK - *Poster*

Abbreviations

AFM	.....	Atomic force microscopy
ARPES	.....	Angle resolved photoemmision spectroscopy
CCD	.....	Charge coupled device
CVD	.....	Chemical vapour deposition
EBSD	.....	Electron backscatter diffraction
EDX	.....	Energy-dispersive X-ray spectroscopy
FCC	.....	Face centred cubic
QDMPMS	.....	Quantum design Magnetic property measurement system
RV	.....	Rough vacuum ($\sim 1 \times 10^{-6}$ mbar)
SAED	.....	Selected area electron diffraction
SAVR	.....	Surface-area-to-volume-ratio
sccm	.....	Standard cubic centimeters per minute
SEM	.....	Scanning electron microscopy
SQUID	.....	Superconducting quantum interference device
TCI	.....	Topological crystalline insulator
TEM	.....	Transmission electron microscopy

TI ..... Topological insulator

ToA ..... Take-off angle

TRIM ..... Time reversal invariant momenta

UHV ..... Ultra-high vacuum ($\sim 1 \times 10^{-9}$ mbar)

VLS ..... Vapour-liquid-solid

TS ..... Vapour-solid

XPS ..... X-ray photoelectron spectroscopy

XRD ..... X-ray diffraction

ZFCW ..... Zero-field cooled-warmed

Abstract

A new class of materials, TIs and TCIs, have been shown to exhibit exotic surface state properties that are protected by mirror or time-reversal symmetry. It is expected that the surface states will be easier to detect if the SAVR of the material increases. We report the experimental procedures to obtain high quality crystal boules of the TCI, $Sn_{1-x}In_xTe$, for $0 \leq x \leq 0.45$, from which nanowires and microcrystals can be produced by the VLS growth technique. Detailed characterisation measurements of the bulk crystals, the superconducting properties as well as characterisation of the nanowires and microcrystals produced are presented. We also present optimised growth procedures to obtain high quality bulk crystals of the TCIs $Pb_{1-x}Sn_xTe$ and $Pb_{1-x}Sn_xSe$, and nanowires from the bulk crystals, also using a VLS growth mechanism. Nanowires of $Pb_{1-x}Sn_xTe$ have been produced with a Sn composition of $x = 0.25$, at which a transition from trivial to non-trivial insulator is reported. The results obtained on the growth of nanomaterials of $Pb_{1-x}Sn_xSe$ are also described. Detailed characterisation of the bulk crystals and the nanomaterials through x-ray diffraction, microscopy techniques and EDX analysis are presented. Sb_2Te_3 is also a topological insulator which, under certain conditions, becomes superconducting. The growth methods and characterisation of Sb_2Te_3 crystal boules are discussed. The methods used to convert bulk samples of Sb_2Te_3 into nanomaterials and 2D layers on graphene are also presented. Investigating nanometer and micron sized materials thought to exhibit topological surface properties can present a challenge, as clean surfaces are a pre-requisite for band structure measurements when using nano-ARPES or laser-ARPES in UHV. We present the findings of an XPS study where various cleaning methods have been employed to reduce the surface contamination and preserve the surface quality for surface sensitive measurements. Microcrystals of SnTe were treated with atomic hydrogen, argon sputtering, annealing, as well as a combination of treatments. The samples were characterised using SEM, both before and after treatment. It was found that atomic hydrogen cleaning with an anneal cycle (200 °C) gave the best clean surface results.

List of Figures

List of Tables

Chapter 1

Introduction

1.1 Motivation

The discovery of topological insulators took place in 2005. Following this discovery, a large number of materials have come to the attention of researchers worldwide because of the exotic surface states the materials exhibit. The surface properties of these topological insulators have raised interesting questions about fundamental physics and the potential applications in which they could be used. The number of articles published year on year in this field of study has grown and does not show any signs of slowing (Figure 1.1). Research in topological insulators is fast paced and as is the case for many areas of physics, theoretical predictions lead those of experimental observation.

There are many challenges and questions that are still outstanding in this field of research. One such hurdle is to experimentally observe the theoretical predictions of the exotic surface states topological materials possess. This thesis brings together two areas of research which have received notable attention recently. The first involves the study of newly discovered topological insulators. The drive to produce high quality single crystals of these materials for study using a variety of scientific methods

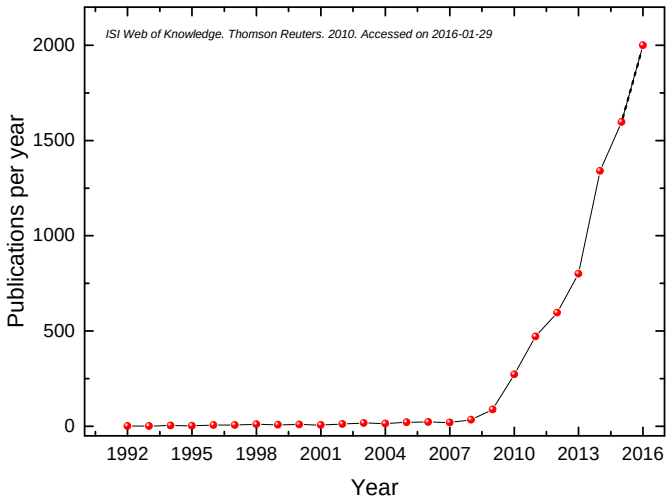

Figure 1.1: Number of articles published in topological insulators per year.

is ever present with an aim to detect the exotic surface states. Secondly, it has been predicted that producing materials with a high surface-area-to-volume-ratio (SAVR), could lead to the easier detection of these topological surface states.

To address the two issues above, this dissertation will first focus on describing the methods used to obtain high quality single crystals of the materials that have been chosen to be studied, followed by the characterisation of them. Established growth procedures will be followed for such materials. For the growth of nanomaterials, well established growth processes such as the vapour-liquid-solid mechanism, which have commonly been used to grow nanowires and nanomaterials from the start of the century, will be used, however, the application of these methods for the growth of TI's and TCI's is relatively new. Although there will be a focus on the production of topological insulators as nanowires, we will explore other morphologies that can be formed and the growth environments that govern those. As a result, this thesis will explore the growth

and characterisation of such materials i.e. those with higher SAVR.

The discovery of the Hall effect by Edwin Hall in the 1800's and subsequently the quantum Hall effect since the 1980's has paved the way for research in new areas of fundamental physics. The quantisation of the electron system led to an understanding of how a large system of interacting electrons can form a surprisingly complex quantum ground state. This then led to the realisation of further quantum states such as the fractional quantum Hall effect. These quantum states were typically observed when materials are placed in high magnetic fields and the resulting system is much like that of a semiconductor. There is a Fermi level that at first in the classical Hall state showed no gap, but then in a high magnetic field, a bulk energy gap can develop between the conduction and valance band.

A material such as this is the first example of a topological insulating material, where the bulk of the material is insulating, but where conduction channels remain in edge states in the quantum Hall regime. This is a very interesting concept. Previously, the edge conductance of a material was attributed to dangling bonds on the surface of the material or an electronic reconfiguration. It has since been realised that there are protected channels through which conduction could occur, irrespective of defects and impurities to the system.

In the early 2000's, protecting the edge states without applying a magnetic field was being investigated. This led to the discovery of a 2D topological insulator. Work by Kane & Mele in 2005, Bernevig & Zhang in 2006 and Sheng & Haldane also in 2006 demonstrated the theoretical existence of TI's and they were later experimentally observed by Molenkamp *et al.* in HgTe quantum wells. [11–15]

The additional protection of the edge states was theoretically possible due to the Hall conductance equating to zero when the Chern number or the topological quantum number, n, became zero, leading to a topologically protected edge state. This relationship can be seen in Equation 1.1, where σ is the Hall conductance, n is the Chern number, e the elementary

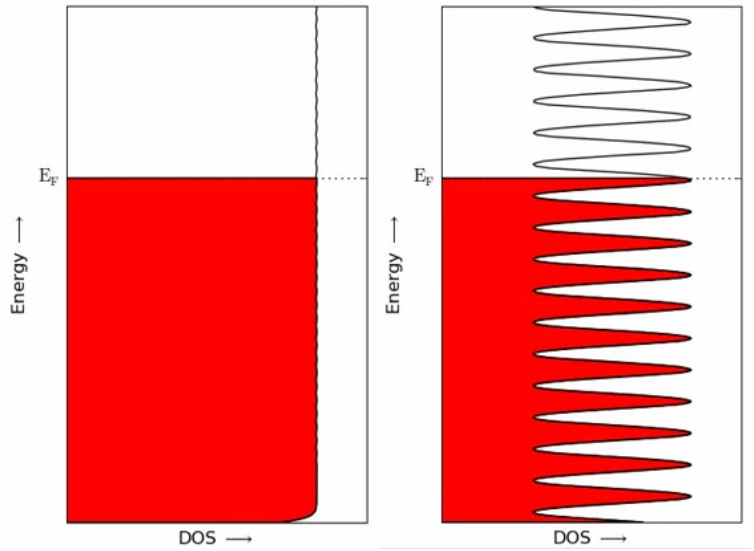

Figure 1.2: (Left) The classical density of states (DOS) for a Hall conductor. (Right) The Landau levels or quantization of the Hall effect. E_F is the Fermi surface.

charge and h is Plank's constant.

$$\sigma = ne^2/h = 0 \tag{1.1}$$

The search for additional topological quantum numbers and therefore additional topologically protected states led to the discovery of 3D topological insulators and various sub-groups. Such sub-groups include topological crystalline insulators and topological superconductors. The standard procedure involved for the measurement of these protected surface states is to first go to the boundary of the materials and observe the state of the electrons. This is then compared that to the state of the electron system in the bulk of the material. This can be summarised as a spin-sensitive momentum resolved edge vs. bulk measurement. A typical signature for a topological insulator is the observation of gapless excitations with a linear dispersion in the electronic band structure also known as a Dirac cone. These occur at crossings in the Fermi surface be-

tween the conduction and valance bands. For almost all materials where metallic surface states exist, if the density of states (DOS) between two time reversal invariant momenta (TRIMs) are observed and if the number of crossings of the Fermi surface is even, then the material is said to be trivial. This is irrespective of the origin of the surface states, be it due to dangling bonds or a surface electronic reconfiguration. In very rare cases, there are an odd number of crossings of the Fermi surface in the DOS and these would give rise to a material that is non-trivial described below. How these surface states differ from conventional states in terms of electron spins is that in a normal material, the electrons enjoy full degrees of freedom. In a 3D material, a 2D slice would show electrons moving in both directions with both spins, both up and down. In a non-trivial material, spin momentum locking occurs where, for example, if we imagine a slab of material, an electron moving to the right can have a down associated spin and a left moving electron an up spin. The result of such a system in terms of physical properties is a dissipationless flow of electrons in thin films as back-scattering is not allowed and the edge states exist independent of defects in the material. The beauty of the protection of the edge states in a topological insulator is that this would be observable at room temperature and without the need of a magnetic field. This is not the case for the quantum Hall effect which requires a magnetic field and low temperatures.

The newer sub-class of materials known as topological crystalline insulators (TCIs) differ from conventional topological insulators (TIs) because of the topological protection offered to them. The earlier TI materials preserved time-reversal symmetry, however, the topological protection offered to the newer phases of matter that are TCIs, are by crystal symmetries such as rotation and reflection. These TCIs also possess a gapless surface state at the boundary however only those surfaces that obey the symmetry rules are gapless.

The timeline shown in Figure 1.3 gives an overview of the progression

in the field. It also highlights the key theoretical predictions and when they were observed experimentally. There is also a brief insight into the compounds chosen for the work presented in this thesis.

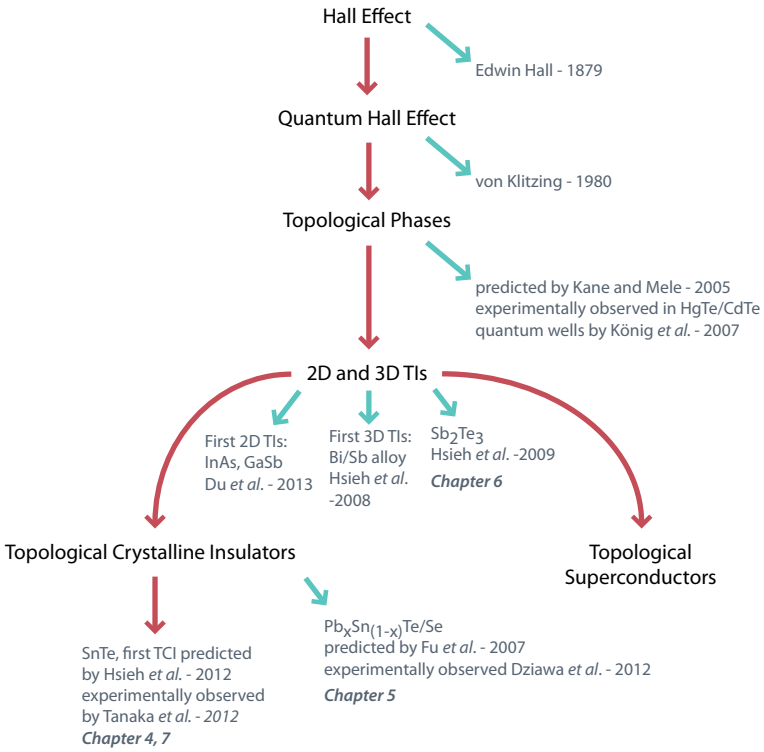

Figure 1.3: Basic overview of the progression in the field of topological materials.

The potential applications that topological insulators and topological crystalline insulators can be used in are exciting. From spintronics to quantum computing devices, the properties of these materials demonstrate promising advances in technology. [16]

TI and TCI materials that are thin enough have even been shown to possess surface conductivity and bulk insulation properties at room temperature. One method employed to improve the detection of the surface states over the interference of the bulk signal is to increase the surface-area-to-volume-ratio (SAVR) of the materials. This is achieved

by producing nanomaterials and micromaterials of the TIs and TCIs. The production of these high SAVR materials is the main focus of this thesis along with the characterisation of them. The majority of the samples studied are TCIs with the exception of Sb_2Te_3. TCI materials are not conventional TIs due to the even number of crossings between the time-reversal invariant momenta (TRIM) points. However, as the band gaps are located at symmetry-related TRIMs, they can be classed as TCIs. Figure 1.4 shows the locations of the Dirac cones in the Brillouin zones of the rock-salt structure of some of the TCIs being investigated.

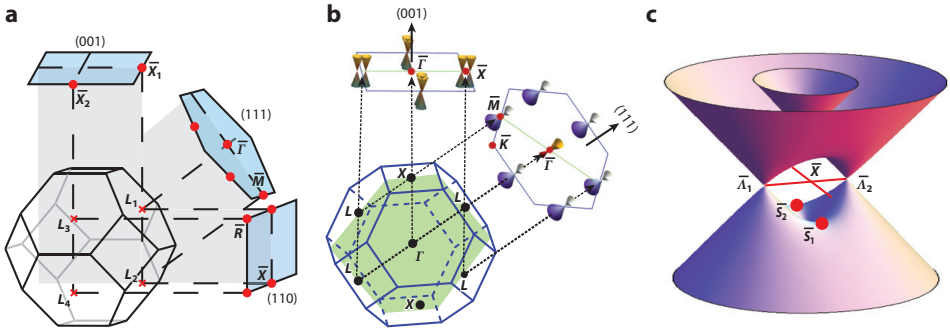

Figure 1.4: (a) The 3D Brillouin zone. Red dots show the high symmetry locations of the rock-salt structure. (b) Dirac cone locations for the (001) and (111) surfaces. (c) Tight-binding model of the double Dirac cone structure for the (001) surface state. *Figure adapted from [1].*

1.2 Topological Materials

The following section will provide a detailed discussion of the materials being investigated in this thesis. A discussion on the topological properties of the materials along with the progress in the research of the compounds will be covered. To date these materials have been investigated on cleaved surfaces of bulk crystals. This presents some challenges as many of the techniques used to verify the topological nature of the materials are surface sensitive probes. Characterisation tools such as ARPES, transport

measurements and surface scanning techniques are all surface sensitive. Although the states are protected even if defects and contamination exist on the surface, measurement of them is still a problem. Furthermore, obtaining bulk materials that have a truly insulating bulk is hard to realise, although some experimental evidence shows insulating bulk behaviour in some Bi-based materials [16].

The TCI materials of interest will be discussed first followed by TI compounds. TCI materials have the added interest in that there is a large variety of methods upon which the band gap can be engineered and potentially useful properties extracted. Methods used to do this include the introduction of magnetic dopants, mechanical strain within a lattice, thickness engineering and disorder. [17]

1.2.1 SnTe & $Sn_{1-x}In_xTe$

Before the discovery of TI's and TCI materials, research in IV-VI semimetal SnTe focused on the semiconducting properties of the material. The material is normally *p*-type due to Sn vacancies in the lattice and has uses in infrared detectors and thermoelectric generators. [18, 19] SnTe has a simple rock-salt structure at room temperature and atmospheric pressure (Figure 1.5). SnTe is a narrow-gap semiconductor with a rock salt cubic structure (lattice constant, $a = 0.633$ nm). SnTe was the first TCI material which was predicted to exist by Hsieh *et al.* [20] and later observed experimentally by Tanaka *et al.* [21, 22]. The band gaps in SnTe are located at four equivalent points in the face centred cubic Brillouin zone (Figure 1.4). The TCI properties of SnTe were first experimentally observed by way of ARPES measurements, where the TCI surface characteristics were detected (double Dirac cones with helical edge states). The band degeneracy observed in TCIs are protected by rotational and mirror symmetry, in place of the role played by time-reversal symmetry in TIs. [23–25] There is added interest in SnTe due to the superconducting

properties of the material, which were observed upon the substitution of In atoms at Sn sites.

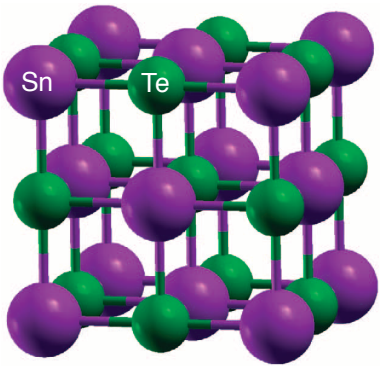

Figure 1.5: Rock salt structure of SnTe. SnTe has a lattice constant, a = 0.633 nm. *Figure adapted from [2].*

The percentage of Sn vacancies formed naturally in the compound SnTe is around 1 %, where the Sn vacancies are in the form of holes. Pure SnTe is superconducting, however, only at low temperatures ($T_{\mathrm{c}} \approx$ 0.1 K). [26] The material becomes a superconductor when the number of vacancies reaches 10^{20} cm^{-3}.

The superconducting critical temperature T_c is below 0.3 K for hole carrier densities p up to 2×10^{21} cm^{-3}, however, with the substitution of In atoms at Sn sites, the superconducting transition can change. [27]

The effect of increasing the In composition is to increase the number of holes in the system, where one further hole is introduced for every Sn atom substituted. When the In substitution lies at around 6% in $Sn_{0.988-x}In_xTe$, the T_c of the materials increases to around 2 K. For increased levels of In substitution, ($x \sim 0.4$ to 0.45), a superconducting transition as high as ~ 4.5 K can be achieved. [28,29] For x less than $x \approx$ 2 %, the structure of $Sn_{1-x}In_xTe$ changes and becomes rhombohedral. Above this level of In doping, the structure of the material is cubic to zero kelvin. [27]

With regards to the TCI properties of $Sn_{1-x}In_xTe$, which are independent to the superconducting properties of the material, ARPES measure-

ments have shown that for low levels of In substitution in $Sn_{1-x}In_xTe$, e.g. $x = 0.045$, a topological surface state can be detected. [30]

Studying the bulk properties of $Sn_{1-x}In_xTe$, is important to better understand the physics behind this new class of materials. It is for this reason that magnetization experiments have been performed to investigate the superconducting properties of $Sn_{1-x}In_xTe$ for $0.38 \leq x \leq 0.45$. Our investigations show that this level of In substitution gives the optimum T_c for this system.

It has been reported that TI materials in nanoform allow the observation of enhanced TI features due to an increased surface-area-to-volume ratio. [31] As materials are transformed into their nano counterparts, the surface states have a greater contribution to the sample properties and conversely, bulk properties are suppressed. [32] To date, many successful growths of nanomaterials have been performed for both binary and ternary compounds of the Bi_2Se_3/Te_3 family. High quality nanomaterials can be obtained with various stoichiometries using both wet and dry synthesis methods. [32–35] Some examples of synthesis methods include van der Waals epitaxy of Bi_2Te_2Se on hexagonal boron nitride sheets or electro deposition of Bi_2Te_2Se/Te to form multi-arrays of nanowires. [35, 36] Another common method for nanowire growth is similar to that for the fabrication of ZnO nanowires using vapour-liquid-solid (VLS) technique. [37] The VLS growth technique is known to be an effective growth method for high quality crystalline nanomaterials with high yields. [38–42] The VLS method has also been used to demonstrate the growth of Bi_2Se_3 and Bi_2Te_3 nanomaterials. [31, 33, 43] SnTe has been previously reported to have been produced in nanoform using methods such as chemical reduction, hydrothermal synthesis as well as chemical synthesis. [44–46] We have also become aware of the recent publications by Li *et al* and Safdar *et al* for the growth of nanostructures of SnTe using the VLS method. [47, 48]

As SnTe was the first TCI material to be predicted and to reveal

the unique band structure it possesses, and due to the superconducting properties of In doped SnTe, it was chosen as a candidate to be converted into nanomaterials using new growth techniques and methods. As a result, we show a detailed study for the growth of bulk crystals of $Sn_{1-x}In_xTe$ $(0 \leq x \leq 0.45)$ and the conversion of these materials into nanomaterials.

1.2.2 $Pb_{1-x}Sn_xTe/Se$

Both $Pb_{1-x}Sn_xTe$ and $Pb_{1-x}Sn_xSe$ are relatively new 2nd generation TCI materials and as such, new TCI properties of these materials are emerging. Below is an account of the current state of research for this material with regards to the TCI behaviour. The parent compound of $Pb_{1-x}Sn_xTe$ is PbTe and for $Pb_{1-x}Sn_xSe$ it is PbSe. Prior to the discovery of topological insulators, PbTe has in the past been investigated for its strong thermoelectric properties and subsequently there are many applications arising from the use of this material. [49] Similarly, PbSe is known to be a very important semiconductor and this compound has been used to make devices such as gas sensors and infrared detectors. [50]

The effect of substituting Sn atoms into Pb sites in PbTe and PbSe introduces strain into the lattice of these materials. Depending on the level of the substituion, a band inversion can be induced at the Fermi level, thereby changing the trivial insulating nature of the materials to topologically non-trivial. [51] Due to the new states of matter that have been observed in these materials as a function of Sn substitution, there is a motivation to produce high quality bulk samples of $Pb_{1-x}Sn_xTe$ and $Pb_{1-x}Sn_xSe$, from which nanomaterials can be produced.

In the solid solutions, $Pb_{1-x}Sn_xTe$ and $Pb_{1-x}Sn_xSe$, TCI surface states have been experimentally observed. [3, 52, 53] The TCI nature of these materials is unaffected by the mixing disorder of the system. [54] Further experimental evidence obtained using spin-resolved photoelectron spectroscopy (SRPES) has led to the direct observation of spin textures for the

(001) metallic surfaces in both $Pb_{0.73}Sn_{0.27}Se$ and $Pb_{0.60}Sn_{0.40}Te$. [52, 55]

Unlike in the case of SnTe, where the experimental observation of the TCI states can be difficult due to the p-type nature of the material, the tunable nature of the chemical potential to n and p-type in $Pb_{1-x}Sn_xTe/Se$ makes these compounds more suitable for experimentally observing the TCI states, thus providing the motivation for the study of these materials. [3]

The resulting solid solution upon substitution, $Pb_{1-x}Sn_xTe$, is a narrow band semiconductor with a tunable electronic structure based on the Sn/Pb ratio. [52] The structure of $Pb_{1-x}Sn_xTe$ is cubic for all Sn substitutions. For Sn substitution of up to $x \leq 0.4$ in $Pb_{1-x}Sn_xSe$, the structure remains cubic, similar to that of PbSe, whilst the other end member SnSe adopts an orthorhombic structure. The Brillouin zone forms a truncated octohedron of 6 square faces and 4 hexagonal faces.

For both $Pb_{1-x}Sn_xTe$ and $Pb_{1-x}Sn_xSe$, the location of the band inversions are analogous to the material SnTe as can be seen in Figure 1.6.

The introduction of Sn atoms allows for the closing of the band gap producing a Dirac state. It cannot be classed as a conventional TI according to the Kane and Mele system as there are an even number of band inversions. However, as the momentum space locations coincide with the momentum space mirror planes it can be considered a TCI. For $Pb_{1-x}Sn_xTe$, the onset for the critical transition from a trivial to non-trivial insulator, occurs at a Sn substitution of $\sim x = 0.25$ and the optimum point of this transition is $x = 0.4$. [52,53]. A TCI phase onset is observed in $Pb_{1-x}Sn_xSe$ for x values between $0.18 \leq x \leq 0.3$. This transition is further dependent on a critical temperature, up to $T_c = 250$ K [3] and the TCI transition is not observed above this critical temperature.

$Pb_{1-x}Sn_xTe$ forms a rock-salt structure similar to that of SnTe. Substituting Sn atoms at Pb sites can be done without the introduction of much strain into the system due to the similar atomic radii (Pb = 0.154

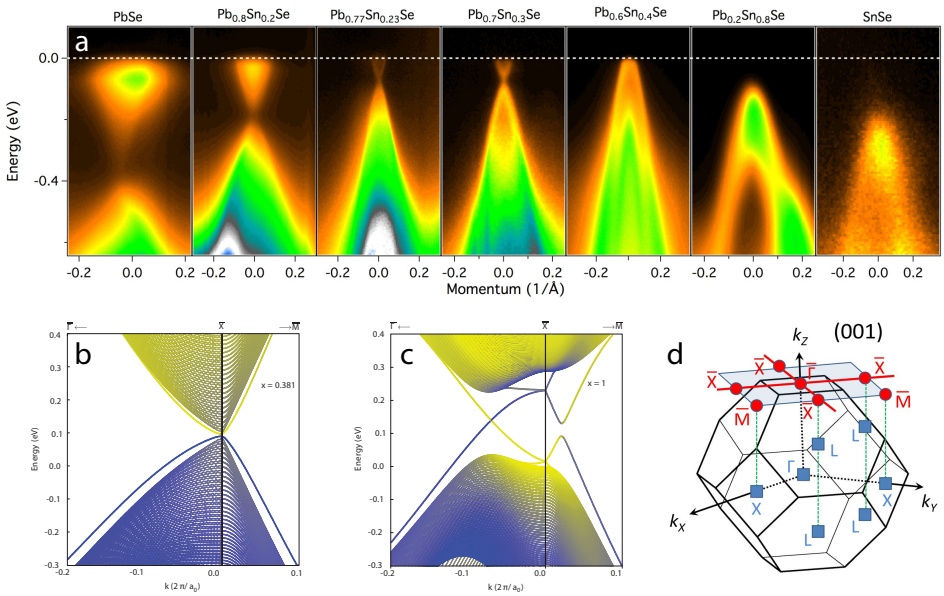

Figure 1.6: (a) ARPES measurements showing the development of the topological phase transition from PbSe to $Pb_{1-x}Sn_xTe$ and SnSe. (b) Band structure calculations of $Pb_{1-x}Sn_xTe$ ($x = 0.381$) . (c) Band structure calculations for SnTe. As can be seen from the band structures for all the compounds in the TCI phase, the location of the band inversion is analogous to that of SnTe. (d) For both $Pb_{1-x}Sn_xTe$ and $Pb_{1-x}Sn_xSe$ the location of the band inversion is at $\bar{X}$ in momentum space. *Figure adapted from [3, 4].*

nm, Sn = 0.142 nm).

One would expect PbTe to be a TI as it shares a similar structure to PbSe and SnTe but this is not the case. This is illustrated in Figure 1.7, where a crossover at the Fermi surface or the formation of a Dirac node is observed only when the composition moves towards that of SnTe.

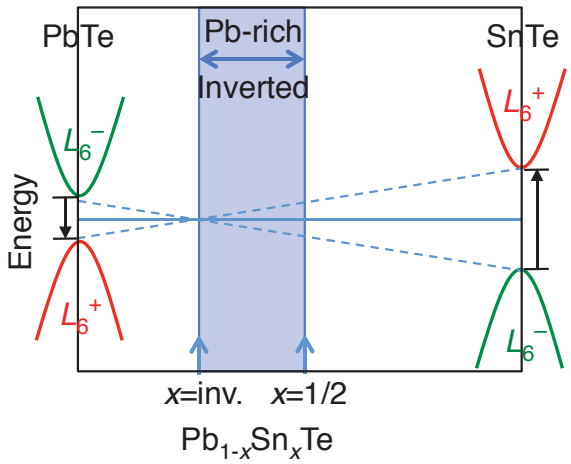

Figure 1.7: Bulk band gapped PbTe transition to non-trivial insulator like SnTe. The topological phase transition occurs at a critical Sn concentration. *Figure adapted from [2].*

The parent compounds for $Pb_{1-x}Sn_xSe$ are PbSe and SnSe. The former crystallises in the rock-salt structure however SnSe forms an orthorhombic crystal (Figure 1.8). Upon the creation of the solid solution $Pb_{1-x}Sn_xSe$, the structure remains cubic for Sn concentrations upto $x \leq 0.4$. The tunable bad gap of these materials is the driving force for the interest in them. External factors such as electric field or lattice strain can cause a TCI transition that could lead to various potential applications.

There are two factors which affect the band gap of this material, allowing it to have an inverted band gap state which is a common feature for TCIs. The first is the Sn concentration in the solid solution. It has been determined by work published by Dziawa *et al.* that there is a closing of

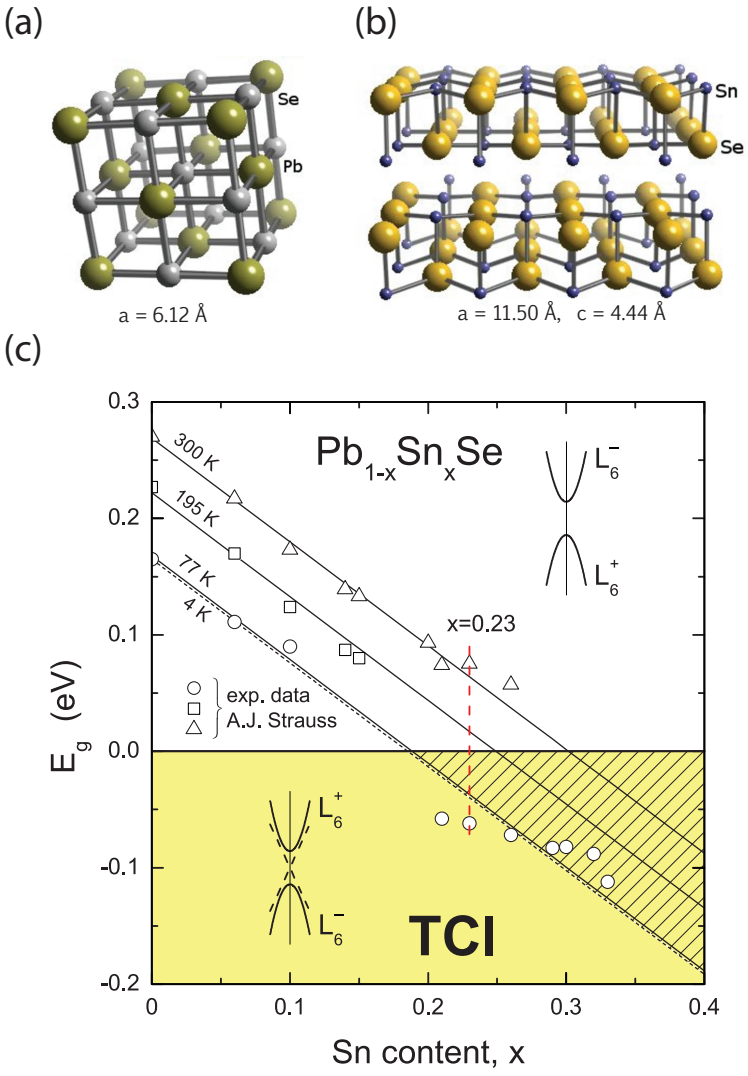

Figure 1.8: (a) Lattice structure of cubic PbSe and (b)orthorhombic SnSe. (c) Solid solutions of $Pb_{1-x}Sn_xSe$ showing the development of the TCI transition wrt. Sn concentration and temperature. *Figure adapted from [3].*

the band gap as the Sn concentration increases. At a critical composition, the band gap begins to reopen and the system enters a TCI phase. This critical composition is $x = 0.23$. The introduction of Sn atoms into the lattice is the source of the strain within the crystal structure. The second factor affecting the TCI transition is temperature where the TCI phase dissapears at temperatures above the critical temperature, $T_c = 250$ K.

1.2.3 Sb_2Te_3

The 3D topological insulators were amongst the first group of materials to have their surface states directly probed for TI behaviour. These materials were quick to have their predicted TI nature confirmed (predicted by Hsieh *et al.*) and observed by Zhang *et al.* in the same year - 2009). [56, 57]

Sb_2Te_3 along with Bi_2Te_3, Bi_2Se_3 are good candidates for studying TI properties as they had well-defined electronic structures and simple surface states. This was important when first identifying a set of materials that were thought to be part of this new state of matter, TIs.

All these materials contain five atoms in a single unit cell and form a rhomboidal crystal structure with a D^5_{3d} space group. The crystal is formed as layers that are weakly bound by van der Waals forces. The *ab-initio* calculations performed by Zhang *et al.* showing that the materials they had chosen for study, were indeed insulators where the conduction and valence bands had opposing parity and that there was the presence of a single Dirac cone where the band inversion occurred at the Γ point in the Brillouin zone. Detailed surface studies of Sb_2Te_3 were performed by Hsieh, Xia, Qian, Wray *et al* using ARPES (see Figure 1.9).

Sb_2Te_3, has in the past been the subject of much interest because of its thermoelectric properties making them useful for use in data storage media and phase change random access memory (PRAM). There has been a revival in research on Sb_2Te_3 due to the topological insulating proper-

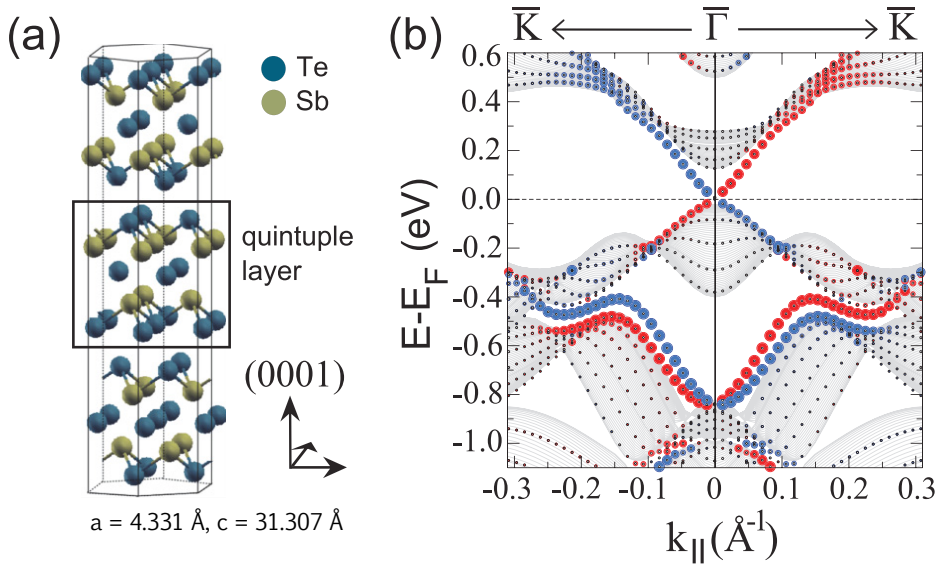

Figure 1.9: (a) Structure of Sb_2Te_3. (b) Band structure determined by DFT showing a Dirac cone at the Γ location. *Figure adapted from [5].*

ties which have been observed experimentally in similar layered crystals, namely Bi_2Te_3 & Bi_2Se_3.

Sb_2Te_3 has been shown to be a topological insulator, however, the material can become superconducting under certain conditions. [5] This superconductivity has been experimentally observed at higher pressures, or by way of increasing the carrier concentration with the presence of excess Te during growth. [7]

There is further interest in Sb_2Te_3 as it can be made superconducting at ambient pressures provided the samples are grown in a Te overpressure. Bulk crystals of this material have also shown a pressure induced superconductivity where a max T_c of $\approx$ 7.5 K is observed at 30 GPa (Fig. 1.11). [7] This again raises the possibility of investigating new physics and phenomena through TI materials that are superconducting.

Due to the weakly bound quintuple layers in Sb_2Te_3, the material lends itself to be easily cleaved and manipulated. Sb_2Te_3 can been thinned to 2D layers using a Scotch tape method much like that of graphene from

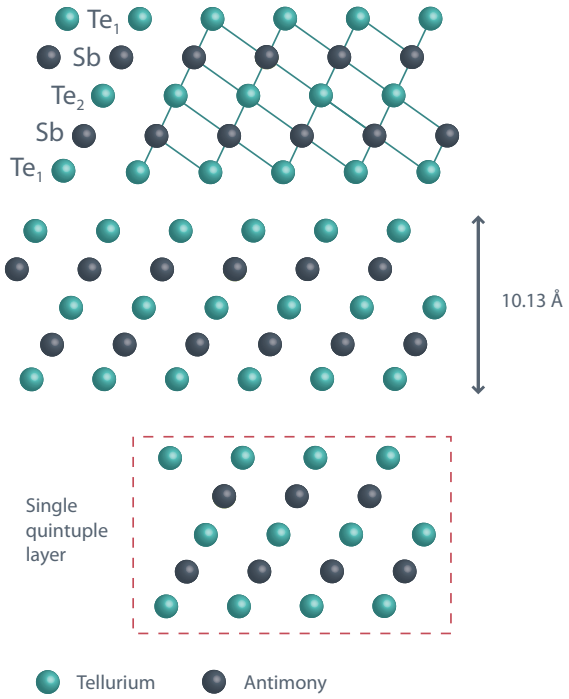

Figure 1.10: Schematic of the crystal structure of Sb_2Te_3. Tellurium atoms occupying different sites have been identified as has the quintuple layer which is weakly bound to adjacent layers. (Te = green & red, Sb = grey) (Lattice constant: [6])

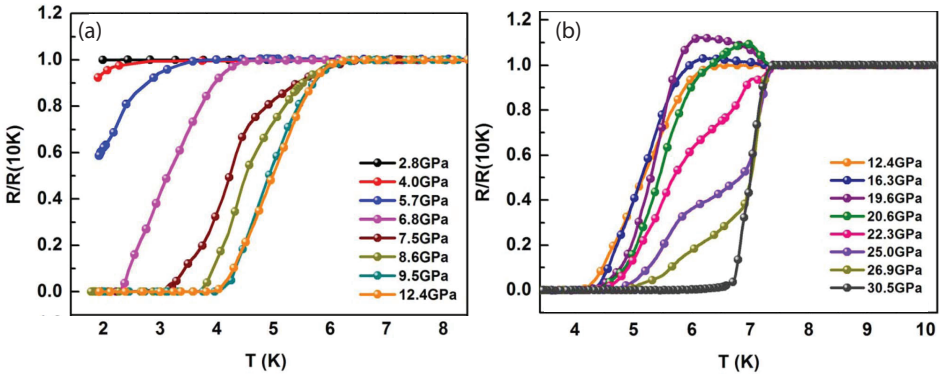

Figure 1.11: Temperature dependent resistance measurement for Sb_2Te_3 under various pressures. (a) 2.8 GPa o 12.4 GPa (b)12.4 GPa to 30.5 GPa. *Figure adapted from [7].*

high orientated pyrolytic graphite. [58] Combining this with the thermoelectric properties of Sb_2Te_3 and others mentioned above, interlayering this material with graphene creates many interesting prospects. Research in this area is very new and producing graphene/TI multilayers is challenging. Ensuring an oxide free interface between graphene and Sb_2Te_3 is one such complication and growth techniques such as molecular beam epitaxy and atomic layer deposition have been explored. However, these techniques present their own problems such as interlayer diffusion. [59] We present preliminary results for some of the avenues that have been pursued to produce such materials (Chapter 5) using an alternative direct growth technique.

Finally, the layered structure of Sb_2Te_3 can also be exploited as there is intense research in the fabrication of multilayer chalcogenide devices some of which include intercalation with graphene. Combining the exciting electronic properties of graphene with those of TIs brings about the prospect of many new research opportunities. Examples of such studies include multilayers of Bi_2Te_3/Sb_2Te_3 to manufacture cooling thermoelectric devices and Ge/Sb_2Te_3 nanocomposite multilayer films for PRAM applications. [60] Studies with graphene intercalation are at an early stage with only a handfull of methods that describe the manufacture of such devices and the processes involved. [59, 61, 62]

Sb_2Te_3 is a semi-conductor that can be made both *n*-type or *p*-type-type. Usually the growth of this material leads to an over stoichiometry of Sb on Te sites. This leads to a high hole carrier density. Growing the material with a Te overpressure reduces this effect to make the semiconductor more p-type by lifting the Fermi level towards to bulk band gap. The structure of the *p*-type topological material Sb_2Te_3 is rhombohedral (space group D^5_{3d} and similar to the tetradymite structure of Bi_2Te_2S. [63] A schematic of the crystal structure of Sb_2Te_3 can be seen in Figure 1.10. The material forms 2D quintuple layers which are weakly bound by van der Waals bonding, however, from neutron scattering experiments

and later photoemission studies, long-range coulomb forces also play a role in adjacent Te layers. [64] Each layer comprising of Te_1-Sb-Te_2-Sb-Te_1 alternately stacked atoms is approximately 1 nm thick. The lattice constants are $a = 4.25$ Å and $c = 30.4$ Å. [65]

Sb_2Te_3 has also been widely studied in the form of nanowires. In the past, the main driving force for the formation of Sb_2Te_3 as nanowires were their use in PRAM devices as nanowires offered a better packing density and increased efficiency. We will investigate an alternative growth method for the growth of Sb_2Te_3 nanowires in the hope that future studies can more easily reveal their topological insulating properties than when they are in the form of bulk crystals.

Topological superconductivity is a new property of materials that fall into the category of novel topological quantum states of matter. Some TI materials have been shown to undergo a superconducting transition when they are not in thier normal state. For example, bulk superconductivity in some of the first TI materials discovered, Bi_2Se_3 and Bi_2Te_3, has been observed. The superconducting transition in Bi_2Se_3 was observed at 3.8 K when Cu was used to intercalate the structure between the quintuple layers that make up the Bi_2Se_3 structure. [66] Superconductivity was also observed in Bi_2Te_3 when a higher pressure is applied on the crystal structure. [67]

Sb_2Te_3 can also be made superconducting at ambient pressures, provided the crystals are grown in specific conditions. When Sb_2Te_3 samples are grown within the narrow Te vapour pressure range of 1.2 - 1.5 MPa, the resulting crystals are superconducting. It had been previously thought the origin of the superconducting state in Sb_2Te_3, when using a dopant or external pressure, was due to the bulk carriers of the material, as the carrier densities in these materials were high. As well as detecting a superconducting signal in bulk materials, a superconducting signal limited to the surface of bulk materials has also been observed on small exfoliated crystals. [8]

Tuning the electronic structure with a chemical dopant to change the superconducting properties of the material, or to induce it entirely, is common practise within the field. A physical process such as applying a higher pressure can also achieve similar effects without the disadvantage of introducing a change to the chemical composition of the system, as would be the case with intercalation of the crystal structure with metallic dopants. [7] The work by Zhu *et al.* demonstrated the reduction of the superconducting transition from $\approx$ 6 K to 3 K in Sb_2Te_3, when the pressure changed from $\approx$ 8 GPa to 4 GPa. Further details on the effect of pressure changes to the superconducting transition can be found in Chapter 1, section 1.2.3.

It is thought that producing materials with a greater surface-area-to-volume ratio allows for the easier detection of these surface properties as the signal arising from the bulk with respect to the surface is lowered. It is for this reason that the results shown by Zhao *et al.* were interesting as they had demonstrated surface superconductivity when growing *p*-type Sb_2Te_3 using a modified Bridgman growth method during which there was a Te overpressure. The Te overpressure did not affect the stoichiometry of the material (in a narrow range), however, it did allow for a reduction in the hole carrier density by compensating bulk carriers - the result of which is increased mobility. A superconducting transition of $T_c \approx$ 9 K was reported by Zhao *et al.* [8].

Sb_2Te_3 nanomaterials can be grown on several substrates. The possibility of exploiting the TI properties of Sb_2Te_3 with those of the spin-orbit interactions in graphene, can potentially lead to the discovery of new spin transport structures and quantum phenomena (such as Majorana fermions). The thermoelectric properties of such systems combined with those predicted in graphene also raises the interesting application in new solid state devices. [59, 68] We have investigated the direct growth of Sb_2Te_3 in the form of layers on graphene to achieve a reliable growth process which can in the future be utilised to investigate new multilayer

systems.

1.3 Outline of the thesis

This section covers the outline and layout of the thesis. Chapter 2 describes the various scientific characterisation tools that are utilised to ascertain the quality of the samples produced in both bulk and nanoforms. Chapters 3 to 5 are experimental results chapters.

Chapter 3 is divided into two sections. The first describes the results on the superconducting compound, Sn_{1-x}-In_xTe and the topological crystalline insulator SnTe. The main characterisation techniques used include magnetic susceptibility measurements and scanning electron microscopy. The second section will focus on the surface preparation of microcrystals of the TCI, SnTe. This section will give an insight into one of the greatest challenges facing the study of topological materials in nanoform. X-ray photoelectron spectroscopy studies are presented for various surface cleaning methods used on one of the materials chosen, SnTe. This section will in part, provide a solution to the difficulties currently encountered in detecting surface states in topological insulators using surface sensitive measurements such as angle-resolved photoelectron spectroscopy.

Chapter 4 focuses on the compounds $Pb_{1-x}Sn_xTe$ and $Pb_{1-x}Sn_xSe$. The methods used to grow bulk crystals of these materials will be discussed followed by the fabrication techniques of these materials as nanomaterials. Techniques used to characterise bulk crystals will include powder x-ray diffraction and Laue back scatter diffraction. The nanomaterials produced will be characterised using a mixture of transmission electron microscopy and scanning electron microscopy.

Chapter 5 discusses the progress made in investigating Sb_2Te_3. Resistivity measurements will be used to investigate the superconducting properties of this material. The methods used to grow Sb_2Te_3 as nanomaterials and 2D layers will also be presented. Characterisation of these

materials will also use atomic force microscopy and Raman spectroscopy as well as conventional microscopy imaging techniques.

Chapter 6 will provide a summary of the concepts covered and the conclusions made from the results obtained. This section will also focus on investigations that are to be carried out in the future and the interesting physics that those experiments can yield.

Chapter 2

Experimental Techniques

2.1 Growth Processes

A corner stone to ensuring reliable and repeatable results when growing crystals and nanomaterials is to completely understand the growth processes taking place. It has been described as a dark art however with a well characterised growth system, subtle changes in the growth parameters can be used to achieve the desired growth methods and in turn, the morphology of the materials required. This chapter focusses on describing the various growth methods utilised and behind those, the processes governing them.

2.1.1 Modified Bridgman method

P. W. Bridgman, after which the technique is named, first reported this growth method in 1925. [69] Typically, in the original Bridgman method, a crucible or quartz ampoule containing the solid mixture is lowered through a temperature gradient using a motor capable of movements between $\approx$ 0.5 to 500 mm/h. A melt forms as the ampoule approaches the highest temperature and solidifies as its passes through the central hot zone. The

melt slowly moves up the ampoule leaving behind a crystalline sample. The crystallisation can be promoted with the use of a seed crystal at the base of the ampoule. Without a seed, the crystal will nucleate randomly decreasing the likelihood of the producing a single crystal.

The shape of the ampoule also plays a roll in the nucleation and development of the crystal during growth. Typically, an ampoule will have a pointy end and is made of a material that has a coefficient of thermal expansion smaller than the crystal to avoid developing strain in the crystal. The quartz ampoule can be evacuated to reduce contamination in the crystal during growth or back filled with an inert gas such as argon. An example for when adjusting the pressure within the ampoule is desirable is dependant on whether one wants to control the various vapour pressures of the elements within the mixture, and the growth temperature the ampoule is expected to achieve. The crystal boules that are described in the following chapters have been sealed under vacuum.

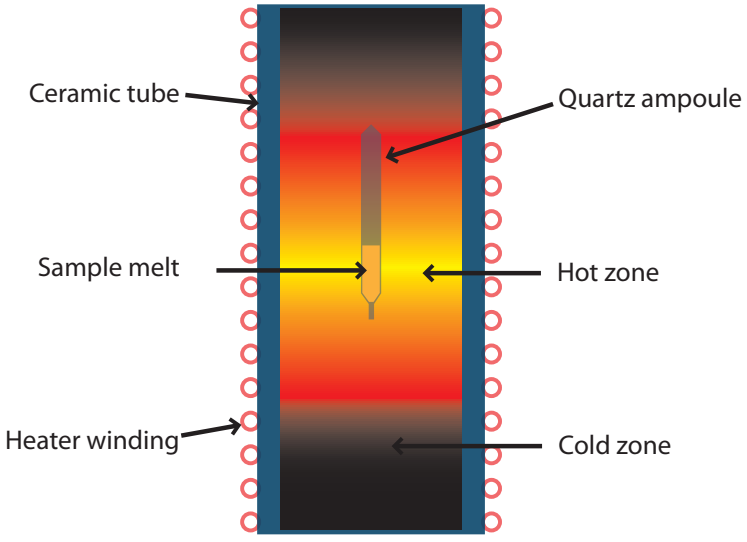

Figure 2.1: The vertical Bridgman method

The modified Bridgman method involves a static growth setup where the ampoule is typically placed vertically in a box furnace. The temper-

ature of the furnace is slowly ramped to a target temperature where the material in the ampoule begins to melt. The furnace then remains at this temperature during the dwell stage. This stage should be long enough to allow complete and even diffusion all all the materials in the melt. This will ensure an even stoichiometric mix within the final crystal. In the modified Bridgman method, all the starting material (in the form of powders, shot or crushed crystal) will form a melt, unlike a travelling melt in the original Bridgman method. This again decreased the likelihood of a single crystal forming as nucleation will occur at various points within the melt when the cooling cycle is initiated. Finally, the furnace temperature is slowly reduced allowing crystallisation of the melt to take place. To monitor the temperatures within the growth furnaces, a K-type thermocouple is placed as close to the centre of the furnace as possible. This is also the location in which the ampoule is placed and is supported vertically in a ceramic base. The modified Bridgman method was mainly used in the production of crystal samples for the studies presented in this text and are described in the chapters to follow. Figure 2.1 shows a schematic of the vertical Bridgman method.

2.1.2 Introduction to the CVD method

The use of chemical vapour deposition (CVD) to grow nanomaterials is a well established method. It is the main reason for choosing CVD to grow TI's and TCI's in the work presented. The method of synthesizing 1D and 2D materials using CVD is a simple one and as such is also the greatest advantage in using CVD. It is a quick tool for growing nanomaterials and the method can be easily refined to give good reliable results. The growth process was first used for the deposition of thin films, where initially, a chemical vapour can be created from heating the source material. The vapour is then deposited forming solid structures or layers as it transitions from the hotter source region to a cooler substrate region. The type

of growth obtained or desired can be fine tuned by varying four major parameters. The finer details of the process are discussed later in the section. Some popular industrial applications for CVD includes the growth of graphene, synthetic diamonds and silicon wafer layers.

The CVD category covers a variety of processes that are an offshoot to the main principle. These subcategories place emphasis in particular to the environment or method in which the chemical reaction takes place. Such examples include, UHVCVD (ultra high vacuum CVD), PECVD (plasma enhanced CVD) and MOCVD (metalorganic CVD). The CVD classification for the growth of chalcogenide nanomaterials in the work presented is LPCVD (low pressure CVD) which typically covers pressures down to 1 x 10^{-3} mbar.

There are four key principles of every CVD process. Firstly, any reacting gasses formed from the source material has to be transported to the substrate. Secondly, the the reactive gasses must adsorb or absorb on to the surface of the substrate. Third, a reaction takes place between the reactive species and the substrate where finally, excess or unreacted gasses are removed from the substrate surface. A typical setup of a CVD system is shown in Figure 2.2. A temperature calibration is also shown demonstrating the narrow temperature bands in which the source and substrate reside.

As shown in Figure. 2.2, the crucible containing the source material is placed at the centre (hot zone) of the quartz tube. The substrate is placed downstream or towards the cold zone in the tube. The quartz tube is pumped constantly using a rotary vacuum pump and argon is used to flush the system and to provide an inert atmosphere during growth. Furthermore, the argon flow acts as a carrier gas contributing to the drift of the source material towards the cold zone.

There are many parameters that can be controlled in CVD. We begin highlighting the parameters and the general effects caused by adopting one parameter over the other. The outcomes are mostly trivial, however

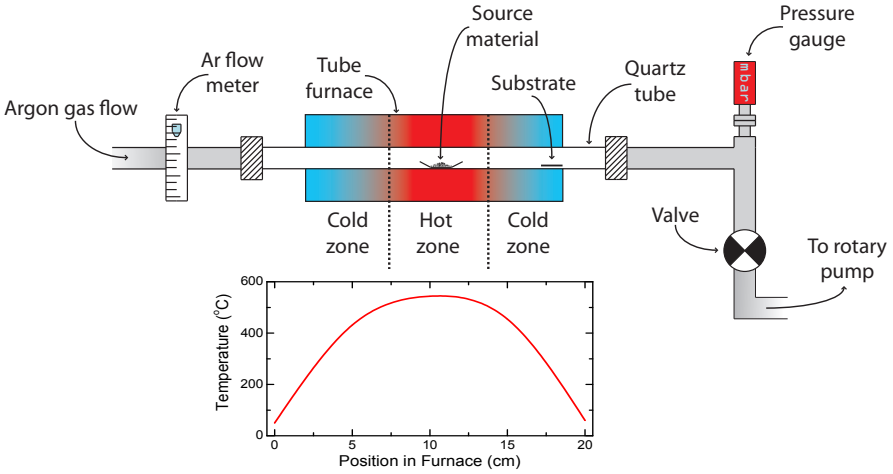

Figure 2.2: (a) Schematic of growth furnace used for the growth of nano materials. (b) Temperature profile of growth furnace.

each parameter has a differing degree of effect on the growth outcome and as such can be less important to control than the other. The two most important variables that are critical to the work presented are the temperature at which the source and substrates are placed within the furnace tube. This parameter is inherently linked to the position of the substrate and the source material within the quartz tube and as such will be used interchangeably when discussing growth results and dynamics. These two parameters control the amount of reacting species evolving at the source which inturn controls the amount of growth that occurs on the substrate. More reacting species will give a greater growth density and usually larger growth morphologies. The flow rate of argon will usually govern the dimensions of the material grown. A slower flow rate allows for the development of fewer but larger growth morphologies per unit of time. Conversely, a quicker flow rate will achieve greater nucleation but the material grown is usually smaller per unit of time. One can also control the amount of source material placed in the crucible and as one would expect, the more source material you have, the greater the number of reacting species that are formed. Finally, the duration of the growth

will dictate the amount of deposition observed.

These are the macroscopic variables that can be controlled for any given growth to find a method which produces repeatable and reliable results. On the microscopic scale, the preparation of the substrate surface will also have an effect on the growth morphologies observed and these are more suitable to discuss in the following section.

2.1.3 Vapour-liquid-solid and vapour-solid growth mechanisms

The vapour-liquid-solid (VLS) or vapour-solid (VS) growth techniques are a common, simple and effective mechanism for growing nano and micro materials. Figure 2.2 shows a basic schematic of the growth furnace that allows for both these processes to be employed in this work. The following sections look at the differences and similarities between both methods and the results they produce.

The VLS mechanism was that used to describe the whisker growth of various 1D crystalline nanostructures in 60's and 70's. The mechanism described the events taking place at the interface between the reacting species created by heating material in the hot zone of a furnace and the substrate.

Typically, a metal catalyst is used on the surface. This can be in the form of a metal layer such as sputtered gold or nanoparticles that have been dispersed on the surface of the substrate. As the reactants reach the metal catalysts, a liquid alloy is formed. As the alloy saturates with the ever increasing presence of reactants, this promotes the precipitation of the reactants into an anisotropic crystalline structure (typically a nanowire). This process continues as the energy required to propagate the growth of the nanowire is less than the nucleation with the substrate. Furthermore, for the VLS process to take place as in the chalcagonides in this work, the materials should have a eutectic point with Au.

As we have identified, the parameters affecting the growth of nanomaterials requires a fine balance of these factors. Lets take an example where the desired growth are nanowires grown using a VLS mechanism. In the case of nanowires, and the desire to obtain a high yield of nanowires, one would expect to have a large number of nucleation sites and therefore a high nucleation rate. It could be assumed that to achieve this, more source material in vapour form is required to create a greater number of reactive species. This argument is in-fact counter productive to the growth of nanowires. The local environment also plays a significant role in the type of growth observed. The resident time, τ, is a value that describes the amount of time a particle or reactive specie stays in a system. $\tau = V/q$ where V is the capacity of the system to hold the the substance and q is the flow rate of the system. If the resident time increases, you approach a growth environment conducive to the growth of nanowires. This agrees well with the type of morphologies observed and described in subsequent chapters.

The VS mechanism of growth is similar to the VLS mechanism with one exception. As the name suggests, no liquid phase is formed at the interface and the growth morphologies observed occur due to solid state diffusion. As a result, no catalyst is required to promote the growth of nanomaterials. These materials still grow forming anisotropic crystalline structures.

In some instances, a VS growth mechanism can dominate after the VLS mechanism in the formation of a nanowire. A schematic of both the VLS and VS growth mechanisms are shown in Figure 2.3, including the transition of the growth mechanism from VLS to VS in some nanowires. This transition yields thicker nanowires as growth is no longer confined to the tip of the nanowire (where the VLS mechanism dominates).

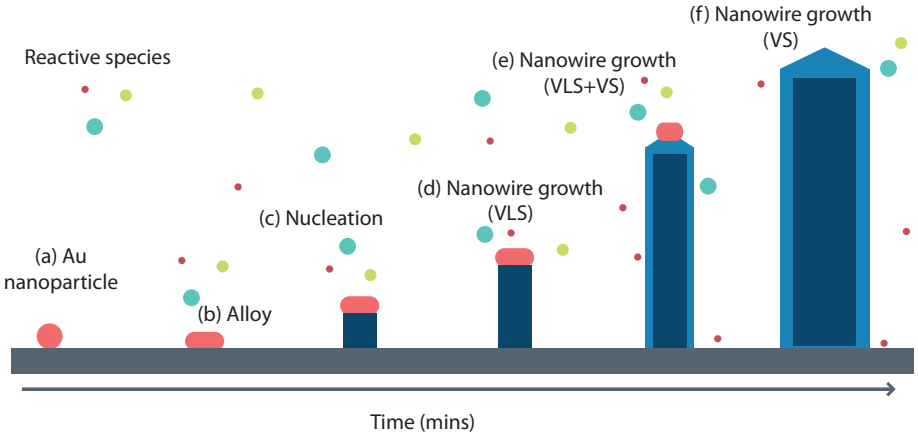

Figure 2.3: A schematic of the VLS and the transition towards VS growth mechanism. (a) A gold nanoparticle on the substrate surface. (b) The reactive species form an alloy with the gold nanoparticle. (c) Nucleation occurs on the substrate. (d) Growth occurs at the tip of the nanowire. (e) Reactive species begin to attach to the body of the nanowire in a VS process. The size of the alloy reduces as it is distributed along the length of the nanowire.(f) When no liquid phase can be formed with the gold nanoparticle, a VS growth mechanism dominates.

2.2 Characterisation Techniques

There are various characterisation techniques that are used to ascertain the quality of bulk crystal samples produced after they are grown using the modified Bridgman method and when they have been converted into nanomaterials. This sections is made of two parts that first address the main techniques that are used for bulk crystals followed by those particular to nanomaterials.

2.2.1 Characterisation of bulk materials

X-ray diffraction

In 1912, Von Laue realised that crystalline materials can behave essentially as diffraction gratings. The regular and periodic arrangement of atoms allows incident x-rays to diffract, providing the incident x-rays are of a wavelength comparable to the lattice separation. By 1914, Bragg's theory of diffraction was established, where parallel planes of atoms were considered to reflect incoming radiation. A diagram demonstrating this principle can be seen in Figure 2.4.

Bragg's law states that two waves have to be scattered and in phase for constructive interference to occur. This translated to a set of conditions where constructive interference could take place, or alternatively, a set of conditions for diffraction to occur. As a result, two waves entering a crystal lattice will be in phase if they are separated by a whole number of wavelengths, $n\lambda$, and the route taken by these two waves between adjacent planes will have a path difference of $\delta\ L$. The angle, θ, of the incident x-ray is also known and thus the scattering angle, 2θ. Furthermore the separation between one plane and the next is a distance, d. A combination of all these give Equation 2.1 and the Bragg condition for detecting a scattering signal.

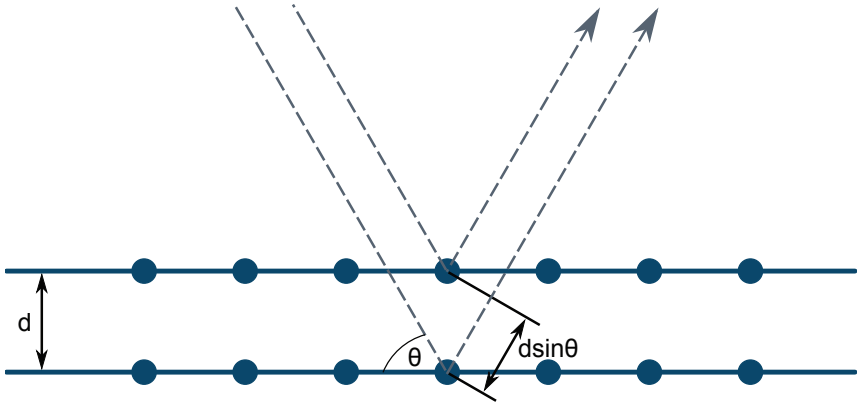

Figure 2.4: Two beams scatter of two different atoms within the crystal lattice and constructive interference occurs when the length, $dsin\theta$, equals an integer value of the wavelength of the incident radiation.

$$n\ \lambda = 2dsin\theta \tag{2.1}$$

XRD is used primarily for two reasons. The first was to determine the lattice parameter from a powder crystal diffractogram. The second is to ascertain the phase purity of the sample. Taking the first case, peaks arising from diffractions that satisfy the Bragg condition are indexed with the Miller indices associated or allowed with those reflections. From this, the d-spacing is obtained as the wavelength of the incident x-rays are known. For the diffractograms presented in this thesis, a Siemens D5000 diffractometer was used capable of producing Cu Kα radiation. Crystals were ground finely and packed into the sample holder. To remove the effects of preferential packing, the sample holder is set to spinning during data acquisition. A typical 2θ scan ranged from 20 to 90 deg. For the latter case, the presence of extra peaks in the diffractogram would suggest multiple phases present in the sample, as well as shifts in the lattice parameter.

Laue diffraction

The technique is mainly used to determine the orientation of large single crystals and the quality of those produced. An x-ray beam is focused onto the sample and the resulting diffracted beams form arrays of spots on the TeGaOS scintillator which has a peak emission of 500nm which matches that of the CCD camera. The beam used is not monochromated and allows for multiple scattering events simultaneously. Again, the Bragg angle is fixed for every set of planes in the crystal. Crystal orientation is determined from the position of the spots. Each spot can be indexed and attributed to a particular plane. The Laue technique can also be used to assess the quality of a crystal. The size and shape of the diffracted spots give an insight into the perfection of the crystal. If there is strain within the crystal, or multiple crystals with a boule, the spots become distorted and smeared out. The diffraction pattern may change depending on the orientation of the crystal with respect to the incident x-ray beam and a goniometer can be used to align the crystal in a particular orientation. Crystals boules that are characterised with Laue diffraction are conical in shape. Using a three axis goniometer, Laue diffraction can be performed every 2 mm on the surface of the crystal along both the face and the length of the boule. This will give an indication of the approximate size of the crystals that have formed within the boule.

Compositional analysis

An important tool in determining the composition of the crystals produced is the use of Energy Dispersive X-ray Analysis (EDX, although it is also known to be abbreviated to EDAX and EDS). An EDX detector is usually placed within an SEM imaging system. The incident electrons on the sample surface causes the emission of x-rays with discrete energies.

These arise due to the inelastic scattering of the incident electron with that of a core level electron in the inner orbital causing an outer

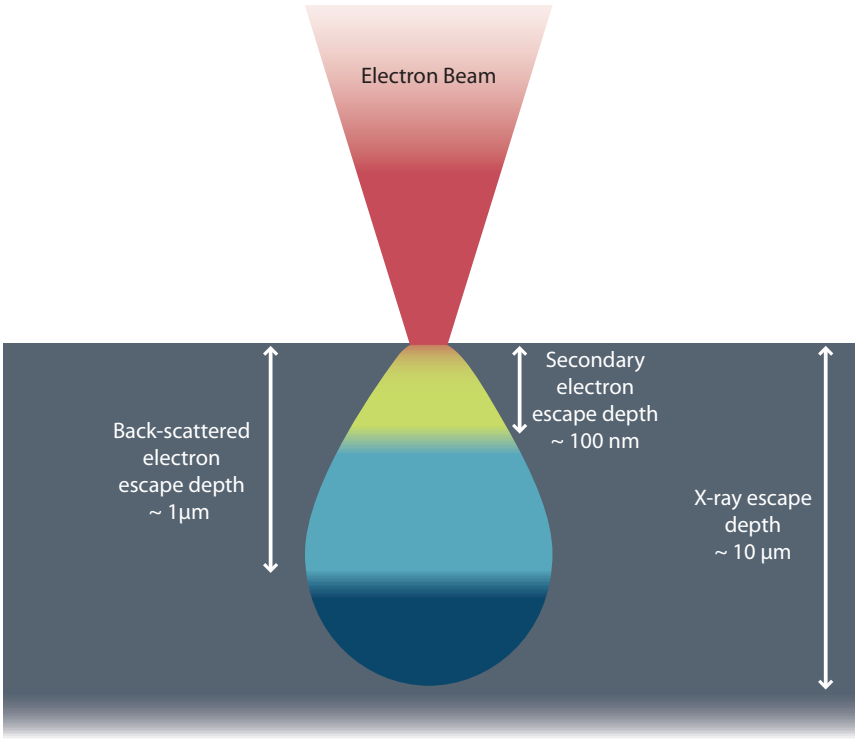

Figure 2.5: Schematic of the interaction volume and the locations of the various interaction processes.

shell electron to take its place. This interaction liberates a photon with an energy equal to the energy change of the electron which has moved from the outer shell to a lower energy shell. The photons collected over a wide energy range give rise to a spectra containing information on the elements present and more importantly the quantities of each.

There are some physical properties of the sample which will affect the results for the composition of a material. These include the sample topography and geometry with respect to the detector. Other factors include x-ray absorption by the sample, florescence and the limited spatial resolution or beam width. Lighter elements are difficult to detect due to the detectors absorbing low energy x-rays. The accuracy of an EDX system in determining elemental compositions is $\approx 2\,\%$ and because of the interaction volume shown in Figure 2.5, this characterisation technique is limited to bulk samples and large microcrystals. Typical escape depths for secondary electrons, back-scattered electrons and x-rays are also shown.

For the studies presented herein, a Zeiss SUPRA 55-VP scanning electron microscope with an EDAX spectrometer was used to obtain information of the stoichiometry of the materials grown. Electron accelerating voltages of 20 kV were used for the measurement of bulk materials with a thickness of ≈ 20 μm.

Magnetic susceptibility

The magnetisation data presented in Chapter 3 was obtained on a Quantum Design Magnetic Properties Measurement System (QDMPMS) and utilised a superconducting quantum interference device (SQUID). The magnetometer comprises of two Josephson junctions in a superconducting ring. A current is induced as the sample passes through a magnet. The SQUID device is a current to voltage converter. The voltage response is mapped to a known response such as palladium to give the magnetic moment of the sample. The susceptibility is the magnetic moment divided by the applied field.

In order to conduct the measurement, small pieces of the crystal boule are isolated and placed in a gel capsule with a very small (in comparison to a superconducting signal) response. The sample/gel capsule is then cooled in zero field at which point a magnetic filed is applied (20 Oe). As the sample is warmed/cooled inside the magnetic field, the voltage response is measured. Magnetic susceptibility measurements on the $Sn_{1-x}In_xTe$ crystals to determine the superconducting transition temperature were taken between 2 and 10 K. An applied field of 20 Oe was used as this was sufficient to obtain a magnetic response and was well below the critical field of the samples where the Meissner effect breaks down.

Resistivity and Hall measurements

Resistivity measurements are conducted by attaching four silver wires of diameter 0.05 mm to the sample surface using DuPont 4929N silver paint. Figure 2.6 shows a schematic of the four probe measurement.

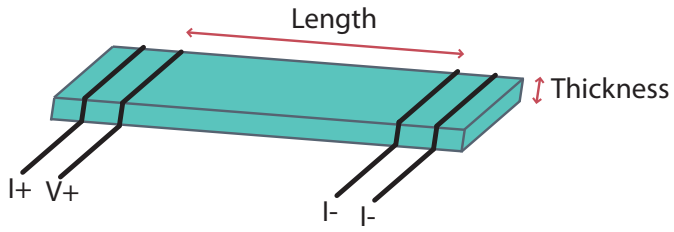

Figure 2.6: Schematic of the position of the voltage and current leads for a four probe measurement.

A current is applied and a voltage difference is measured over a short distance, L. The cross sectional area, A, is determined and these measured values allow for the calculation of the samples resistivity using Equation 2.2.

$$\rho = RA/L \tag{2.2}$$

Voltage and current measurements are taken from temperatures of 300

K down to 2 K using a Quantum Design Physical Properties Measurement System (PPMS). Samples are typically upto 5 mm long, 1 mm wide and 0.25 mm thick.

Hall measurements can be used to obtain electronic properties of materials such as the carrier density. A Van der Pauw measurement method was used to obtain the carrier concentration of flakes of Sb_2Te_3 cleaved from crystal boules (Chapter 5).

2.2.2 Characterisation of Nanomaterials

SEM

In this work, high resolution scanning electron microscopy(SEM) images were taken with a Zeiss Supra55 microscope. All contrast in SEM images is due to the different number of scattered electrons detected [70]. Backscattered electrons provide information about Z-contrast and secondary electrons provide topographical information. The secondary electrons are detected using the in-lens detector for high contrast surface imaging. There are other factors that can add or subtract contrast to images and these arise from sample tilt, changes in acceleration voltage and beam spot size. An optical image can be seen in Figure 2.7 showing a typical silicon substrate post nanogrowth.

Figure 2.7: Typical optical image of silicon substrate post growth.

In SEM, a high energy electron beam (up to 40 keV) is focused onto the sample (beam spot typically 4 - 5 nm) causing a variety of interactions that can be used to characterise the sample being analysed. SEM is

carried out under vacuum to obtain the electron mean free path required for imagery. A vacuum also reduces the adsorption of contamination whilst imaging and preserves the stability of the beam, which is controlled using electrostatic lenses. Secondary electrons emitted from the sample surface are commonly used to indicate morphology and topography of the surface. Using a positive potential, secondary electrons emitted from the surface of the sample are directed towards a detector and photomultiplier producing an image. Spatial resolutions of 50 to 100 nm can be obtained. In this study, all images shown are taken with the electron beam at 10 or 20 keV depending on the thickness of the materials being investigated.

Electron Backscatter Diffraction

Backscattered electrons can be used to determine crystallographic orientations. In electron backscatter diffraction (EBSD), electrons are backscattered and diffracted according to Bragg's law, giving rise to diffraction patterns or Kikuchi bands. The surface crystal orientation can be indexed using Miller indices. Within the scope of this study, EBSD was used to index the crystal orientations in CVD grown microcrystals. The probing depth of EBSD is greater than that of other techniques that can achieve similar results such as low energy electron diffraction. The sample is tilted at grazing angles to optimise the contrast obtained, as at lower tilt angles the contrast in the diffraction pattern decreases. Figure 2.8 shows the Kikuchi bands which are indexed to reveal the surface orientation for a crystal (Silicon).

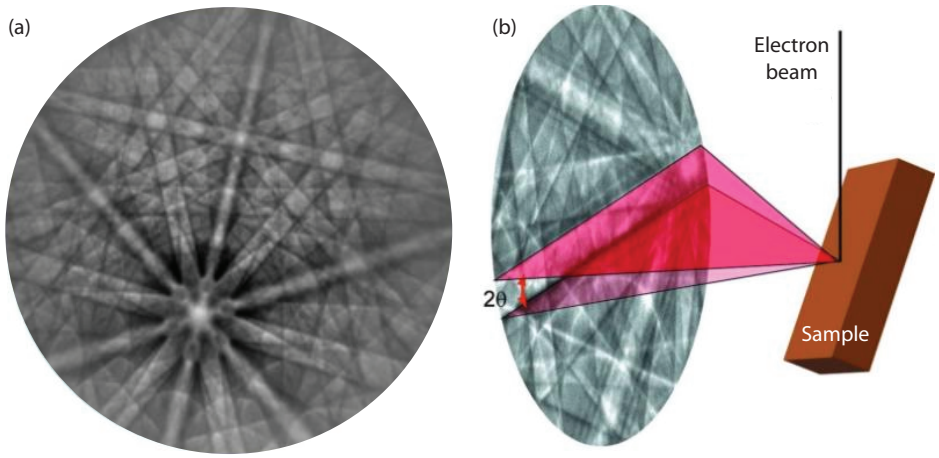

Figure 2.8: (a) Schematic showing the Kikuchi bands which are formed through EBSD as detected on the CCD camera. These bands are later indexed to reveal the crystalline surface orientation from a stereogram. (b) Schematic of sample and detector geometry for EBSD measurement.

Raman Spectroscopy

Information about atomic vibrations can be obtained using Raman spectroscopy. This information can be used to identify samples and to quantify their chemical make up. It can be interpreted similar to infrared absorption spectroscopy. In Raman spectroscopy, monochromatic laser light is shone onto the surface of a sample and the scattered light is detected. The majority of the incident photons undergo Rayleigh scattering, however, approximately 1 in 10,000 photons are scattered with a different energy to that of the incident photons. These photons interact with vibrational energy levels of the atoms in the sample. Raman spectroscopy is a non destructive characterisation technique that is fast to use with little sample preparation. It is also a surface specific characterisation tool much like in x-ray photoelectron spectroscopy (XPS).

Chapter 3

The TCI SnTe and $Sn_{1-x}In_xTe$ ($0 \leq x \leq 0.45$)

In this chapter, we first discuss the growth and characterisation of $Sn_{1-x}In_xTe$ crystal boules for $0 \leq x \leq 0.45$. From these, the growth of $Sn_{1-x}In_xTe$ nanostructures using a Au-catalysed VLS growth technique is shown. The optimum growth conditions are presented to obtain nanowires and microcrystals of $Sn_{1-x}In_xTe$. Characterisation performed on the materials grown include powder x-ray diffraction (XRD), x-ray Laue diffraction, scanning electron microscopy (SEM), energy dispersive x-ray analysis (EDAX), EBSD. For $Sn_{1-x}In_xTe$ for $0 \leq x \leq 0.45$, the magnetisation response of cleaved pieces of the crystal boules has been carried out to study the superconducting properties.

The latter part of the chapter will then focus on the surface preparation of the SnTe microcrystals produced, in preparation for surface sensitive measurements such as ARPES.

3.1 Sample preparation & characterisation of $Sn_{1-x}In_xTe$ crystals in bulk and nanoform

We begin by detailing the procedure for the growth of bulk crystals of $Sn_{1-x}In_xTe$ for $0 \leq x \leq 0.45$. By following the procedure reported by Tanaka *et al*, crystal boules of $Sn_{1-x}In_xTe$ were produced. Samples of $Sn_{1-x}In_xTe$ for $x = 0$, 0.38, 0.40, 0.42, and 0.45, were prepared by the modified Bridgman method. Stoichiometric ratios of the starting materials, 99.99% Sn,(shot) In (shot) and Te (powder), were placed in evacuated quartz tubes.

As stated previously, four compositions of $Sn_{1-x}In_xTe$ were grown around the optimum composition. SnTe crystal boules were also produced which were later used as starting materials for the growth of nanomaterials.

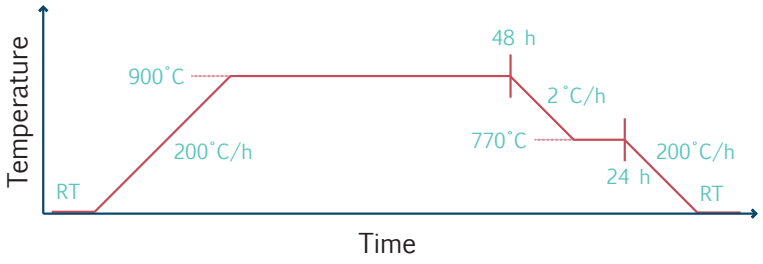

Figure 3.1: Typical temperature profile used for $Sn_{1-x}In_xTe$ crystal growth.

The contents of the tubes were then sealed in evacuated quartz tubes. The quartz tubes were placed vertically into a box furnace and the contents melted at 900 °C. The quartz tubes remained at this elevated temperature for two days. The tubes were then slow cooled (2 °C/h) to 770 °C and then rapidly cooled down to room temperature. A typical growth profile can be found in Figure 3.1.

To check the phase purity, a small section of the boule was finely ground and powder x-ray diffraction patterns were obtained using a Panalytical X'Pert Pro system with monochromatic CuKα_1 radiation. X-ray Laue diffraction was performed on the crystal boules and across the faces of cleaved sections of the boule to check the quality of the crystals produced. Finally, the stoichiometry was determined using an EDAX EBSD system installed alongside a Zeiss SUPRA 55-VP scanning electron microscope.

Upon removal of the bulk crystal boules from the sealed quartz tubes, a visual inspection of the crystal boules revealed shiny metallic surfaces. The crystal boules cleaved easily revealing flat mirror surfaces.

3.1.1 X-ray diffraction

A small section of the crystal boules were isolated and ground into a fine powder for characterisation using powder XRD. A multitude of crystals were grown of varying In concentration. The XRD data shown in Figure 3.2 shows that the pure SnTe crystals grown were single phase with no impurities. For x compositions $0.38 \leq x \leq 0.45$, a few Bragg peaks for the InTe phase could be seen, which became enhanced with the increase of In. This shows that single phase materials were obtained for compositions upto x $\leq$ 0.3. Crystals grown by Zhong *et al.* have showed that for In substitutions of $x \geq$ 0.6, only the InTe tetragonal phase is visible. [28]

Laue diffraction (Figure 3.3) was performed on several freshly cleaved surfaces which revealed well defined sharp diffraction spots.

It was found that the majority of crystals cleaved along the $\{100\}$ and $\{111\}$ planes. The XRD patterns were collected at room temperature. The patterns observed for the $Sn_{1-x}In_xTe$ powdered samples are similar to that of the parent compound SnTe which has a cubic $Fm\bar{3}m$ structure. They are also similar to data published for $Sn_{1-x}In_xTe$ with varying

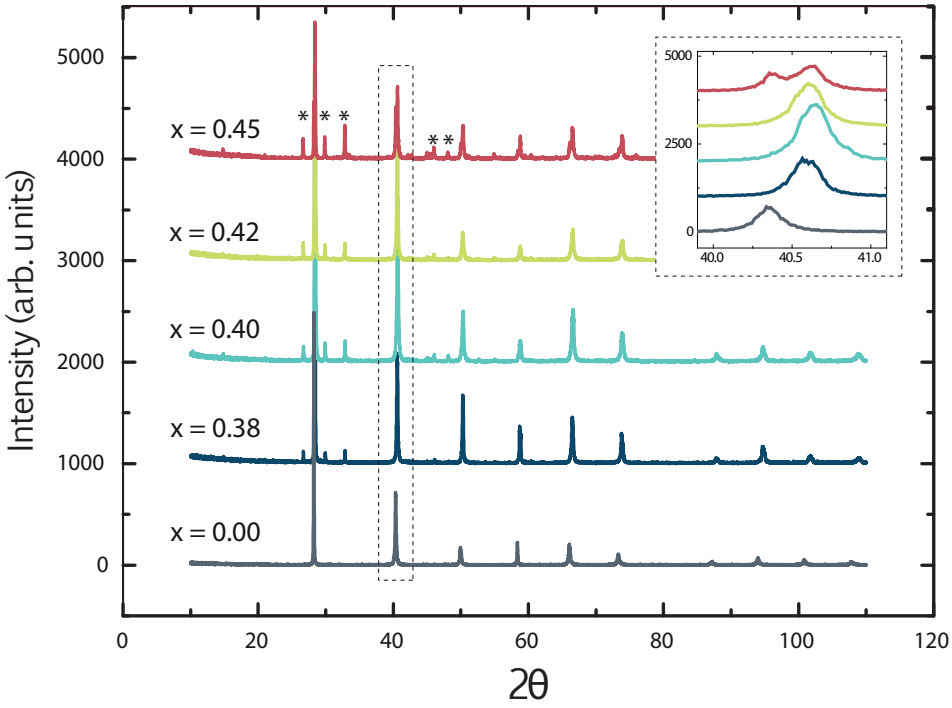

Figure 3.2: Powder x-ray diffraction pattern of a crushed sample of the as-grown $Sn_{1-x}In_xTe$ crystal (composition $x = 0$, 0.38, 0.40, 0.42, and 0.45). The data obtained and the expected Bragg peak positions are shown. The InTe phase has been highlighted with asterisks.

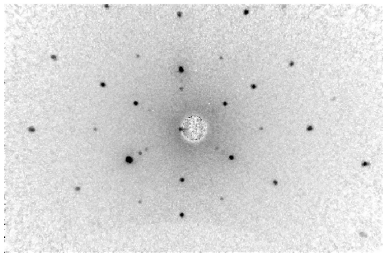

Figure 3.3: Typical Laue pattern of the as-grown crystal boule. The crystal is aligned along the the [111] crystallographic direction. The Laue patterns were consistent across the surface of the boule.

In doping levels. [28,71] The lattice parameters calculated from peak positions in the data agree with those cited in literature and are shown in Table 3.1. The lattice parameter increases with greater In substitution up to $x \approx 0.40$ after which the value for the lattice parameter remains approximately constant.

Composition, x	a (Å)
0.38	6.280(9)
0.40	6.280(1)
0.42	6.279(6)
0.45	6.275(1)

Table 3.1: Room temperature lattice parameter a determined from the powder x-ray patterns for the samples of $Sn_{1-x}In_xTe$ with $x = 0$, 0.38, 0.40, 0.42, and 0.45. The samples are all cubic (Space group $Fm\bar{3}m$).

3.1.2 Compositional Analysis

Compositional analysis using EDAX was performed on several small pieces of crystal obtained from different regions of the boule. The data revealed that the crystals had formed stoichiometrically for all compositions of x as can be seen in Table 3.2.

Table 3.2: Representative compositions for bulk $Sn_{1-x}In_xTe$ crystal boules, where $x = 0$, 0.38, 0.40, 0.42, and 0.45. All values are atomic percent.

Composition, x	Sn (%)	In (%)	Te (%)
0.00	51(2)	-	48(2)
0.38	38(2)	62(2)	48(2)
0.40	40(2)	60(2)	47(2)
0.42	42(2)	58(2)	47(2)
0.45	45(2)	55(5)	49(2)

3.1.3 Superconducting properties of $Sn_{1-x}In_xTe$

Observing superconducting topological insulators has further fuelled interest in this field of work. The experimental observation showing that Bi_2Se_3 could be made superconducting by intercalating the Bi and Se layers with Cu forming $Cu_xBi_2Se_3$ added to the interest generated from the discovery of a gapless metallic state in this system. The studies of superconductivity in $Cu_xBi_2Se_3$ has proven to be difficult due to imperfections in the growth of the samples and the quality of those produced. [72–74] The half-Heusler compounds YPtBi, LaPtBi, and LuPtBi, have also been investigated as candidates for 3D topological superconductivity. [75–77]

Measurements of dc magnetic susceptibility were made using a Quantum Design Magnetic Property Measurement System (MPMS) SQUID magnetometer on small cleaved pieces for each composition of the crystal boules.

3.1.3.1 Superconducting transition in $Sn_{1-x}In_xTe$

Measurements of the dc magnetic susceptibility ($\chi_{\rm dc} = M/H$) as a function of temperature were used to investigate the onset of superconductivity. $\chi_{\rm dc}(T)$ measurements were carried out in applied fields of 2 mT. Figure 3.4 shows the zero-field-cooled warming (ZFCW) data for all four samples we have studied and the field-cooled cooling (FCC) data for the sample with $x = 0.45$, which is the composition that gave the optimum value for the temperature of the superconducting transition.

The measurements of cleaved pieces of $Sn_{1-x}In_xTe$ show that the superconducting critical temperature T_c increases with increasing x, reaching a maximum at around 4.8 K for and In composition of $x = 0.45$. As can be seen in Figure 3.4, the superconducting transitions displayed are all broad and as a result for comparison the critical temperature is taken as the temperature at which the diamagnetic signal is at 5 % of the full Meissner signal.

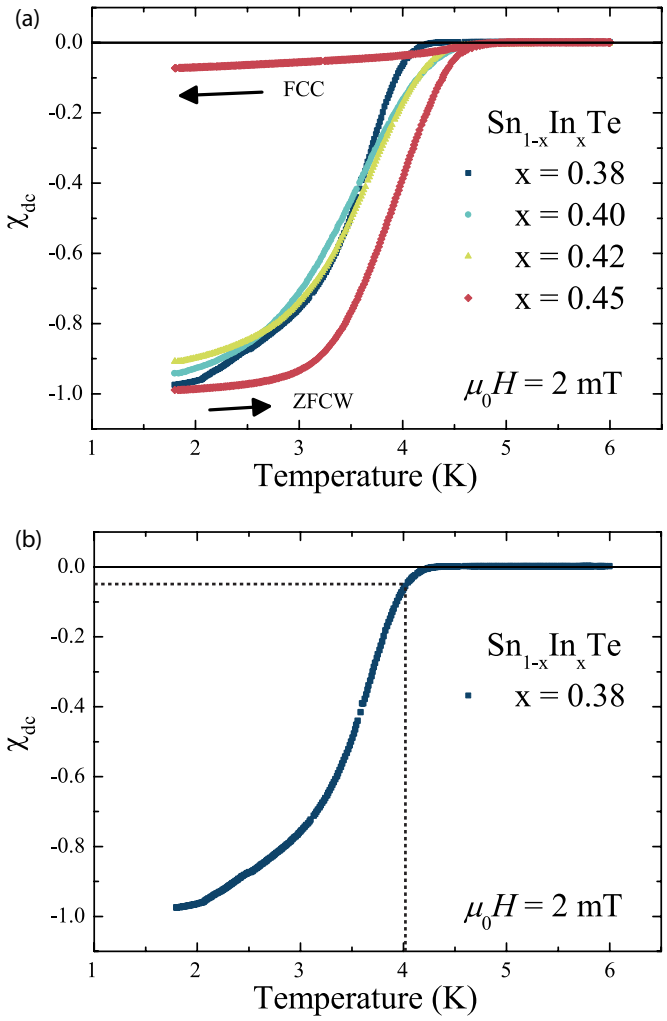

Figure 3.4: (a) Temperature dependence of the dc magnetic susceptibility for four samples of $Sn_{1-x}In_xTe$ with $x = 0.38$, 0.40, 0.42, and 0.45 measured on zero-field-cooled warming (ZFCW) in an applied field of 2 mT. The field-cooled cooling (FCC) curve for the $x = 0.45$ is also shown. The FCC data for the other three samples are similar and are omitted for clarity. (b) The dashed lines demonstrate how the transition temperature is determined. T_c is taken as 5 % of the full Meissner signal.

The relationship between the increasing In composition and that of the increasing transition temperature, T_c, agrees with previous work. [29] For the sample with In composition $x = 0.45$, we observe the onset of the diamagnetic signal at a higher temperature of $T = 5.14(2)$ K. Figure 3.4 shows field-cooled cooling data for the sample grown with varying In compositions. Table 3.3 provides a summary of the temperatures at which the superconducting transitions are observed for $Sn_{1-x}In_xTe$, for $0 \leq x \leq 0.45$.

Table 3.3: Temperatures at which the superconducting transitions are observed for $Sn_{1-x}In_xTe$, for $0 \leq x \leq 0.45$

	$x = 0.38$	$x = 0.40$	$x = 0.42$	$x = 0.45$
T_c K	4.04(5)	4.29(5)	4.33(8)	4.50(5)

3.1.4 Nanomaterial growth of SnTe & Sn_{1-x} In_xTe

The main objective of the work presented in this section is to produce a reliable and repeatable method for growing high quality nanomaterials of TCIs starting from bulk materials that have been shown in literature to exhibit TCI characteristics. We have undertaken the required characterisation of bulk materials allowing us to determine that they are suitable for use as starting materials for the growth of nanomaterials. This section discusses the steps undertaken to develop a growth procedure of TCI nanomaterials that may contain these exotic surface states.

3.1.4.1 Growth method

Two different growth procedures for the nanomaterials were attempted resulting in variable morphologies of SnTe. These included nanowires, crystal stacks and microcrystals, depending on the position and therefore the temperature of the substrate downstream in the tube furnace used

for the growth. For the growth of nanomaterials, a typical temperature profile can be seen in Figure 3.5.

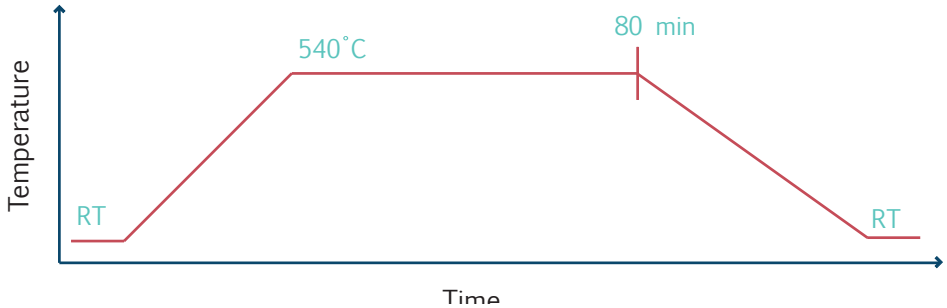

Figure 3.5: A typical temperature profile can be seen for the growth of nanomaterials.

Silicon substrates were prepared using two methods depending on the SnTe morphologies desired. The first was found to be appropriate for the formation of nanowires. This involves using Au nanoparticles as a precursor for nanowire growth. The second method was found to promote the growth of microcrystals and required using a smooth Au layer deposited onto the substrate used. Over 40 experiments were conducted, varying a number of parameters, such as substrate position, source material position, temperatures of the hot and cold zones, Ar gas flow rates used for the growth and duration of growth. The methods reported below explain the processes used to obtain nanomaterials of high yields and the optimum conditions for the growth and crystallinity.

For both methods, a small portion of the SnTe boule (0.05 g) was ground into a fine powder and placed in an alumina-silicate boat to act as the source material for the growth. In most of the studies reported here, the boule with the nominal starting composition 51:49 was used. The silicon substrates used were 50 mm $\times$ 5 mm strips of silicon wafer, cleaved and cleaned using a solvent mixture of 50:50 isopropan-2-ol and acetone. The silicon substrate was blow dried using nitrogen gas.

For the first method, the silicon substrate was dipped into and im-

mediately removed from a sodium citrate solution containing 20 nm gold nanoparticles (Sigma Aldrich). With the substrate placed horizontally, the solution was allowed to evaporate in air at room temperature for approximately 30 minutes. As the substrates dried, evenly spaced gold nanoparticles were observed across the substrate surface using an SEM. The alumina silicate boat containing the SnTe powder was placed in the centre 'hot-zone' of the quartz tube furnace. The prepared silicon substrate was placed downstream in the furnace 'cold-zone'. The quartz tube was evacuated and flushed several times with high purity argon gas (99.997 %) to ensure that there was an inert atmosphere in the chamber prior to growth. A steady flow of argon gas of 35 sccm was then established to act as the carrier gas and to reduce oxidation and contamination during the growth process. The furnace temperature was ramped up rapidly from room temperature (in 10 mins) to reach a target temperature of 540 °C at the hot zone, while the temperature at the cold zone where the substrate was placed was maintained $\approx$ 300 °C. The hot zone of the furnace was maintained at 540 °C for a period of 120 mins, while the growth was allowed to take place and after this period, it was cooled to room temperature. The furnace was calibrated using an external temperature probe that was positioned at various fixed locations along the length of the tube, for a fixed temperature (set point) at the hot zone. From this, a temperature profile over the entire length of the tube inside the furnace was obtained.

For the second procedure, a thermal evaporator was used to deposit a 50 to 100 nm layer of gold onto the silicon substrate to act as a catalyst for growth. The substrate and source material were then placed inside the quartz tube furnace as shown in Figure 2.2 and the same growth conditions were employed as described for the first method. Samples obtained were characterised using SEM, EDAX and EBSD.

For the growth of $Sn_{1-x}In_xTe$ nanomaterials, and with the aim of producing superconducting nanowires, some of the crystal with the opti-

mum critical transtition (In composition $Sn_{0.6}In_{0.4}Te$) was ground into a fine powder and used as source material. The growth methods for SnTe nanowires were utilised for the formation of $Sn_{1-x}In_xTe$ nanowires, the charchterisation of which are described below.

3.1.4.2 Structural characterisation & refinement

After the VLS growth process was completed, a metallic coating on the inside of the quartz furnace tube was formed downstream and the substrate appeared to show metallic crystalline features on the surface when viewed with the naked eye. The substrates were then inspected using SEM. We found that the two different procedures adopted, gave different results. It was found that for the first method, long smooth single crystal nanowires were observed and for the second procedure, where gold was sputtered on the substrate, the structures formed were microcrystals.

We first describe the results obtained on the nanowires. Representative images of the substrate surface for the first procedure are shown in Figure 3.6 along with a high resolution image of an isolated nanowire. Nanowires were observed to grow in random orientations protruding outwards from the sample surface. Typically, the nanowires grown are 200 nm wide and 20 to 50 μm long. EDAX analysis of the nanowire shows that within experimental error the composition is stoichiometrically similar to the source material used. The composition of the nanowires determined using EDAX is presented in Table 4.2. From the high resolution SEM image of a single isolated nanowire in Figure 3.6, it can be seen that the Au-nanoparticle terminates the growth of the nanowire. This suggests a tip growth mechanism occurs with the Au-alloy travelling away from the substrate surface.

This is similar to the recent reports by Li *et al.* [47] for this material. The diameter of the nanowires can also be seen to be constrained to the width of the Au-nanoparticle alloy formed, as all nanowires observed were $\approx$ 200 nm $\times$ 200 nm in cross-section. It was reported in ref. 25 that

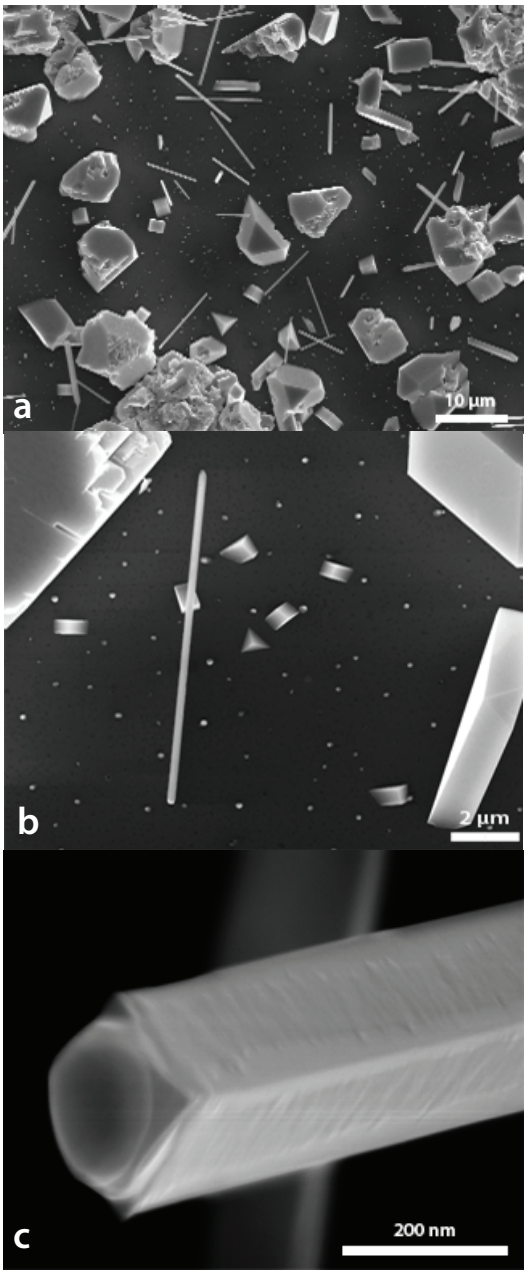

Figure 3.6: (a) SEM image showing a high density of SnTe nanowires amongst microcrystals. (b) SEM image showing a typical nanowire seen protruding from the sample surface surrounded by evenly spaced Au-nanoparticles. (c) High resolution SEM image of the tip of a nanowire showing the smooth nature of the growth. The end of the nanowire can be seen to contain the alloyed Au-nanoparticle which travels along the growth direction.

the nanowires they observed were wider/thicker than the alloy particle, which we see no evidence of. Nanowire formation was best observed in the center of the substrate with microcrystals forming at the warmer end of the substrate (i.e. closer to furnace centre/hot zone).

As a control, a growth was performed without the use of Au-nanoparticles and no nanowires were observed, which suggests the importance of using Au-nanoparticles to catalyse the growth of nanowires. In the growth procedures described by Li *et al.*, the temperature of source material as well as the substrate was much higher than our reported growth temperatures. Their growth periods were also much shorter (30 mins). Our experiments show that when varying both the growth temperature as well as the duration over a very wide range, no evidence of nanowire or microcrystal formation is observed at these high temperatures and for shorter durations.

We find that our optimum growth temperature is 540 $\pm$ 20 °C and duration is $\approx$ 120 mins. For periods longer than 120 mins, we observe a more complete coverage of SnTe. A layer 15 μm thick across the silicon substrate surface is formed and at higher temperatures we observe more nucleation (Figure 3.7). For periods less than 120 mins, very little deposition was seen, as was the case at lower temperatures.

The second experimental procedure described above was conducive to the growth of microcrystals. The morphology of SnTe structures found in this procedure were microcrystal rods and stacks. A typical SEM image obtained is shown in Figure 3.8.

Perfectly formed cubic crystal structures of SnTe can be seen. Using EDAX, these were determined to be stoichiometric in composition to the source material. Microcrystal rods were found to form in clusters on the edges of the substrate, protruding out of the surface. They also formed as single stacks on the surface as flat planes parallel to the substrate surface. Using EBSD, it was found that all the structures grew predominantly in the vicinal $\{001\}$ growth orientation as can be seen in Figure 3.8.

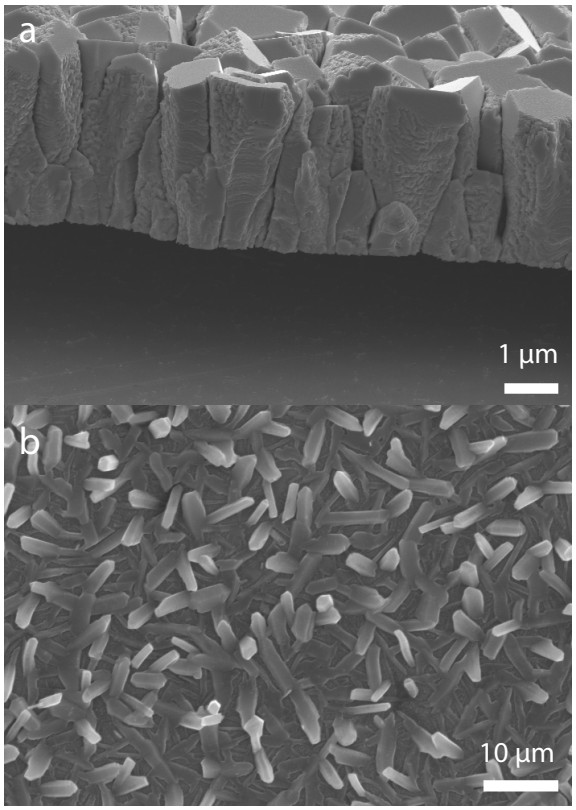

Figure 3.7: (a) Representative SEM image of the growth of SnTe for periods longer than 120 minutes. The thickness of the SnTe film grown is $\approx$ 15 μm (b) Representative SEM image of the growth of SnTe for temperatures greater than the optimum temperature of 540 °C. Much greater nucleation is observed coupled with a greater growth rate giving rise to thicker structures resembling nanowires.

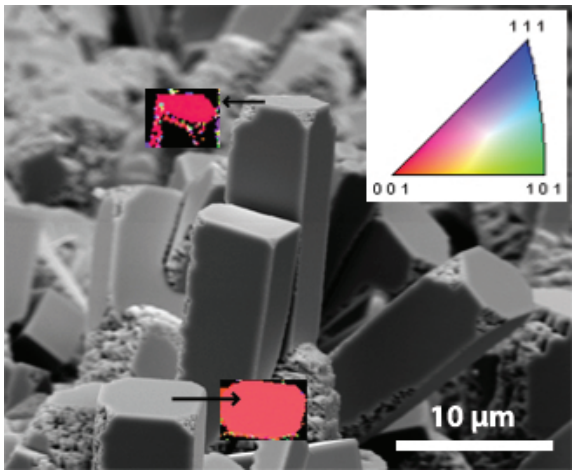

Figure 3.8: SEM image of SnTe microcrystals. The two red insets placed next to the corresponding microstructures show the EBSD pattern of the growth orientation in the direction normal to the growth axis. This is typically found to be a vincinal $\{001\}$ orientation for the majority of crystals but some show a $\{111\}$ growth plane.

This was also observed by Li *et al.* where the growth direction of their crystals is along the $<001>$ zone axis. It was also found that the Au-layer, sputtered onto the substrate surface, played an important role in promoting growth as no ordered SnTe structures were observed when the same growth procedure was carried out without the Au layer.

After establishing a growth procedure for the parent compound SnTe, the same optimum conditions were used for the production of nanowires for the growth of $Sn_{1-x}In_xTe$ nanomaterials. Under these same parameters, nanowires of $Sn_{1-x}In_xTe$ were produced which were thicker than those observed for SnTe nanowires ($\approx$ 400 nm). Figure 3.9 shows a SEM image of a $Sn_{1-x}In_xTe$ nanowire.

The structure of the nanowires appeared tetragonal with a pyramidal formation near the tip of the wire. Numerous step edges and dislocations were observed along the length of the nanowires. Upon EDX compositional analysis of these wires, they were found to be In-deficient and no consistency was observed with regards to composition from one wire to

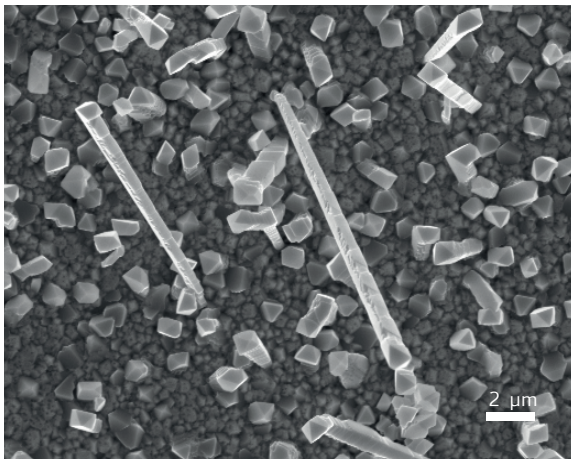

Figure 3.9: Representative SEM image of $Sn_{1-x}In_xTe$ nanowires. The nanowires can be seen protruding normal to the surface surrounded by a darker grey region where nucleation has occurred but nanowires have failed to develop.

the next. Due to the low vapour pressure of In, and the long growth period required to grow the nanowires, it would seem that there is an overpressure of In at the start of the growth due to the lower melting point of In and that a uniform congruent gas flow does not occur.

A refinement of the growth methods and parameters could yield nanowires with a higher In content to match that of the most optimum composition for superconductivity and these refinements are ongoing.

3.2 Surface Preparation of Microcrystals of the TCI, SnTe

Investigating materials thought to exhibit topological surface properties can present a challenge as clean surfaces are a pre-requisite for band structure measurements when using nano-ARPES or laser-ARPES in ultra-high vacuum. This issue is exacerbated when dealing with nano or micron sized materials which have been prepared ex-situ and so have

been exposed to atmosphere. This chapter presents the findings of an XPS study where various cleaning methods have been employed to reduce the surface contamination and preserve the surface quality and topological characteristics for surface sensitive measurements.

3.2.1 Cleaning treatments

Microcrystals of the topological crystalline insulator SnTe were grown ex-situ and transferred into UHV before being treated with either atomic hydrogen, argon sputtering, annealing or a combination of treatments.

3.2.2 X-ray photoelectron spectroscopy

A common practise to probe the band structure of TIs and TCIs (such as HgTe, Bi_2Se_3, Bi_2Te_3 and SnTe) is to perform surface sensitive angle-resolved photoemission spectroscopy (ARPES) measurements. [20, 78, 79] Samples are usually bulk crystals that have been cleaved inside the vacuum or thin films grown in-situ.

It is thought to be difficult to detect the weak signal arising from the exotic surface properties of TIs and TCIs. To combat this, there has been a focus to increase the surface area to volume ratio (SAVR) of such materials in the hope that the exotic surface properties become more readily available. [31] There have been numerous successful examples for the conversion of TIs and TCIs from bulk to nanoform using a variety of growth techniques, including both wet and dry synthesis methods. [31–43, 47, 48] Furthermore, the majority of the growth techniques used to make nanomaterials are not designed to keep the samples free from contamination and naturally occurring atmospheric oxidation.

We will demonstrate effective cleaning methods in ultra high vacuum (UHV) of high SAVR materials which have been exposed to atmosphere. With this information, we provide a preparation method that can be used to negate the effects of surface contamination and allow the exotic surface

states of TCIs to be explored.

3.2.3 Experimental methods

The x-ray photoemission spectroscopy (XPS) data were collected at the University of Warwick Photoemission Facility, more details of which are available at reference [80]. The samples investigated in this study were mounted on Omicron sample plates using tantalum foil and loaded in to the fast-entry chamber. Once a pressure of less than 1 x 10^{-7} mbar had been achieved (approx. 1 hour), the samples were transferred to a 12-stage storage carousel, located between the preparation and main analysis chambers, for storage at pressures of less than 2 x 10^{-10} mbar.

XPS measurements were conducted in the main analysis chamber (base pressure 2 x 10^{-11} mbar), with the sample being illuminated using an XM1000 monochromatic Al Kα_1 x-ray source (Omicron Nanotechnology). The measurements were conducted at room temperature and at a take-off angle of 90°. The photoelectrons were detected using a Sphera electron analyser (Omicron Nanotechnology), with the core levels recorded using a pass energy of 10 eV (resolution approx. 0.47 eV). The data were analysed using the CasaXPS package, using Shirley backgrounds, mixed Gaussian-Lorentzian (Voigt) lineshapes and asymmetry parameters where appropriate. All binding energies were calibrated using the Fermi edge of a polycrystalline Ag sample, measured immediately prior to commencing the measurements.

In-situ sample preparation was conducted with a variety of instruments attached to the vacuum system. Ion bombardment was conducted in the analysis chamber at room temperature using an incident beam of 500 eV Ar^+ ions, generated using a FIG 05 ion gun (Omicron Nanotechnology, UK). Atomic hydrogen exposure was facilitated by a TC-50 thermal gas cracker (Oxford Applied Research, UK) in the preparation chamber, with an estimated H_2 cracking efficiency of 50 %. All atomic hydrogen doses

were conducted over a 15 minute duration using a pressure of 1x10^{-6} mbar (675 L total per dose [H and H_2 combined]), with the sample held at the chosen temperature for the duration of H dosing and for a subsequent five minutes in the absence of a H flow. Sample annealing was achieved using sample heaters located on the manipulators in both the preparation and analysis chambers, with the sample temperature measured using a pre-calibrated chromel-alumel thermocouple.

3.2.4 Results and discussion

In total, four different treatment methods were investigated. These included argon sputtering at room temperature, atomic hydrogen cleaning at room temperature, atomic hydrogen cleaning at elevated temperatures and just annealing in UHV. SEM was used to compare the effects of the more effective cleaning methods to the surface morphology. EDX measurements were performed in order to compare the surface and bulk stoichiometries via a comparison with XPS results. XPS also provided an insight in the oxides formed at the surface during exposure to atmosphere.

Figures 3.10, 3.11 and 3.12 show the effectiveness of removing the oxide layer and the adventitious carbon formed at the surface for different cleaning methods. They also show the changes to the Sn $3d_{5/2}$ and Te $3d_{5/2}$ peaks to various treatment methods. The Sn $3d_{5/2}$ peak was fit with two components for Sn^{2+} and Sn^{4+} with the positions at a binding energy (B.E.) of 485.4 $\pm$ 0.1 eV and 487.1 $\pm$ 0.1 eV respectively. The value for the B.E. of SnO_2 is consistent with that found in reference tables and literature. [81] The full width half maximum and the energy difference of the two components were constrained during fitting. Five components were used to fit the Te $3d_{5/2}$ peak, three of which were attributed to the two possible oxidation methods and intermediate oxide phases for the formation of TeO^{+4}. The B.E. for Te^{-2} and TeO^{+4} was 572.3 $\pm$ 0.1 eV and 576.8 $\pm$ 0.1 eV. A summary of the B.E. can be found in Table 3.4.

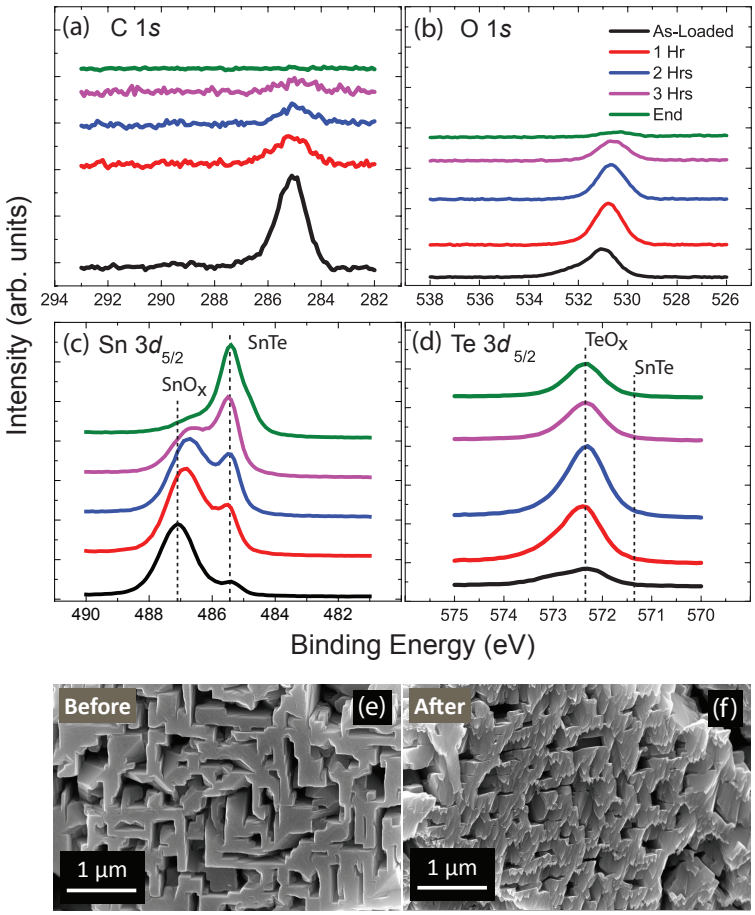

Figure 3.10: XPS data for the (a) C_{1s},(b) O_{1s},(c) Sn $3d_{5/2}$ and (d) Te $3d_{5/2}$ peaks. Samples were subject to an argon sputtering cycle and the data presented shows chemical shifts for an as-loaded sample (black), the effects after 1 hour (red), 2 hours (blue), 3 hours (purple) and the end of the treatment cycle (green). SEM images (e + f) show how the treatment effects the sample surface. Damage to the surface can clearly be seen in the form of 'shadow cones' formed, the direction of which are dependent on the sputtering angle.

Table 3.4: The B.E. for the fitted components of Sn $3d_{5/2}$ and Te $3d_{5/2}$ peaks.

Component	B.E. (eV)
Sn^{2+}	485.4 ($\pm$ 0.1)
Sn^{4+}	487.1 ($\pm$ 0.1)
Te^{-2}	572.3 ($\pm$ 0.1)
Te^{+4}	576.8 ($\pm$ 0.1)

Figures 3.10 and 3.11 show that at room temperature, both argon sputtering and atomic hydrogen cleaning were similar in effectiveness. Whilst both reduced the intensity of the C 1s present at the surface, there was still a noticeable peak showing the presence of oxygen with argon sputtering. Figure 3.10 also shows that the Sn and Te peaks are still quite broad, owing to the presence of SnO_x and TeO_x at the surface, compared to that observed in Figure 3.11, for atomic hydrogen cleaning at room temperature. SEM revealed that the surface morphology had changed with the introduction of 'shadow cones' to the surface after bombardment. Such features can be seen in Figure 3.10f. EDX did not show a change in the bulk stoichiometry after room temperature treatments of argon sputtering or atomic hydrogen treatment. The stoichiometry at the surface determined from XPS also remained the same post treatment for both argon sputtering and atomic hydrogen cleaning and further more appears to be Sn-rich, suggesting the majority of the surface oxide is SnO_x (see Table 3.5).

In order for the cleaning to yield a smooth surface as seen in Figure 3.10e, an anneal cycle was introduced after both argon sputtering and atomic hydrogen cleaning. Annealing at temperatures of upto 600 $^{\circ}$C were investigated along with dose lengths upto 24 hours. XPS revealed that at temperatures higher than 300 $^{\circ}$C, large amounts of Te were evaporated from the sample, thereby destroying the stoichiometry

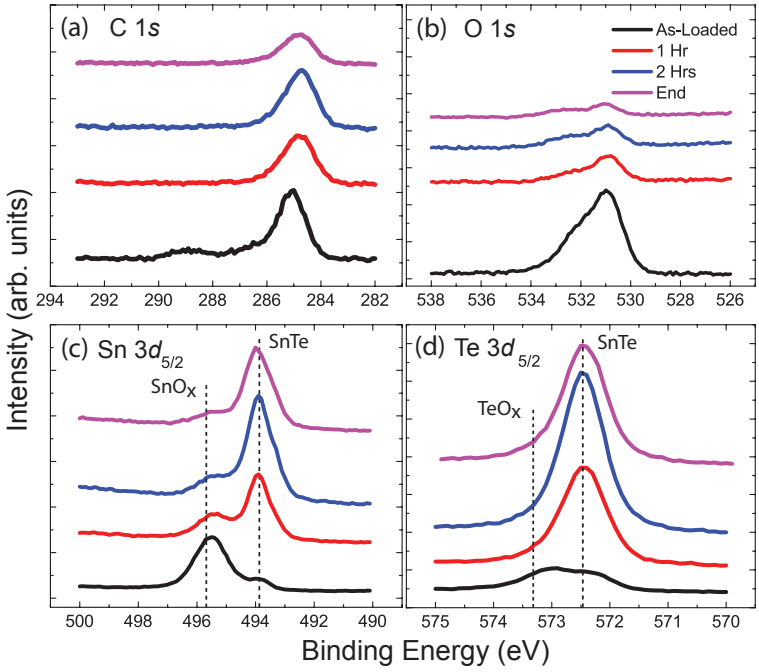

Figure 3.11: XPS data for the (a) C_{1s},(b) O_{1s},(c) Sn $3d_{5/2}$ and (d) Te $3d_{5/2}$ peaks. Samples were subject to an atomic hydrogen cleaning cycle at room temperature and the data presented shows the chemical shifts for an as-loaded sample (black), the effects after 1 hour (red), 2 hours (blue) and the end of the treatment cycle (purple).

Table 3.5: Representative atomic compositions for the bulk and the surface of SnTe microcrystals obtained using EDX and XPS analysis.

Treatment	EDX	XPS
Argon Sputtering	$Sn_{49(2)}Te_{51(2)}$	$Sn_{60(2)}Te_{39(0)}$
AHC	$Sn_{48(2)}Te_{52(2)}$	$Sn_{64(2)}Te_{35(2)}$
AHC + 200	$Sn_{49(2)}Te_{51(2)}$	$Sn_{54(2)}Te_{45(2)}$

of the surface. However, we found that annealing at 200 °C preserved the surface stoichiometry of the sample confirmed by both EDX and XPS measurements. The 'shadow cones' present due to sputtering were not however removed after either anneal cycle.

Figure 3.12 shows the XPS data for samples exposed to atomic hydrogen at 200 °C. This method was found to be most effective for four reasons. Firstly, heating the sample to 200 °C allowed for the removal of the surface oxides and and carbon peaks to a greater extent to that observed for argon sputtering and atomic hydrogen cleaning at room temperature. Secondly, the time required to clean the surface of the sample reduced vastly compared to ion bombardment and annealing, with the residual surface oxides and carbon components reaching near background levels after $\approx$ 1 hour. Thirdly, the morphology of the sample surface remained the same after treatment as can be seen in Figure 3.12f. Finally, compositional analysis of the bulk of the microcrystals with EDX analysis post-treatment showed no change to the stoichiometry. Similar results were observed for the surface stoichiometry from XPS and can be found in Table 3.5.

With regards to dose lengths, it is clear that atomic hydrogen cleaning at 200 °C offers the most promising route to a surface which would be sufficiently clean to conduct surface sensitive measurements such as ARPES. It is worth noting that due to the geometry of the sample and sputter gun, it was not possible to remove the oxide and carbon from

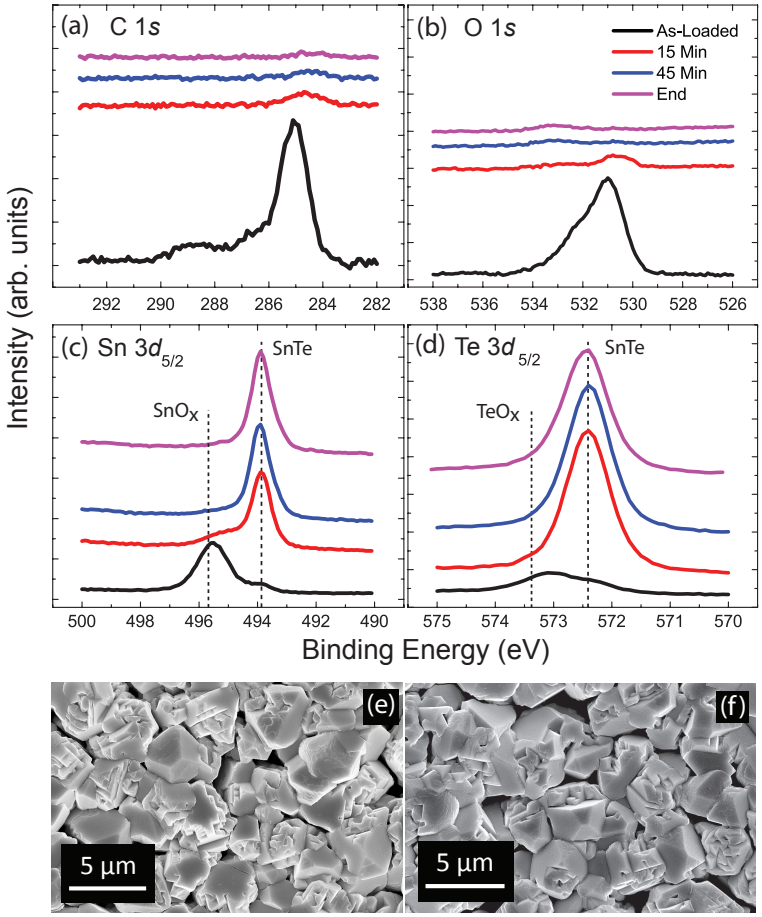

Figure 3.12: XPS data for the (a) C_{1s},(b) O_{1s},(c) Sn $3d_{5/2}$ and (d) Te $3d_{5/2}$ peaks. Samples were subject to an atomic hydrogen cleaning cycle at room temperature and the data presented shows the chemical shifts for an as-loaded sample (black), the effects after 1 hour (red), 2 hours (blue) and the end of the treatment cycle (purple). (e + f) SEM images of microcrsytals pre and post treatment showing no change to the surface morphology.

the edges of the microcrystals, however, the surface normal to the substrate had been successfully cleaned and restored without a stoichiometric change in the bulk or surface of the sample. This limitation was overcome for atomic hydrogen cleaning as the gas cracker was aligned to the surface normal.

3.3 Summary and conclusions

In summary, we show a reliable growth method to obtain high quality crystals of SnTe and $Sn_{1-x}In_xTe$ for a variety of In substitutions, one of which is the optimum composition, $x = 0.45$, where we observe the highest value of the superconducting transition temperature ($T_c = 4.8$ K).

We have also determined the optimum growth conditions for the formation of nanowires and microcrystals of SnTe. Both these structures were produced using the VLS growth method. We have determined the growth orientation of SnTe microcrystals using EBSD and found this to be vicinal $\{001\}$ to the direction normal. We find that a Au precursor is essential for the growth of both the nanowires as well as the microcrystals. The growth results are dependent on the temperature of the source material, the substrate temperature which corresponds to the position of the substrate in the cold zone and the growth duration. This demonstration for the growth of topological insulators and their derivatives in micro or nanoform allows a pathway to be established to potentially exploit and enhance the observable topological surface state features by reducing the bulk contribution.

To refine to growth procedure leading to the production of $Sn_{1-x}In_xTe$ nanowires with the optimum In composition, would mean to increase the In composition of the starting material or to significantly modify the experimental setup to produce a different growth environment. This is an avenue that is still being pursued in the hope of producing a topological crystalline insulator with superconducting properties.

In this study, the most effective method to prepare the surface of microcrystals for the TCI, SnTe has been investigated. It was found that cleaning with atomic hydrogen for a minimum of 15 minutes at 200 °C removed a sufficient amount of surface oxide and carbon to perform measurements such as ARPES. We also found by performing SEM on samples pre and post treatment, that damage did not occur to the surface of the material with atomic hydrogen cleaning, which is not the case for argon sputtering due to the formation of 'shadow cones'. This optimal cleaning procedure was also able to restore the bulk stoichiometry at the sample surface, as evidenced in the comparison of EDX and XPS measurements.

Sputtering the sample surface with argon was also investigated, however, it was not found to be as effective as atomic hydrogen in removing surface contamination, and also caused significant damage to the microcrystal surface. Removing surface impurities with annealing cycles in UHV was ineffective. Table 3.5 provides a summary of the atomic composition for each treatment. The data presented describes an effective pathway to obtaining clean surfaces for materials with exotic topologically protected surface states and for surface sensitive measurements of these systems.

Chapter 4

$Pb_{1-x}Sn_xTe$ and $Pb_{1-x}Sn_xSe$

4.1 Introduction

This chapter looks at two compounds closely related to the parent TCI, SnTe, which was discussed in the previous chapter. The growth methods used to obtain bulk crystals of these materials along with the procedure to convert them into nanomaterials will be discussed.

We have chosen to study the formation of nanomaterials starting with bulk crystals of $Pb_{1-x}Sn_xTe$, for an optimum Sn substitution level of $x = 0.4$ and $Pb_{1-x}Sn_xSe$ with three different Sn substitution levels $x = 0.18, 0.23$ and 0.30. We report the growth of high quality single crystal nanowires of $Pb_{1-x}Sn_xTe$ ($x = 0.23(2)$), close to the critical Sn content at which the TCI transition occurs in this material. We also report attempts to produce nanomaterials of $Pb_{1-x}Sn_xSe$. In both cases, a Au-catalysed VLS growth technique was used, similar to that adopted for SnTe [82]. The optimum growth conditions and parameters obtained from the study are presented. The methods described herein provide a route to producing suitable nanomaterials which may lead to the successful investigation of the enhanced TCI states of the compounds $Pb_{1-x}Sn_xTe/Se$. Detailed characterisation performed on the bulk crystals grown, as precursors to the

Table 4.1: Compositions of the bulk $Pb_{0.60}Sn_{0.40}Te$ and $Pb_{1-x}Sn_xSe$ crystal boules synthesized.

Nominal starting composition
$Pb_{0.60}Sn_{0.40}Te$
$Pb_{0.82}Sn_{0.18}Se$
$Pb_{0.77}Sn_{0.23}Se$
$Pb_{0.70}Sn_{0.30}Se$

nanomaterial growth, include powder x-ray diffraction (XRD), x-ray Laue diffraction, scanning electron microscopy (SEM) and energy dispersive x-ray analysis (EDX). The resultant nano and micro materials obtained are characterised using SEM, EDX, transmission electron microscopy (TEM) and selective area electron diffraction (SAED).

4.2 Crystal growth & characterisation

In order to determine the maximum temperature at which to perform the crystal growth, one must find the fusion temperatures of the two parent compounds for each ternary. For example, PbTe and SnTe has a fusion temperature of 924 $^{\circ}\mathrm{C}$ and 806 $^{\circ}\mathrm{C}$ respectively. PbSe and SnSe have fusion temperatures of 1078 $^{\circ}\mathrm{C}$ and 861 $^{\circ}\mathrm{C}$ respectively. A lower growth temperature similar to the melting point of SnSe, SnTe and PbTe would translate to low diffusion rates. A higher temperature allows for good diffusive mixing of the elements within the experimental time frame. A growth temperature of $\approx$ 1075 $^{\circ}\mathrm{C}$ was therfore chosen. A summary of all the materials synthesized including the composition, x, of those materials can be seen in Table 4.1.

Starting with high purity Pb and Sn shot (Alpha Aesar 99.99 $\%$) and powders of Sn and Se, (Alpha Aesar 99.99 $\%$), the stoichiometric

mixtures were carefully placed in quartz tubes. The tubes were evacuated and sealed under vacuum. Following the procedure described by Tanaka *et al.*, a modified Bridgman was employed. The quartz tubes were placed vertically into a furnace and the temperature was ramped to $\approx$ 1075 $^{\circ}\mathrm{C}$ and remained at this temperature for a period of 48 hours. [10] The furnace was then slow cooled at 2 $^{\circ}\mathrm{C}$/h to 700 $^{\circ}\mathrm{C}$. The tubes were rapidly cooled from this temperature to room temperature at a rate of 200 $^{\circ}\mathrm{C}$/h.

The crystal boules obtained had shiny metallic surfaces when examined visually (Figure 4.1). The phase purity of the crystals was determined by performing powder XRD. Small pieces of the crystal boules were finely powdered and placed in a Panalytical X'Pert Pro system with a monochromatic Cu Kα1 radiation source.

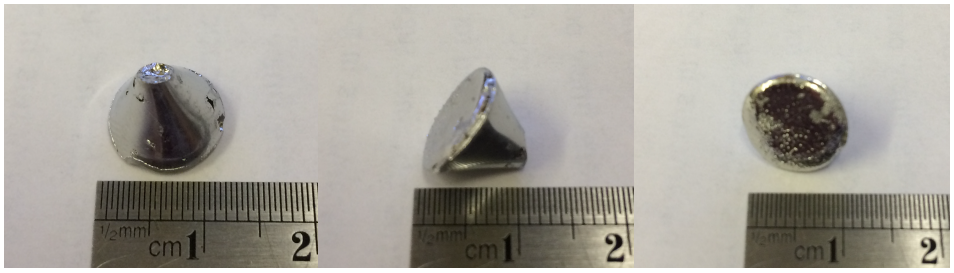

Figure 4.1: A typical crystal boule obtained after the modified Bridgman growth process. View from various elevations. (Composition: $Pb_{0.60}Sn_{0.40}Te$)

4.2.1 X-ray diffraction & compositional analysis

.

Figure 4.2 shows the X-ray powder diffraction data obtained for two samples, $Pb_{0.60}Sn_{0.40}Te$ and $Pb_{0.70}Sn_{0.30}Se$. The x-ray patterns obtained suggests that the crystals grown are mostly single phase with lattice parameters in good agreement with the expected values (see Table 4.2). The solubility limit for rock-salt $Pb_{1-x}Sn_xSe$ is about 40 $\%$ and the average stoichiometry was found to be $\approx x = 0.3$, as detected by EDX

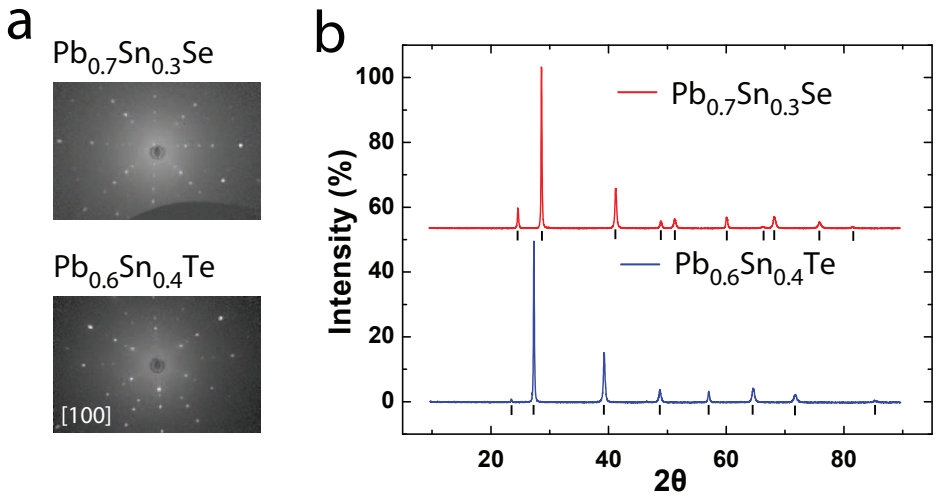

Figure 4.2: (a) X-ray Laue diffraction data taken of two of the crystals grown along the [100] direction. This is a typical representation of all the crystal boules synthesized. The sharp spots demonstrate the high crystallinity of samples. (b) Powder XRD spectra taken on crushed powders from the as grown boules of $Pb_{0.70}Sn_{0.30}Se$ and $Pb_{0.60}Sn_{0.40}Te$ demonstrating the single phase nature of the crystal boules. The tick marks show the positions of the expected Bragg peaks.

Table 4.2: Representative atomic compositions of the bulk $Pb_{0.60}Sn_{0.40}Te$ and $Pb_{1-x}Sn_xSe$ crystal boules are shown below. The data was obtained using EDX analysis of the bulk crystals. Lattice parameters for the powdered sections of the crystal boules obtained using powder XRD are also presented. The lattice parameters obtained show a slight discrepancy when compared to previously published data. [10] This discrepancy may be possible due to the strain in the samples. Further studies are required to investigate this.

Nominal starting composition	Atomic Percent (%) Pb	Sn	Te/Se	Total	Lattice parameter, *a* (Å)
$Pb_{0.60}Sn_{0.40}Te$	29(2)	21(2)	50(2)	100	6.420(0.020)
$Pb_{0.82}Sn_{0.18}Se$	41(2)	9(2)	50(2)	100	6.147(0.004)
$Pb_{0.77}Sn_{0.23}Se$	40(2)	11(2)	48(2)	100	6.147(0.005)
$Pb_{0.07}Sn_{0.30}Se$	34(2)	16(2)	49(2)	100	6.146(0.008)

analysis.

The crystallinity of the boules produced were examined using X-Ray Laue diffraction. This was performed across the surface of the crystal boules at various points. The diffraction patterns observed revealed sharp spots as can be seen in Figure 4.2a. This demonstrates the high crystalline nature of the samples grown and provides the orientation of the crystals cleaved from the as-grown boules.

Compositional analysis was performed on different sections of the crystal boules. Cleaved sections of the boules were examined using an EDX system on a Zeiss SUPRA 55-VP scanning electron microscope. The results showed that all the crystals grown were of a stoichiometry similar to the nominal starting compositions, within error, as shown in Table 4.2. The crystals were powdered for use as starting materials for the growth of nanomaterials.

4.3 Nanomaterials of $Pb_{1-x}Sn_xTe$ and $Pb_{1-x}Sn_xSe$

Various parameters were refined and optimised to find the best conditions to obtain high quality nanowires with a good yield. This involved performing over 20 experiments adjusting the temperature of the hot zone as well as substrate position and argon flow rate similar to methods adopted in our previous work on the TCI, SnTe, and as described in the previous chapter 3 Section 3.1.4. [82] Growth preparation techniques common to both materials will be discussed first followed by results specific to $Pb_{1-x}Sn_xTe$ and $Pb_{1-x}Sn_xSe$ respectively.

4.3.1 Nanomaterial growth

The preparation of the silicon substrates used for nanomaterial growth involved a two step process. First the silicon wafer substrates (approx. 5 mm x 30 mm) were cleaned using a 50:50 mixture of acetone and isopropan-2-ol. These were then allowed to dry naturally in air before suspending a sodium citrate gold nanoparticle buffer solution on the surface of the substrates (Alpha Aesar 20 nm gold nanoparticles). The buffer was held in position by the surface tension of the solution on the substrates. The solution was then allowed to evaporate in ambient room temperature conditions. We found that the Au nanoparticles dispersed on the surface with a density of $\approx 5/\mu m^2$.

5 mg of the source material was then placed at the centre of an alumina-silicate boat which in turn was placed in the centre of the 'hot zone' of a 20 cm tube furnace. The silicon substrates were placed down stream in a 'cold zone'. For the growth of $Pb_{0.80}Sn_{0.20}Te$ nanowires, the furnace was rapidly heated to 540 $^{\circ}C$ in 25 minutes under a flow of argon, to suppress oxide growth and to act as a carrier gas for the source material. The furnace remained at this temperature for a further 120 minutes at

which point it was allowed to cool to room temperature naturally. The temperature of the 'cold zone' where substrates were placed for micro and nanomaterial growth was $\approx 300\ ^{\circ}\mathrm{C}$. A table showing detailed growth parameters that have been used for the growth are shown in Table 4.3

It should also be noted that the system was restored to a clean state after each growth cycle. This was to prevent the deposition on the inside of the quartz tubes which was the preferential location for growth due to prior deposition of the source material in previous growth cycles. To clean the quartz tube, it was placed vertically in aqua regia for at least 1 hour and then thoroughly rinsed with water and allowed to dry naturally. To refine the growth parameters, over 50 experiments were performed and 6 parameters were varied to obtain the desired growth morphologies.

4.3.2 Structural characterisation and compositional analysis

After performing the nanomaterial growth, the substrates were removed from the furnace and upon visual inspection, metallic grey features on the surface of the substrates could be seen. The inside of the quartz tube was found to be coated with a thin metallic layer at the 'cold zone'. Table 4.3 shows a summary of the results obtained for the various starting materials. For the growths performed with $Pb_{1-x}Sn_xTe$, nanomaterials in the form of wires were obtained. The growth of microcrystals surrounding the free standing nanowires was also observed for $Pb_{1-x}Sn_xTe$. For the growths with $Pb_{1-x}Sn_xSe$, however, microcrystals in the form of cubes were predominantly observed with a few nanowires present - see Table 4.3.

$Pb_{1-x}Sn_xTe$

TEM was used to obtain information on the quality of the $Pb_{1-x}Sn_xTe$ nanowires grown which had a composition of $Pb_{0.77(2)}Sn_{0.23(2)}Te$ when

Table 4.3: Representative growth conditions and outcomes for the nanowire growth attempts. Rows 1 - 5 show some of the refinement steps in the growth procedure to obtain nanowires (row 6). Rows 7 - 10 show the refinement of the growth paramerters for $Pb_{1-x}Sn_xSe$ nanomaterials.

No.	Source Material	Mass (g)	Substrate Information	Ar flow rate (sccm)	Source temp. (°C)	Substrate temp. (°C)	Growth Duration (min)	Nanostructures observed
1	$Pb_{0.60}Sn_{0.40}Te$	0.05	Si/Sprayed Au nanoparticles	35	540	400	90	No nanowires, layered growth
2	$Pb_{0.60}Sn_{0.40}Te$	0.05	Si/Sprayed Au nanoparticles	35	540	350	90	No nanowires
3	$Pb_{0.60}Sn_{0.40}Te$	0.05	Si/Sprayed Au nanoparticles	35	540	350	120	Some microcrystals & layered growth
4	$Pb_{0.60}Sn_{0.40}Te$	0.05	Si/Dipped Au nanoparticles	35	540	400	120	Some small microcrystals observed ($\leq 1\mu m$)
5	$Pb_{0.60}Sn_{0.40}Te$	0.05	Si/Sputtered Au + Sprayed Au nanoparticles	35	540	400	120	Some nanowires & thicker layered crystals
6	$Pb_{0.60}Sn_{0.40}Te$	0.05	Si/Suspended Au nanoparticles	35	540	400	120	Isolated nanowires observed
7	$Pb_{0.82}Sn_{0.18}Se$	0.05	Si/Suspended Au nanoparticles	35	540	400	120	Layer of PbSe, trace amounts of Sn
8	$Pb_{0.77}Sn_{0.23}Se$	0.05	Si/Suspended Au nanoparticles	35	530	400	120	Layer of PbSe, trace amounts of Sn
9	$Pb_{0.70}Sn_{0.30}Se$	0.1	Si/Suspended Au nanoparticles	35	530	400	140	Layer of PbSe, trace amounts of Sn
10	$Pb_{0.70}Sn_{0.30}Se$	0.05	Si/Suspended Au nanoparticles	35	550	400	120	Decomposition of SnSe zig-zag and PbSe microcubes

Table 4.4: Chemical composition of the materials observed using EDX analysis.

Starting material (Powder)	Nanowire Composition	Microcrystal Composition
$Pb_{0.60}Sn_{0.40}Te$	$Pb_{0.77(2)}Sn_{0.23(2)}Te$	$Pb_{0.60(2)}Sn_{0.40(2)}Te$

examined by EDX as shown in Table 4.4. The nanowires were found to be between 10 and 50 μm long with a typical thickness of $\approx$ 100 nm. The growth density of the nanowires, observed from SEM, was found to be $\approx 0.40/\mu m^2$. Figure 4.3 shows an SEM image of the results for a typical growth with both nanowires and microcrystals of $Pb_{1-x}Sn_xTe$ obtained. The optimum conditions to produce nanowires can be found in Table 4.3, row 6.

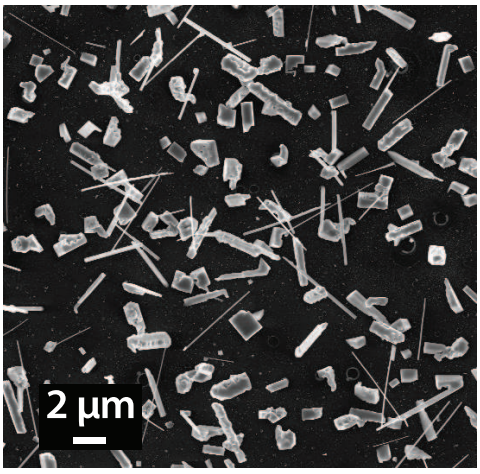

Figure 4.3: Representative SEM image of the growth of $Pb_{1-x}Sn_xTe$ nanowires and microcrystals. The thickness of the nanowires are $\approx$ 100 nm and lengths of up to 15 μm are observed. The microcrystals are distributed randomly but have distinct cubic growth facets.

It has been widely reported that dispersed gold nanoparticles on the surface of the silicon substrates act as catalysts and promote the growth of nanowires. [83] The growth is through the formation of an alloy at the

tip of the nanowire. The TEM image (Figure 4.4a) shows a nanowire with a gold alloy which has formed at the tip, commonly seen in shorter ($<$ 4 μm) thinner nanowires ($<$ 80 nm). By observing various stages of the growth from nucleation, we observe that the alloy travels upwards in the growth direction of the nanowires. This is the typical tip-growth mechanism by which these nanowires grow.

Using TEM and SAED, the growth orientation of the crystalline nanowires was determined. Figure 4.4b shows an atomic resolution image of a $Pb_{0.77(2)}Sn_{0.23(2)}Te$ nanowire from which the lattice parameter was obtained (6.497(3) Å). Using a focused ion beam (FIB) to prepare a nanowire in cross-section, SAED was performed to obtain structural information about the growth orientation of the nanowires (Figure 4.4c). The nanowires were found to grow in the [100] direction. Sharp diffraction spots are also indicative of the highly crystalline nature of the nanowires.

We also determined from TEM that some thicker nanowires ($>$ 80 nm) grew with a core-shell structure as commonly observed in GaAs and ZnO nanowires (Figure 4.4d). [83, 84] When performing cross-sectional TEM on samples prepared using FIB milling, EDX does not show a variation in composition of the core-shell to that of the surface. We believe therefore that a transition in the growth process occurs, namely, from a VLS to VS growth process similar to that observed for AlGaAs nanowires. [85] The axial growth of the central core is thought to be a VLS process after which a radial VS growth process dominates. The central core has a thickness comparable to the gold alloys at the tip of the nanowires which is approximately 30 nm.

Within the nanowires, we also observe contrast that agrees with Guinier-Preston like zones (G-P zones) under TEM (Figure 4.4e). This metallurgical process can occur at room temperature and is typically observed in age hardened aluminium alloys. [84] G-P zones are also visible due to rapid cooling where precipitation occurs because the supersaturation within the crystal lattice. The natural diffusion of atoms within a lattice can form

localised concentrations that can then act as nucleation sites for other intermediate phases. These features introduce strain in the lattice. We find no structural defects such as dislocations or stacking faults within the regions and the G-P like zones appear at right angles to each other in line with the crystal lattice. EDX was unable to detect any compositional difference of the G-P zones to the surrounding matrix. A compositional difference is something that would be expected for G-P zones, however, the zones are surrounded by a thick matrix and therefore a compositional difference cannot be detected. As a result, the origin of these zones remains to be ascertained.

For very long ($>$ 4 μm) and thick nanowires ($>$ 80 nm) as seen in Figure 4.4f, no gold alloy was found at the tip of the nanowire. From EDX, small trace amounts of gold could be detected which may suggest that the gold nanoparticle eventually becomes consumed within the body of the longer nanowire. In shorter nanowires ($<$ 4 μm), we observe a distinct gold alloy formation at the tip of the nanowire (4.4a). This further demonstrates the change in the growth mechanism of the nanowires - namely from an initial VLS process to form shorter thinner nanowires, to a VS process that leads to longer and thicker wires.

EDX obtained in TEM mode reveals that the nanowires have a chemical composition, within experimental error, that lies in the region of the critical transition point in $Pb_{1-x}Sn_xTe$ nanowires ($\sim x = 0.25$) [53], the point at which the material changes from a trivial insulator to a TCI (see Table 4.5). To compare the nanowires with the bulk crystals grown, TEM was used to obtain the lattice parameter from the edge of the nanowire. The lattice parameter matches (within experimental error) that of the starting powder obtained from crushed crystals shown in Table 4.2.

In addition to the nanowires, micron sized crystals were also observed in areas surrounding the nanowires. EBSD allows us to ascertain the orientation of the faces of the microcrystals grown. EDX compositional analysis of these microcrystals revealed a stoichiometry similar to that of

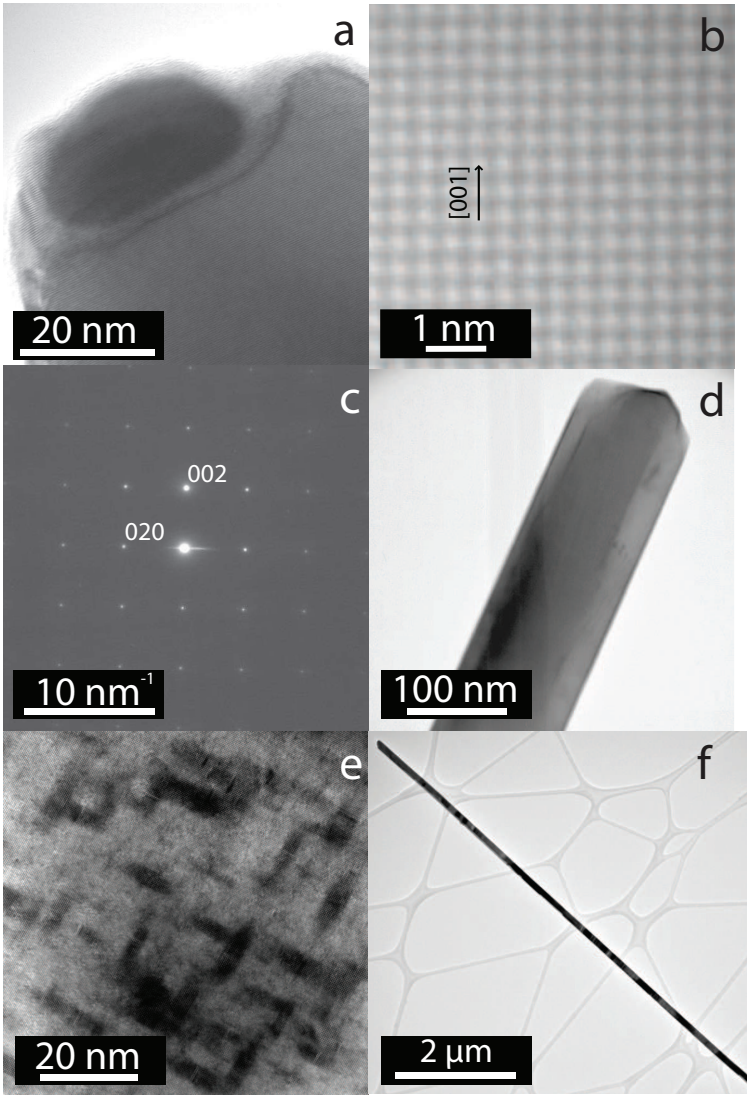

Figure 4.4: (a) HR-TEM of the gold alloy formed at the tip of a $Pb_{0.77(2)}Sn_{0.23(2)}Te$ nanowire which has been isolated on a TEM grid with carbon lace. (b) HR-TEM of a $Pb_{0.77(2)}Sn_{0.23(2)}Te$ nanowire. A regular lattice can be seen showing the high crystalline nature of the the structure where the lattice parameter equates to $6.497(3)$ Å. (c) Core-shell growth of nanowire. (d) SAED of nanowire. (e) Guinier-Preston like zones can be seen forming in-plane within the 3D lattice. No defects can be seen in these regions and compositional analysis reveals the they are the same composition as surrounding areas. (f) A typical long nanowire (> 4 μm).

the source material. Futhermore, no gold was present in the microcrystals suggesting a vapour-solid growth mechanism for these. Figure 4.5a shows the typical cubic $Pb_{0.60(2)}Sn_{0.40(2)}Te$ microcrystals obtained in the growth. EBSD data obtained for the faces of the cubes showed they had a predominantly vicinal $\langle 001 \rangle$ orientation.

The distribution density (DD) of the microcrystals across the substrate surface was much greater than that for nanowires. We found that the DD increased towards the hotter end of the substrate, where we also saw fewer nanowires growing. Figure 4.5b also shows the typical structures observed as you move closer to the hotter end ($\approx$ 300 $^{\circ}\mathrm{C}$) of the substrate. The nucleation of the microcrystals increases greatly and they are in some cases approximately three times larger in size. As a result they merge forming a layer that is $\approx$ 10 μm thick, under which no substrate is visible. Conversely, for growths in the furnace at temperatures lower than the optimum (below $\approx$ 520 $^{\circ}\mathrm{C}$), very little nucleation is observed. Here only a few microcrystals are seen and the DD decreases by approximately one order of magnitude.

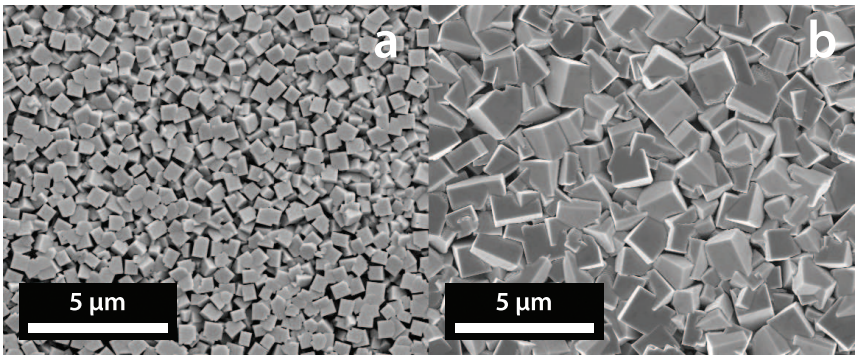

Figure 4.5: (a) SEM image of $Pb_{0.60}Sn_{0.40}Te$ microcrystals. (b) Larger microcrystals merge to form a thick layer of growth towards the hotter end of the substrate

$Pb_{1-x}Sn_xSe$

Similar growth conditions used for the formation of $Pb_{0.77(2)}Sn_{0.23(2)}Te$ nanowires were initially used for the compound $Pb_{1-x}Sn_xSe$. Under these conditions, the furnace temperature in the hot zone is $\approx$ 540 $^{\circ}\mathrm{C}$. At this temperature, and for all Sn compositions, we did not observe the growth of any nanowires or microcrystals. Instead, a thin layer of PbSe material was found to be deposited with trace amounts of Sn detected.

When the temperature of the source material was increased to 550 $^{\circ}\mathrm{C}$, we did not observe any nanowire or microcrystal growth for Sn compositions $x = 0.18$ & $x = 0.23$. However, starting with a Sn composition of $x = 0.30$, we found that the $Pb_{0.70}Sn_{0.30}Se$ powder decomposed into PbSe microcrystals in the form of cubes and SnSe in the form of zig-zag nanowires (Figure 4.6). For temperatures higher than 550 $^{\circ}\mathrm{C}$, no nanowires were observed and the nucleation density of microcubes had increased to the point where the cubes merged to form a thick continuous layer, similar to the morphology seen in $Pb_{0.60(2)}Sn_{0.40(2)}Te$ microcrystals (Fig. 4.5b). Tables 4.3 and 4.5 show a summary of the growth parameters used to obtain SnSe zig-zag nanowires and PbSe microcubes along with the compostion of those materials.

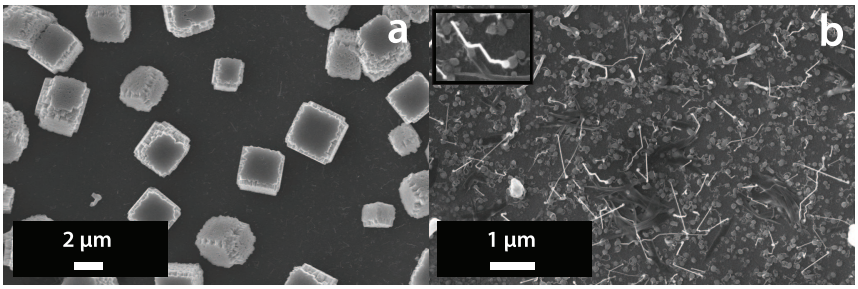

Figure 4.6: (a) Representative SEM image of the growth of PbSe microcubes. (b) SnSe zig-zag nanowires with the inset for clarity. The thickness of the nanowires obtained for $Pb_{0.70}Sn_{0.30}Se$ are $\approx$ 40 nm.

The microcubes were $\approx 2\ \mu m^{\ 3}$ and the zig-zag nanowires were found to be $\approx$ 1 nm in length and $\approx$ 20 nm thick. From EBSD, the struc-

Table 4.5: Representative atomic compositions of the PbSe microcubes and SnSe zig-zag nanowires obtained using EDX analysis.

Nominal starting composition $Pb_{0.70}Sn_{0.30}Se$	Atomic Percent (%) Pb	Se	Sn	Total
SnSe zig-zag nanowires	-	50(2)	50(2)	100
PbSe microcubes	50(2)	50(2)	-	100

ture of the PbSe microcubes was found to be analagous to those of the $Pb_{0.60}Sn_{0.40}Te$ microcrystals. Figure 4.7 shows EBSD data where some features have been highlighted for ease of reference. It shows a typical microcube with growth faces in the $\langle 001 \rangle$ orientation. We did not observe any epitaxial relationship between the substrate and any of the various growth morphologies obtained for solid solutions of $Pb_{1-x}Sn_xTe$ and $Pb_{1-x}Sn_xSe$.

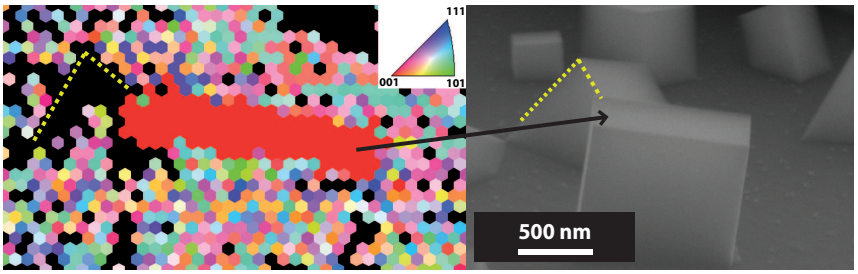

Figure 4.7: Left: EBSD showing the top face of a typical PbSe microcube. The red region indicates a $\langle 001 \rangle$ face. The dashed yellow line is for reference and black arrow indicates the face of the microcube examined using EBSD.

Different approaches to the dispersion of Au nanoparticles were also tested and allowing a suspension of Au nanoparticles in a buffer solution to evaporate naturally was found to be most effective in giving an even and dense coverage of nanoparticles on the silicon substrate. Other meth-

ods included dipping the silicon substrates in the buffer solution, spraying the buffer solution and sputtering a Au layer as well a mixture of the above. Spraying the solution also gave a good dispersion of Au nanoparticles however the density of the Au nanoparticles were very low. These techniques did yield an interesting range of nanomaterials for both Se and Te based compounds, however, none were consistently reproducible and gave a range of growth formations as shown in Figure 4.8.

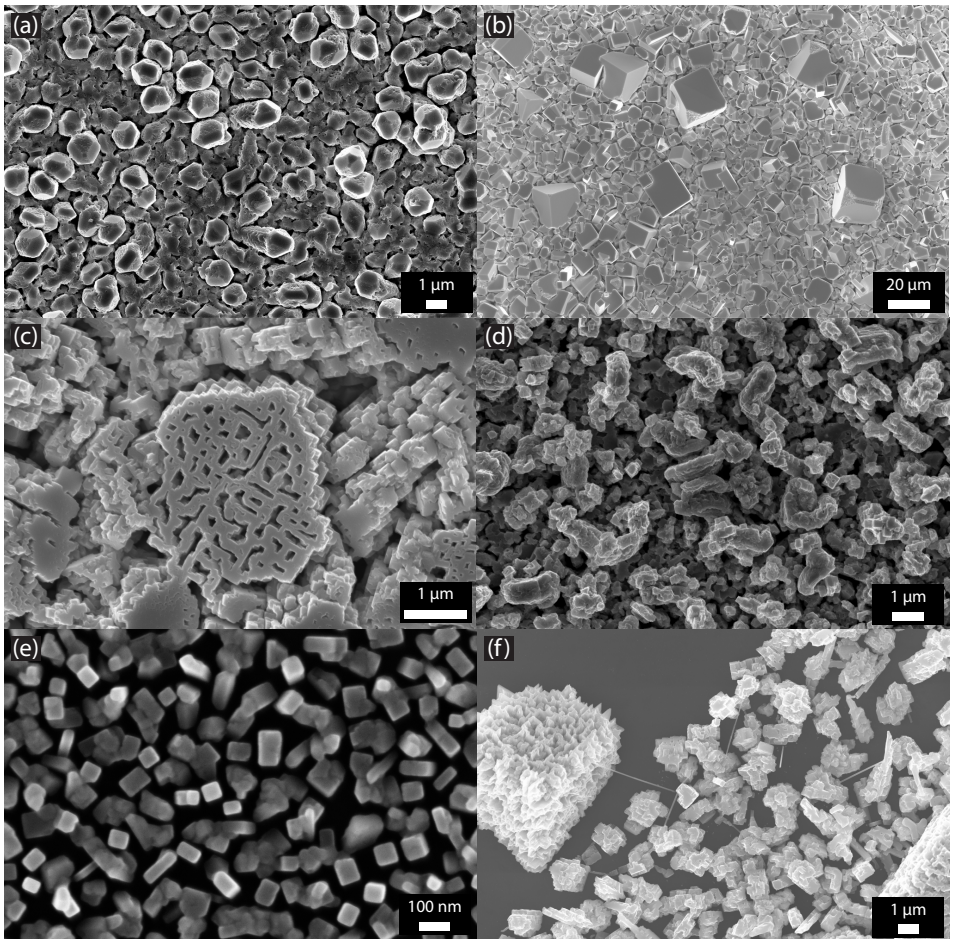

Figure 4.8: A range of morphologies were observed when using different Au nanoparticle dispersion methods. These can be seen above. A layer of Au depostited from sputtering gave a high density, crystalline growth as seen in (a) & (b). A higher density of Au nanoparticles would yield results shown in (c) & (d). A lower Au nanoparticle density achieved from spraying the substrates gave results such as those shown in (e) & (f).

4.4 Summary

In summary we have outlined the optimal methods for the growth of high quality crystal boules of the TCIs $Pb_{0.60}Sn_{0.40}Te$ and $Pb_{1-x}Sn_xSe$ ($x = 0.18, 0.23$ & 0.30). From these we have demonstrated evidence for the growth of high quality $Pb_{0.77(2)}Sn_{0.23(2)}Te$ nanowires using the VLS growth technique. The composition of the nanowires obtained for $Pb_{1-x}Sn_xTe$ is similar to that where a TCI transition is known to occur in bulk crystals. The growth orientation of the $Pb_{0.77(2)}Sn_{0.23(2)}Te$ nanowires was found to be in the [100] direction. It was found that using gold nanoparticles to activate the growth of nanowires is essential. We also find that there is a shift away from a VLS process to a VS process for very long nanowires (> 4 μm) and that the nanowires grow with a core-shell model. For the solid solution $Pb_{0.70}Sn_{0.30}Se$, we found the compound decomposed to form PbSe microcubes and SnSe zig-zag nanowires. For $Pb_{0.82}Sn_{0.18}Se$ and $Pb_{0.77}Sn_{0.23}Se$, only a thin layer of PbSe material was deposited with trace amounts of Sn.

The formation of both nanowires and microcrystals in all experiments is dependent on the local growth conditions where the reactive gasses meet the substrate surface. As mentioned previously, a temperature gradient exists across the substrate and this is a leading factor controlling the morphologies observed. Different mechanisms of growth do occur. The seed growth begins with the formation of a gold alloy (formed from the gold nanoparticles used as a catalyst and the reactive gasses) and this promotes the growth of nanowires.

We found that two possible scenarios occurred for the growth of nanomaterials: either VLS to VS growth or a dominant VS process. We believe both mechanisms play an active role in the materials grown and that they both occur depending on the local temperature and composition of the gases on the substrate surface.

It is plausible that the gas flow is a mixture of elemental and congruent

gas flow, however, this is difficult to prove. To obtain information on the gas flow requires major experimental modifications and investigations of the gas phase mechanism of the growth are studies that we aim to conduct in the future.

Recent work by Safdar *et al.* and Xu *et al.* also demonstrated the growth of long nanowires of $Pb_{1-x}Sn_xTe$ with distinct cubic facets similar to the results we have observed. [86, 87] We do have however some major differences for the growth conditions that were used. Both Safdar *et al.* and Xu *et al.* use powdered SnTe and PbTe as precursors rather than a powder of a fixed stoichiometry, $Pb_{1-x}Sn_xSe$, as in our case. As a result, due to the higher melting points of both these materials, the centre zone (source) of the furnace was much higher to allow for the vaporisation of the source materials. All the growth methods described by Safdar *et al.*, Xu *et al.* and us used Au nanoparticles to initiate growth. Finally, Xu *et al.* used W foils as substrates and Safdar *et al.* used Si substrates as in our growth method. In terms of the stoichiometry of the nanowires produced by Safdar *et al.* and Xu *et al.*, the EDX data showed a varying range of values for x. For $Pb_{1-x}Sn_xSe$, a growth procedure has been proposed by Wang *et al.* where a mixture of Pb and SnSe powders are used as source material. [88] This introduces extra complexity when trying to grow nanowires with a specific stoichiometry. The two major factors affecting the stoichiometry of the nanowires is the amount of material passing over the substrate and the composition of the gas flow. Again the growth methods described by Wang *et al.* differ slightly to the methodology used in the current work. In summary, due to the infancy of the research in this field, a variety of growth methods have been put forward which yield single crystalline nanomaterials useful for further studies of a topological nature.

Our findings demonstrate reliable methods to make TCIs with high SAVR, which could be used to investigate enhanced TCI features. These nanomaterials are therefore good candidates to study TCI materials with

enhanced surface effects and may be used for detailed investigations.

Chapter 5

Sb_2Te_3

5.1 Introduction

In this chapter, detailed characterisation of the TI Sb_2Te_3 is discussed followed by the results for the various methods explored to increase the SAVR of the material. Bulk crystal boules were produced using a modified Bridgman method and the quality of the crystals were determined by x-ray Laue diffraction and EDX. The superconducting properties of the samples were investigated using magnetic susceptibility and resistivity measurements. Finally, the characterisation techniques employed for nanomaterials in 2D and 1D form included SEM, TEM, SAED, EDX, Raman and XPS.

5.2 Sample Preparation & Growth

This section describes the preparation and the growth procedures for both bulk crystals and nanomaterials of Sb_2Te_3. The growth methods used are similar to those described for other bulk materials previously such as SnTe. Supplementary information regarding the growth methods can be found in Chapter 2, Section 2.1.1 and Chapter 3, Section 3.1.

5.2.1 Preparation of bulk crystals of Sb_2Te_3

Bulk crystals of Sb_2Te_3 were produced using a modified Bridgman method as described in Chapter 2 and the procedure used to produce crystals of Sb_2Te_3 were similar to those reported by Zhao *et al*. [8] A quartz tube was made and a stoichiometric mixture of high purity Sb and Te powders (Alpha Aesar 99.999 %) were placed inside.

The volume of the quartz tube used was important as it dictated the value of the Te overpressure during the growth process. The ideal gas equation (Equation 5.1) was used to set the Te pressure, where T_{max} is 1000°C, *n* is the number of moles of material, $R = 8.31 JK^{-1}mol^{-1}$ and *V* is the enclosed volume of the quartz tube.

$$P = \frac{nRT_{max}}{V} \tag{5.1}$$

Samples were synthesized with a vapour pressure between 1.4 MPa and 3 MPa of Te. A 3 MPa over pressure was achieved using a quartz tube with an inner diameter of 16 mm and a length of $\approx$ 13 cm, giving an internal volume of $\approx$ 24 cm^3

The quartz tube was evacuated, sealed and then placed vertically in the centre of a box furnace. The sample was heated from room temperature to 1000 °C at a rate of 200 °C/hr. The samples remained at this temperature for a period of 12 hours before cooling at 5 °C/hr to RT. Upon removing the boule from the quartz tubes, the crystals appeared shiny and metallic. Crystal domains could be visible by eye and were easily detectable under an optical microscope. The crystal domains were approximately $3mm^3$.

5.2.2 Preparation of substrates for nanomaterial growth

The result of using different substrates for the growth of nanomaterials are that a variety of morphologies are observed. We grew Sb_2Te_3 on

two different substrates (silicon and graphene). This section details the preparation methods of these substrates.

Sb_2Te_3 nanomaterials

From the literature discussed previously, the aim was to replicate the growth of Sb_2Te_3 in nanowire form, however we intended to use a direct growth method that uses a VLS growth technique which had not reported in literature. The preparation of silicon substrates prior to growth exactly mirrors those used for the growth of SnTe nanomaterials, which can be found in Chapter 3, Section 3.1.4. Furthermore, the growth method described previously was utilised here, the only difference being the temperature of the centre of the furnace i.e. the source temperature. The temperature at which the source material is deposited onto the substrates that are positioned downstream are also therefore affected.

Similar conditions to those detailed by Lee *et al.* were followed in producing nanowires of Sb_2Te_3. The setup of the growth furnace is described in Chapter 2, Section 2.1.2. The source material used for growth varied. For a majority of the growths, we had primarily used 0.05 g of finely ground Sb_2Te_3 powder which was placed in the centre of the growth furnace. On some occasions we also used separate ceramic crucibles that contained Sb and Te powder. The latter method was used when attempting to replicate the growth procedure of Lee *et al.*. [9]

Particularly for the growth of Sb_2Te_3 nanomaterials, the source material was at a temperature of $\approx$ 480 $^{\circ}\mathrm{C}$. A $\approx$ 35 sccm argon flow was established using a rough vacuum. The approximate temperature of the cold zone where the substrate was placed was $\approx$ 350 $^{\circ}\mathrm{C}$. A flow rate of 35 sccm of argon gas was established to act as a carrier gas.

2D layer growth of Sb_2Te_3

The preparation techniques for the substrates used to obtain 2D layers of Sb_2Te_3 are quite different to those of nanomaterials on silicon substrates. This is because graphene coated copper foils were used as substrate. The graphene deposited onto the copper foils were prepared using a well established CVD method, full details of which can be found in Ref. [89]. To deposit graphene on the copper substrates, which measure 2 cm $\times$ 3 cm, the samples are first placed in the centre of a tube furnace. The copper foils are rapidly heated to temperatures of 1000 $^{\circ}\mathrm{C}$. A mixture of ethylene and hydrogen is allowed to pass over the sample furnace. Ethylene will crack upon contact with the foil and will form graphene domains. The amount of coverage of graphene is dependent on the growth time. In this study, full coverage graphene was used, which is achieved with a growth time of $\approx$ 20 minutes.

The graphene substrates are then transferred to another horizontal tube furnace in order to grow 2D layers of Sb_2Te_3. 0.005 g of powdered Sb_2Te_3 was placed in a ceramic boat the centre of the tube furnace. The temperature of the centre of the furnace is set to 480 $^{\circ}\mathrm{C}$. The graphene substrates are placed downstream at a temperature of $\approx$ 320 $^{\circ}\mathrm{C}$. The total growth time including the ramping stage of the furnace was $\approx$ 18 minutes. Argon was used as a carrier gas with a flow rate of $\approx$ 80 sccm.

It has been reported that defects can be introduced when exposing graphene to higher temperatures in air. Raman studies of graphene(Nan *et al*). have shown the extent of these defects when increasing the temperature of graphene in air. [90] The data showed that defects began to appear in the graphene at temperatures above 600 $^{\circ}\mathrm{C}$. We would expect no defects to occur for the second phase of the growth procedure due to the lower temperature at which the Sb_2Te_3 gorwth occurs and that the growth is performed with a steady flow of argon..

5.3 Bulk Crystal Characterisation

The following section describes various bulk characterisation measurements performed on the boules that were synthesized using the modified Bridgman method to ascertain their quality.

5.3.1 Crystal quality

Laue diffraction was used to ascertain the quality of the crystals produced. The diffraction pattern, as seen in Figure 5.1, is typical of those from various points along the face and length of the crystal boule. The boule was also cleaved in several locations and the diffraction pattern shown in Figure 5.1 showing the c-axis was representative of what was observed on cleaved surfaces from within the boule. The sharp spots are indicative of a highly crystalline sample, however, a rotation of the pattern was observed in some regions of the boule suggesting domains of approximately 5 mm^3 exist within the boule.

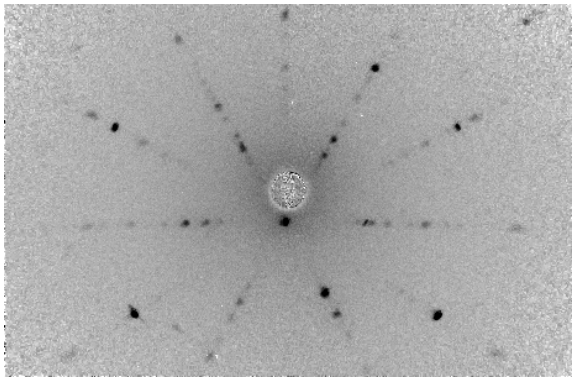

Figure 5.1: X-ray Laue diffraction pattern of Sb_2Te_3 for the c-axis. The sharp diffraction pattern shows the sample is highly crystalline.

EDX spectroscopy was performed on various locations on the boule surface and on several cleaved pieces from within the boule. The stoichiometry of all samples were found to be similar to the original mixing

ratios within experimental error. Table 5.1 shows some typical values for the concentration of Sb and Te.

Table 5.1: Representative atomic compositions (%) of bulk Sb_2Te_3 crystal boules at the surface and within the boule.

Location	Sb	Te	Total
Boule Surface	40(2)	59(2)	100
Centre of Boule	39(2)	60(2)	100

5.3.2 Tests for superconducting behaviour

In total, three different samples of Sb_2Te_3 were produced using the growth procedure described above. The different samples had a Te overpressure of $\approx$ 1.4 MPa, $\approx$ 1.6 MPa and $\approx$ 1.35 MPa respectively. Table 5.2 provides a summary of the samples grown and the carrier density of those samples determined using Hall effect measurements.

Table 5.2: Three boules of Sb_2Te_3 were synthesized with varying Te vapour overpressures. The carrier densities were determined using Hall effect measurements.

Boule No.	Pressure (MPa)	Carrier density (m^{-3})
1	1.40	0.98 x 10^{23}
2	1.60	1.25 x 10^{23}
2	1.35	8.37 x 10^{23}

Small pieces of each of the crystal boules were isolated to examine if the samples exhibit superconductivity. Using a Quantum Design Magnetic Property Measurement System (MPMS) SQUID, dc magnetic susceptibility, χ_{dc}, as a function of temperature was used to determine the onset of superconductivity. For all portions of crystals cleaved from the boules,

no signals of superconductivity were observed or signals stronger than the noise of the system. Magnetic susceptibility measurements would suggest that the correct Te vapour pressures required to make the samples superconducting were not achieved during growth when following similar growth procedures by Zhao *et al.*. [8]

Hall effect measurements were also conducted on cleaved pieces of the crystals. The carrier density of isolated flakes with uniform thickness were measured using a four point probe Hall measurement device. We found that the carrier density for our samples, were in the region of 10^{23} cm^3. The carrier densities reported by Zhao *et al.* for non-superconducting Sb_2Te_3 were $\approx \geq 10^{19}$ cm^3. These values although in agreement, suggest that the necessary Te over pressure was not achieved during the growth procedure to obtain superconducting samples. We would expect the hole carrier density to lie in the region of 10^{18} cm^3 for a superconducting sample. The relationship between the hole carrier density and the Te overpressure can be seen in Figure 5.2. [8]

5.3.3 Resistivity

It is worth highlighting here that the superconductivity in Sb_2Te_3, is thought to be a surface effect. [8] Resistivity measurements were conducted on cleaved sections of the crystal boule to test for superconductivity. Resistivity measurements were also conducted to investigate the relationship between superconductivity and the effect of thinning the samples down progressively. Thinner samples were obtained by further cleaving the sample, and/or exfoliating the surface with Scotch tape.

Both AC and DC resistivity measurements were performed on rectangular cleaved bars taken from all three crystal boules produced. We observed the onset of a superconducting transition in only one sample originating from boule 2. The onset of superconductivity was observed at $\approx$ 7.2 K in DC resistivity as shown in Figure 5.3. This was lower than

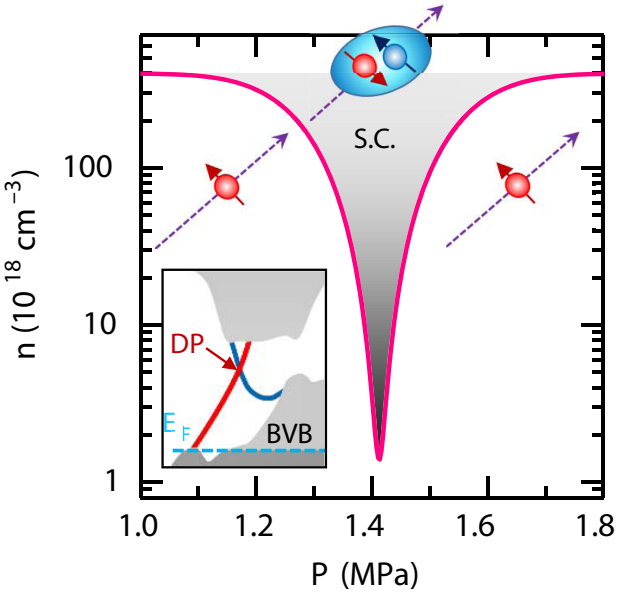

Figure 5.2: Hole carrier density, n, vs Te vapour pressure. The shaded region shows the narrow region in which Sb_2Te_3 become superconducting which is dipicted by the cooper pairs. The inset shows that the Fermi level (E_F) resides in the bulk valence band (BVB) for higher carrier densities. In the superconducting state the Fermi level is raised towards the Dirac point (DP). *Figure adapted from Ref. [8].*

the $\approx$ 9 K T_c transition reported by Zhao *et al*. From the DC resistivity data, one can see that three phases are visible for the the transition into the superconducting state. We were unable to replicate the DC resistivity results for other cleaved bars isolated from boule 2. AC resistivity performed on the sample showing superconductivity in DC measurements did not show a superconducting signal. This was most likely due to local heating effects and the power law. When performing AC resistivity measurements, assuming the contact resistance was approximately equal for each of the four terminals, the current applied is $= 10$ mA whereas for DC resistivity, the current applied is $= 0.4$ mA).

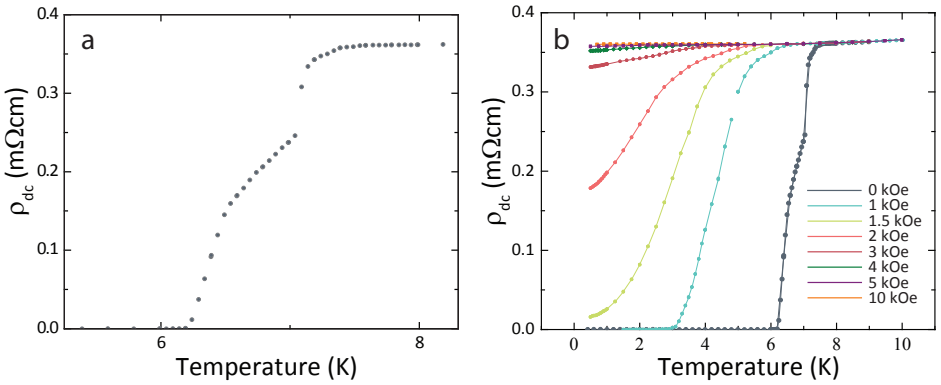

Figure 5.3: (a) DC resistivity of an isolated flake of Sb_2Te_3 from boule 2. A superconducting transition is observed at $\approx$ 7.5 K. A multiphase transition is also observed, most likely due to the inhomogeneity of the sample and distribution of hole carriers. (b) Resistivity vs temperature for magnetic fields applied up to 10 kOe.

The thickness of the sample in which the superconducting signal was detected was 0.198 mm. In total, approximately 20 resistivity measurements were performed with samples of a comparable thickness. A number of samples with a starting sample thickness of $\approx$ 0.25 mm were thinned by cleaving and exfoliation to $\approx$ 0.15 mm. Unfortunately, no superconducting transition in resistivity was observed. Possible reasons include an inhomogeneous carrier distribution or segregation of Te within the boule.

To test the possibility of inhomogeneity within boule 2, repeat resistivity measurement were performed on newly isolated pieces. Superconducting signals were not observed for these samples and this again suggests that there was inhomogeneity within the crystal boules and therefore an issue with the synthesis of the crystals.

5.4 Nanomaterial Characterisation

The growth of Sb_2Te_3 nanowires has been well documented in various publications using a variety of techniques. [91] The main driving force for the formation of Sb_2Te_3 as nanowires in the past has been their use in PRAM devices. These nanowires operated more efficiently compared to thin films due to the lower melting point of nanowires than when the material is in bulk form. Now the focus has shifted to produce nanomaterials to better investigate their topological insulating properties.

With regards to the topological insulating properties of Sb_2Te_3, it has been determined that producing materials with a greater surface-area-to-volume ratio allows for the easier detection of these surface properties, as the signal arising from the bulk with respect to the surface is lowered.

5.4.1 Sb_2Te_3 Nanomaterials

The most challenging aspect of establishing a growth procedure is ensuring that the majority of the variables remain constant from one growth run to the next. By far the two greatest variables are furnace temperature and mass of source material, as discussed in Chapter 2.

Our early results indicated the production of microcrystals of Sb_2Te_3, with the formation of small nanowires dispersed in local regions in and amongst the microcrystals. In these regions, the partial pressure of the growth material is lower providing suitable conditions for the growth of nanowires. Figure 5.4 shows SEM images of various Sb_2Te_3 morphologies

formed at the hotter end of the substrate. (Fig. 5.4a) and the colder end (Fig. 5.4b) respectively. It can be seen that at there is an abrupt change in this instance in the morphologies observed (Fig. 5.4c). Also visible in Fig. 5.4c are large micron sized rods. Distinct facets are visible in the high resolution SEM image of a nanowire (Fig. 5.4d) along with beams upto 15 μm in length (Fig. 5.4e).

Despite following the growth methods described by Lee *et al.* for the growth of Sb_2Te_3 nanowires, there were great difficulties in replicating those results. Figure 5.4 shows the difference between the nanowires obtained by Lee *et al.* and those grown by us. Lee *et al.*'s procedure uses Sb and Te powders placed at different locations in the central hot zone of the growth furnace. This was due to the different melting temperatures of Sb and Te (630 and 449 $^{\circ}\mathrm{C}$, respectively). We did observe the growth of various Sb -Te platelets using this method, however the composition of the platelets varied and many were found to be off stoichiometry and did not yield Sb:Te 2:3.

The disparity between the morphologies obtained by Lee *et al.* and our data shows that the growth conditions are not completely understood. Over 25 trials were conducted to obtain a repeatable growth procedure for the desired morphologies by varying 5 different parameters. As a result, the need for a reliable and repeatable method still exists, which the work in this chapter aimed to address. An optimised growth procedure for nanomaterials of Sb_2Te_3 can pave the way to investigate exotic surface states that these materials posses. However, there is also an interest in detecting the surface superconductivity in this particular system. Currently, the methods required to investigate these properties in nanomaterials, or indeed to ascertain if surface superconductivity exists in nanomaterials presents a challenge. This would also be beyond the scope of this work, however, producing a reliable and repeatable growth procedure with well characterised samples is ongoing.

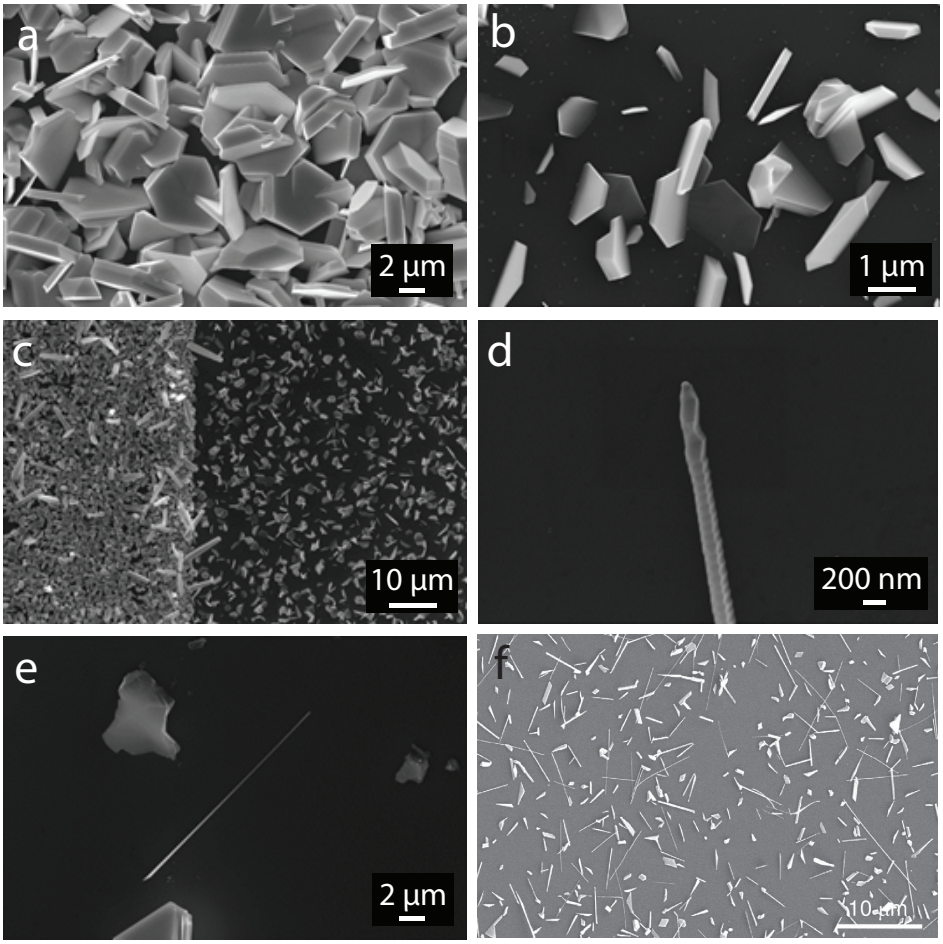

Figure 5.4: SEM image showing the various morphologies observed from both the hot and cold zone regions of the substrate. (a) Growth of Sb_2Te_3 platelets closer to the centre hot zone of the furnace (280 $^{\circ}$C). (b) Growth of Sb_2Te_3 platelets towards the colder end zone of the furnace tube (220 $^{\circ}$C). (c) Abrupt change in the density of Sb_2Te_3 platelets from the hotter to colder sides of the substrate. (d) Sb_2Te_3 nanowire with distinct facets visible along the length of the wire. A Au nanoparticle is also visible on the tip of the wire which promotes tip-growth. (e) Sb_2Te_3 nanowires can reach lengths up to 15 μm. (f) Typical Sb_2Te_3 nanowires as reported by Lee *et al*. *Figure adapted from [9]*.

Table 5.3: Summary of nanomaterial growth results and typical chemical composition of the materials obtained using EDX analysis on silicon substrates.

Starting material (Powder)	Mass (g)	Ar flow rate (sccm)	Source temperature °C	Substrate temperature °C	Morphology	Composition
Sb_2Te_3	0.05	≈ 80	480	≈ 280	Platelets/ stacks/columns	$Sb_{2.04(2)}Te_{2.96(2)}$
Sb_2Te_3	0.05	≈ 80	480	≈ 220	Zig-zag nanowires	$Sb_{1.98(2)}Te_{3.02(2)}$
Sb & Te	0.05	≈ 80	430	≈ 250	Platelets	Varied

5.4.2 2D layers of Sb_2Te_3

In this section we discuss the progress to date of growing Sb_2Te_3 on copper substrates which have a layer or bi-layer of graphene. Prior to growth, the samples were metallic copper coloured. After the growth had occurred, the samples were tarnished and appeared slightly grey colour. This was expected due to the growth of Sb_2Te_3 on the surface of the samples. What was unknown was the morphology the Sb_2Te_3 had undertaken, or if it had formed in the correct stoichiometry.

We aimed to grow samples, where after growth, the substrate surface showed very little signs of change when visually inspected. This was because a low coverage of Sb_2Te_3 was desired. A copper coloured sample post growth was a quick visual inspection that indicated that little growth had occurred and that it may be in layer form.

Figure 5.5 shows AFM images of the surface of the samples post growth. The images show islands of Sb_2Te_3 on the surface of the graphene along with layers of Sb_2Te_3 being formed due to the near 1 nm sized step edges which correspond to the approximate width of a quintuple layer in Sb_2Te_3. To verify this, Raman spectroscopy was used to see if the characteristic fluorescence signal for Sb_2Te_3 from the surface of the sample could be observed. A comparison of the Raman spectra of bulk crystal samples was also to be made.

Grazing angle XPS was also performed to observe peaks corresponding to the presence of Sb_2Te_3. The XPS data was inconclusive as no Sb or Te peaks were detected. Raman spectroscopy data was obtained on cleaved pieces of the crystal boules were performed. This was to obtain reference data to which the 2D layer growth samples could be compared with. Unfortunately, the data obtained from Raman studies of the surface of the Sb_2Te_3/graphene samples and those from bulk crystals were also inconclusive.

With only AFM indicating the possible presence of Sb_2Te_3 on graphene

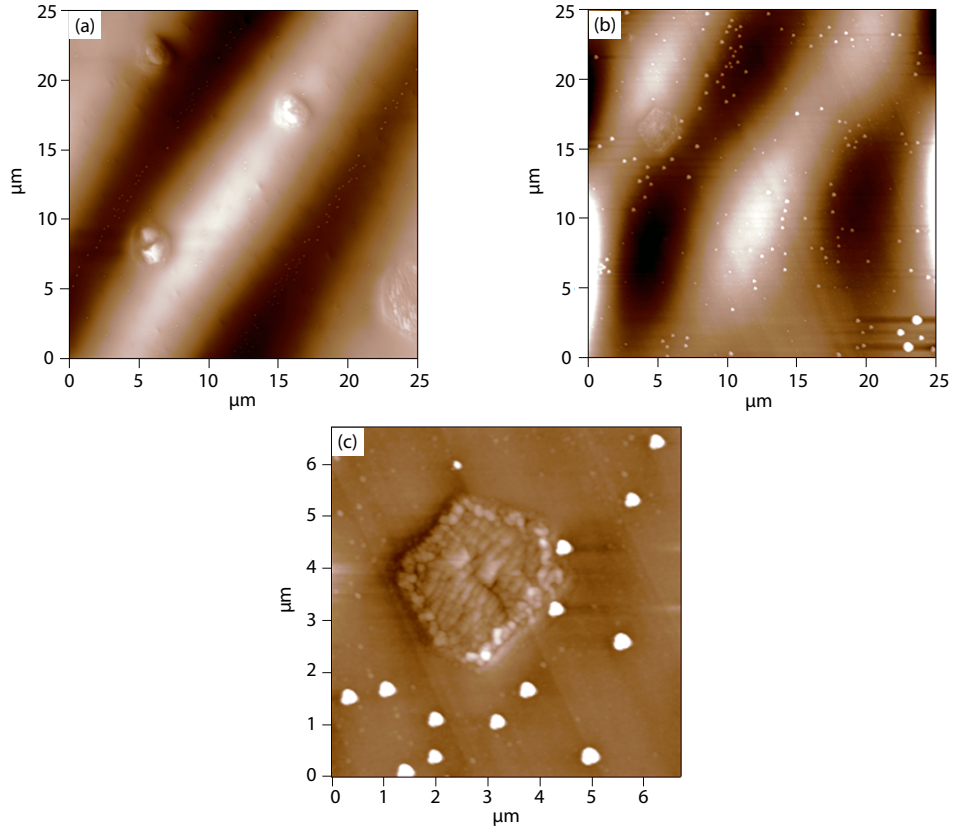

Figure 5.5: AFM image of the surface of graphene coated copper substrates. (a) Low resolution AFM image showing islands of Sb_2Te_3 (b) Low resolution AFM image showing the presence of contamination (circular white dots) (c) High resolution AFM image showing hexagonal features ≈ 5 μm. Indications of the height profiles of the hexagonal features indicate they are multiples of the thickness of the quintuple layers of Sb_2Te_3 (≈ 1 nm).

as layers, there are still uncertainties regarding the stoichiometry of the deposition that is visible in AFM. The characterisation tools that have been used by us are also unable to verify the composition of the deposition and ongoing measurements are taking place to obtain this information. A summary of the growths performed and the outcomes of those can be found in Table 5.4.

Table 5.4: Summary of 2D layer growth results and chemical composition of the materials obtained using EDX analysis on graphene substrates.

Starting material (Powder)	Mass (g)	Ar flow rate (sccm)	Source temperature °C	Substrate temperature °C	Morphology	Composition
Sb_2Te_3	0.03	≈ 80	420	≈ 200	Platelets	$Sb_{2.01(2)}Te_{2.99(2)}$
Sb_2Te_3	0.03	≈ 100	420	≈ 220	Layers/Islands	Unknown
Sb & Te	0.05	≈ 100	420	≈ 250	Crystallites (micron scale)	Various

5.5 Summary

We have shown that of the three Sb_2Te_3 bulk samples that were grown, only boule 2 produced a sample where a superconducting signal could be detected through transport measurements. We have also demonstrated that nanomaterials Sb_2Te_3 can be produced using a VLS/VS growth mechanism. A variety of morphologies were observed from nanowires to platelets. EDX analysis shows the materials had matching stoichiometric values to that of the starting powdered crystals. We also demonstrated the growth of 2D layers of Sb_2Te_3 on graphene through a similar direct growth method, however, further studies are required to characterise these samples to ascertain the composition of the deposition that has formed on the graphene surface. This opens up the possibility of new and novel devices that can be exploited, using the exciting properties of both graphene and Sb_2Te_3. Many further studies are required to refine the growth method to obtain reproducible structures. These studies are on going and raise the prospects of Sb_2Te_3 being used as a candidate for new research for both fundamental physics and novel device fabrication applications.

Chapter 6

Summary and Conclusions

6.1 Summary

In this thesis, four systems have been investigated that have previously been shown to exhibit topological surface states. [3, 21, 22, 51, 52, 56, 57] $Sn_{1-x}In_xTe$, $Pb_{1-x}Sn_xTe$, $Pb_{1-x}Sn_xSe$ and Sb_2Te_3 were amongst the very first materials to exhibit properties of a new state of matter (TIs and TCIs).

SnTe was the first material confirmed to be a TCI through ARPES measurements. [21] Bulk crystals of this material were grown using a modified Bridgman method, a method that had been well established by Tanaka *et al.*. SnTe can also be made superconducting by substituting Sn atoms with In atoms. We were able establish a growth method that could be used to produce high quality crystals of SnTe and $Sn_{1-x}In_xTe$ ($0 \leq x \leq 0.45$). These methods were refined and $Sn_{1-x}In_xTe$ crystals with varying composition were investigated to obtain information of the superconducting transition temperature, T_c, with respect to the In composition. $Sn_{1-x}In_xTe$ is a compound that has been placed into the classification of topological superconductors, which are a new class of materials. Coupled with the knowledge that the exotic surface states of these

materials could be easily detected if they are produced in nanoform, or in a morphology where they possessed a higher SAVR, there is a motivation to produce nanomaterials of TCIs and topological superconductors. A reliable growth method for nanomaterials of SnTe and $Sn_{1-x}In_xTe$ had not been previously established and we presented a growth method that could be used to obtain high quality nanomaterials.

The effect of varying the In composition to the superconducting transition temperature in $Sn_{1-x}In_xTe$ bulk crystals had not been previously investigated. We found that by increasing the In composition, an optimum T_c was observed at $\approx$ 4.5 K. This superconducting transition was achieved for an In substituion of $x = 0.45$.

We were able to use the bulk materials grown to produce nanomaterials using a direct growth method which had not previously been explored. The growth of nanowires of SnTe and $Sn_{1-x}In_xTe$ had not been established prior to the investigations presented in 3, so the motivation behind this work was to achieve reliable growth methods for nanomaterials, in the hope that they could be tested for topological surface states. Powdering the crystal boules so they could be used as starting materials for the growth of nanomaterials, resulted in the stoichiometry of the structures grown matching those of the original crystal boules. We had found that the nanowires grew by a VLS process and that a gold nanoparticle used as a catalyst was essential in producing SnTe nanowires. A reliable growth procedure with optimum conditions was established for the growth of SnTe nanowires. $Sn_{1-x}In_xTe$ nanowires were also obtained. Further work is required to refine the growth methods in order to obtain nanowires with the In content which shows the highest superconducting transition.

A similar experimental approach used for the compound $Sn_{1-x}In_xTe$, was applied to the materials $Pb_{1-x}Sn_xTe$ and $Pb_{1-x}Sn_xSe$. These two compounds have previously been shown to exhibit TCI surface states, yet a growth procedure to obtain high quality nanomaterials had not been established. By varying a number of growth parameters such as the tem-

perature of the source material, substrate temperature and Ar flow rate besides others, a variety of morphologies were observed. After refining the growth methods, we provided first evidence of a direct growth procedure that was obtained and used to produce long smooth nanowires of $Pb_{1-x}Sn_xTe$. The Sn composition of these nanowires was $x = 0.23$. At this level of Sn substitution, bulk materials had been previously investigated to show a TCI transition from trivial to non-trivial. Similar growth methods were also used to produce nanomaterials of $Pb_{1-x}Sn_xSe$, however, it was found that the compound decomposes into PbSe microcubes and SnSe zig-zag nanowires rather than retain the stoichiometry of the source material.

Sb_2Te_3 can be made superconducting at ambient pressures, provided the right conditions during growth are achieved. Sb_2Te_3 is also a TI material and was one of the first 3D topological insulators to be discovered. If samples of Sb_2Te_3 are grown with the correct Te vapour pressure, the carrier concentration reduces to levels sufficient for superconductivity to be observed. The required Te vapour pressure during growth is $\approx$ 1.4 MPa. A number of bulk crystals were produced with a Te vapour pressure between 1.35 MPa and 1.6 MPa to investigate the superconducting properties of this material. We were unable to detect a superconducting signal using magnetic susceptibility measurements for cleaved pieces of the crystal boule. However, transport measurements were also performed and we were able to detect a superconducting transition of $\approx$ 7.5 K from a sample, thickness $= 0.198$ mm, isolated from the boule which was grown with the highest Te vapour pressure of 1.6 MPa (boule 2, Table 5.2). Unfortunately, further samples isolated from boule 2 did not show a superconducting transition. Hall effect measurements were also performed on cleaved sections of the boules. The carrier concentrations obtained for the cleaved samples were $\approx 10^{23}$ m^{-3}, which was consistent for non-superconducting samples. As the superconductivity observed in Sb_2Te_3 is thought to be a surface effect, an investigation into the effect of

sample thickness on superconductivity was also performed. No superconducting signals were detected for samples that were progressively thinned to thicknesses comparable to the sample that showed a superconducting transition. We believe that the lack of superconductivity observed in the samples is due to inhomogeneity of carriers in the crystal boules. An investigation into obtaining a procedure for the growth of nanomaterials of Sb_2Te_3 was conducted. High SAVR materials were obtained in the form of nanowires and platelets on silicon substrates. Graphene was also chosen as a substrate for Sb_2Te_3 growth due to the layered structure of Sb_2Te_3, with the hope of producing new and novel multilayer heterostructures. Much attention has been given to 2D graphene heterostructures in order to investigate new properties and phenomena. Therefore, there is a desire to produce new multilayer heterostructures using a variety of methods. Preliminary results indicate that a growth procedure has been obtained for the layered growth of Sb_2Te_3 on graphene and this work is ongoing.

The next logical step after obtaining nanomaterials of TCIs and TIs is to test if they also possess the same exotic surface states as their bulk counterparts. Currently, this presents a major challenge in this field of research. There are a number of techniques that can be used to ascertain information on the topological surface properties such as transport measurements, yet to directly probe the band structure using a technique such as ARPES is difficult. The materials required for such measurements need to be free from surface oxidation. We began to investigate the effectiveness of using techniques that were common to UHV studies of thin film samples in order to remove surface oxidation on SnTe microcrystals. Various UHV cleaning methods were applied to SnTe microcrystals, something that had not been previously investigated. An XPS study was conducted to ascertain the level of surface oxidation post treatment. We also investigated the effect of various cleaning methods on the surface morphology. We found that the cleaning of microcrystals with atomic hydrogen for a minimum of 15 minutes at 200 °C gave the most effec-

tive results in retaining the surface morphology, whilst removing sufficient surface oxidation required for ARPES measurements.

6.2 Future Work

Refining the method for the growth of Sb_2Te_3 crystal boules and nanomaterials is ongoing. Being able to produce crystal boules with the correct carrier concentration which show a superconducting signal will allow for the materials to be better characterised. Obtaining a reliable growth procedure for Sb_2Te_3 nanomaterials is also ongoing, as is the characterisation of the thin film growth of Sb_2Te_3 on graphene. This will open up further avenues such as making multilayer graphene heterostructures which may reveal new and interesting physics. Growth methods to obtain nanomaterials of $Pb_{1-x}Sn_xSe$ are also being investigated.

The greatest challenge currently is to determine whether the nanomaterials produced in this work exhibit any TCI or TI behaviour. Transport measurements can be made on nanowires or high SAVR materials and these techniques are proven to reveal such exotic behaviour. Currently, investigating the band structure of nanomaterials directly using laser ARPES or nano-ARPES is difficult due to the limitations of the measuring techniques, the size of the nanomaterials, as well surface oxidation. We have begun addressing the issue of surface oxidation through various UHV cleaning methods.

Other avenues have been pursued in increasing the SAVR of TCI and TI materials. Preliminary growth results of BiTeI, a topological insulator, confined within single walled carbon nanotubes have been performed with some success. These materials are commonly investigated using Raman spectroscopy to reveal information about the finite structures they form. Confining materials to carbon nanotubes removes the bulk nature of the material completely and the resulting structures of the confined crystals are only a few atoms wide. The promising results obtained thus far are

exciting as the topologically protected states are a surface specific phenomena i.e. a surface effect that could potentially be investigated without any contribution from the bulk signal.

6.3 Conclusion

Through the search of new states of matter, topological insulators, topological crystalline insulators, various materials that are thought to be topological superconductors or even combinations of the above, have been discovered and more are being predicted. This re-writes what we know about many materials that have already been exploited in exciting applications. This thesis has focused on a very small number of materials that exhibit these properties. By answering some of the questions facing this rapidly moving research field, we move to a point where new, bigger and exciting challenges are presented before us.

We now know the importance of having reliable growth methods which can be used for further studies as well as an eventual aim to use topologically protected states in electronic applications. We showed the benefits of starting with bulk materials in the growth of nanomaterials, and the motivation behind finding repeatable methods of those. The nanostructures produced show interesting properties where now a focus can be in detecting the enhanced surface states they are thought to possess.

Although these surface states are protected from impurities and defects, we are limited by the scientific tools we have to detect them. Many of the surface probes used today such as ARPES and surface conductivity measurements are heavily dependent on using clean surfaces with known crystallographic orientations. Previous methods used to tackle these problems such as in-situ cleaving have not been ideal and to present a surface cleaning solution that can be adjusted for other substrates or samples is promising. Additionally, it is favourable knowing that such a cleaning method ensures that the surface topography is unaffected.

Bibliography

[1] J. Liu, W. Duan, and L. Fu, Phys. Rev. B - Condens. Matter Mater. Phys. **88** (2013).

[2] S.-Y. Xu et al., Nat. Commun. **3**, 1192 (2012).

[3] P. Dziawa et al., Nat Mater **11**, 1023 (2012).

[4] M. Neupane et al., Phys. Rev. B **92**, 075131 (2015).

[5] C. Pauly et al., Phys. Rev. B **86**, 235106 (2012).

[6] G. Wang et al., Nano Res. **3**, 874 (2010).

[7] J. Zhu et al., Sci. Rep. **3**, 2016 (2013).

[8] L. Zhao et al., arXiv , 10 (2014).

[9] J. S. Lee, S. Brittman, D. Yu, and H. Park, J. Am. Chem. Soc. **130**, 6252 (2008).

[10] A. Strauss, Phys. Rev. **157**, 608 (1967).

[11] C. L. Kane and E. J. Mele, Phys. Rev. Lett. **95**, 146802 (2005).

[12] B. A. Bernevig, T. L. Hughes, and S.-C. Zhang, Science **314**, 1757 (2006).

[13] D. N. Sheng, Z. Y. Weng, L. Sheng, and F. D. M. Haldane, Phys. Rev. Lett. **97** (2006).

[14] M. König et al., Science **318**, 766 (2007).

[15] J. E. Moore and L. Balents, Phys. Rev. B - Condens. Matter Mater. Phys. **75** (2007).

[16] Y. Xu et al., Nat. Phys. **10**, 956 (2014).

[17] Y. Ando and L. Fu, arXiv Prepr. arXiv1501.00531 , 1 (2015).

[18] G. J. Snyder, Appl. Phys. Lett. **84**, 2436 (2004).

[19] G. Scott, J. Vac. Sci. Technol. B Microelectron. Nanom. Struct. **9**, 1785 (1991).

[20] T. H. Hsieh et al., Nat. Commun. **3**, 982 (2012).

[21] Y. Tanaka et al., Nat. Phys. **8**, 800 (2012).

[22] L. Fu, Phys. Rev. Lett. **106**, 106802 (2011).

[23] D. Hsieh et al., Nature **452**, 970 (2008).

[24] D. Hsieh et al., Science **323**, 919 (2009).

[25] Y. Xia et al., Nat. Phys. **5**, 398 (2009).

[26] R. A. HEIN and P. H. E. MEIJER, Phys. Rev. **179**, 497 (1969).

[27] A. S. Erickson, J.-H. Chu, M. F. Toney, T. H. Geballe, and I. R. Fisher, Phys. Rev. B **79**, 24520 (2009).

[28] R. D. Zhong et al., Phys. Rev. B **88**, 020505 (2013).

[29] G. Balakrishnan, L. Bawden, S. Cavendish, and M. R. Lees, Phys. Rev. B **87**, 140507 (2013).

[30] T. Sato et al., Phys. Rev. Lett. **110**, 206804 (2013).

[31] J. J. Cha et al., Nano Lett. **10**, 1076 (2010).

[32] D. Kong et al., Nano Lett. **10**, 329 (2010).

[33] D. Kong et al., Nano Lett. **10**, 2245 (2010).

[34] Z. Wang et al., ACS Nano **7**, 2126 (2013).

[35] X. Li, K. Cai, D. Yu, and Y. Wang, Superlattices Microstruct. **50**, 557 (2011).

[36] P. Gehring, B. F. Gao, M. Burghard, and K. Kern, Nano Lett. **12**, 5137 (2012).

[37] P. Yang et al., Adv. Funct. Mater. **12**, 323 (2002).

[38] J. S. Lee, S. Brittman, D. Yu, and H. Park, J. Am. Chem. Soc. **130**, 6252 (2008).

[39] C. M. Lieber, MRS Bull. **28**, 486 (2011).

[40] P. Yang, MRS Bull. **30**, 85 (2005).

[41] P. Gao and Z. L. Wang, J. Phys. Chem. B **106**, 12653 (2002).

[42] D. L. Medlin, Q. M. Ramasse, C. D. Spataru, and N. Y. C. Yang, J. Appl. Phys. **108**, 043517 (2010).

[43] Q. Wei et al., J. Mater. Sci. **46**, 2267 (2010).

[44] V. G. Leontyev, L. D. Ivanova, K. Bente, and V. F. Gremenok, Cryst. Res. Technol. **47**, 561 (2012).

[45] M. Salavati-Niasari, M. Bazarganipour, F. Davar, and A. A. Fazl, Appl. Surf. Sci. **257**, 781 (2010).

[46] M. V. Kovalenko et al., J. Am. Chem. Soc. **129**, 11354 (2007).

[47] Z. Li et al., Nano Lett. **13**, 5443 (2013).

[48] M. Safdar et al., Nano Lett. **13**, 5344 (2013).

[49] J. He, M. G. Kanatzidis, and V. P. Dravid, Mater. Today **16**, 166 (2013).

[50] D. J. Lovell, page 85 (1968).

[51] L. Fu and C. L. Kane, Phys. Rev. B - Condens. Matter Mater. Phys. **76**, 045302 (2007).

[52] S.-Y. Xu et al., Nat. Commun. **3**, 1192 (2012).

[53] Y. Tanaka et al., Phys. Rev. B **87**, 155105 (2013).

[54] S. Safaei, P. Kacman, and R. Buczko, Phys. Rev. B **88**, 045305 (2013).

[55] B. Wojek et al., Phys. Rev. B **87**, 115106 (2013).

[56] D. Hsieh et al., Phys. Rev. Lett. **103** (2009).

[57] H. Zhang et al., Nat. Phys. **5**, 438 (2009).

[58] K. Kuroda, J. Reimann, J. Güdde, and U. Höfer, Phys. Rev. Lett. **116**, 076801 (2016).

[59] L. Zheng et al., RSC Adv. **5**, 40007 (2015).

[60] C. Wang, J. Zhai, Z. Song, F. Shang, and X. Yao, Appl. Surf. Sci. **257**, 949 (2010).

[61] S. Singh et al., Chem. Mater. **27**, 2315 (2015).

[62] Y. Jiang et al., Phys. Rev. Lett. **108**, 066809 (2012).

[63] G. C. Sosso, S. Caravati, and M. Bernasconi, J. Phys. Condens. Matter **21**, 095410 (2009).

[64] M. S. O. Madelung, U. Rössler, *Non-Tetrahedrally Bonded Elements and Binary Compounds I*, volume 41C of *Landolt-Börnstein - Group III Condensed Matter*, Springer-Verlag, Berlin/Heidelberg, 1998.

[65] R. W. G. Wyckoff, Crystal Structures Vol. 2, 1986.

[66] Y. S. Hor et al., Phys. Rev. Lett. **104**, 057001 (2010).

[67] S. Sasaki et al., Phys. Rev. Lett. **107**, 217001 (2011).

[68] K.-H. Jin and S.-H. Jhi, Phys. Rev. B **87**, 075442 (2013).

[69] P. W. Bridgman, Proc. Am. Acad. Arts Sci. **60**, 305 (1925).

[70] M. Kotera, T. Fujiwara, H. Suga, and D. B. Wittry, Jpn. J. Appl. Phys. **29**, 2312 (1990).

[71] G. V. Zhigarev, Neorg. Mater. **24**, 1486 (1988).

[72] Y. S. Hor et al., Phys. Rev. Lett. **104**, 57001 (2010).

[73] M. Kriener, K. Segawa, Z. Ren, S. Sasaki, and Y. Ando, Phys. Rev. Lett. **106**, 127004 (2011).

[74] P. Das, Y. Suzuki, M. Tachiki, and K. Kadowaki, Phys. Rev. B **83**, 220513 (2011).

[75] N. P. Butch, P. Syers, K. Kirshenbaum, A. P. Hope, and J. Paglione, Phys. Rev. B **84**, 220504 (2011).

[76] G. Goll et al., Phys. B **403**, 1065 (2008).

[77] F. F. Tafti et al., Phys. Rev. B **87**, 184504 (2013).

[78] M. Z. Hasan and C. L. Kane, Rev. Mod. Phys. **82**, 3045 (2010).

[79] W. Zhang et al., Chem. Lett. , 446 (2000).

[80] Warwick Photoemission Facility.

[81] V. Neudachina et al., Surf. Sci. **584**, 77 (2005).

[82] M. Saghir, M. R. Lees, S. J. York, and G. Balakrishnan, Cryst. Growth Des. **14**, 2009 (2014).

[83] M. Kirkham, X. Wang, Z. L. Wang, and R. L. Snyder, Nanotechnology **18**, 365304 (2007).

[84] S. Ringer and K. Hono, Mater. Charact. **44**, 101 (2000).

[85] Z. H. Wu, M. Sun, X. Y. Mei, and H. E. Ruda, Appl. Phys. Lett. **85**, 657 (2004).

[86] E. Xu et al., Nano Res. **9**, 820 (2016).

[87] M. Safdar et al., Nano Lett. **15**, 2485 (2015).

[88] Q. Wang et al., Small **11**, 2019 (2015).

[89] N. R. Wilson et al., Nano Res. **6**, 99 (2013).

[90] H. Y. Nan et al., J. Raman Spectrosc. **44**, 1018 (2013).

[91] B. G. Kim et al., Mater. Lett. **65**, 812 (2011).